LAWRENCE
LIVERMORE
NATIONAL
LABORATORY

LLNL-TH-461912

Measurements of Relativistic Effects in Collective Thomson Scattering at Electron Temperatures less than 1 keV

S. Ross

November 10, 2010

Disclaimer

This document was prepared as an account of work sponsored by an agency of the United States government. Neither the United States government nor Lawrence Livermore National Security, LLC, nor any of their employees makes any warranty, expressed or implied, or assumes any legal liability or responsibility for the accuracy, completeness, or usefulness of any information, apparatus, product, or process disclosed, or represents that its use would not infringe privately owned rights. Reference herein to any specific commercial product, process, or service by trade name, trademark, manufacturer, or otherwise does not necessarily constitute or imply its endorsement, recommendation, or favoring by the United States government or Lawrence Livermore National Security, LLC. The views and opinions of authors expressed herein do not necessarily state or reflect those of the United States government or Lawrence Livermore National Security, LLC, and shall not be used for advertising or product endorsement purposes.

This work performed under the auspices of the U.S. Department of Energy by Lawrence Livermore National Laboratory under Contract DE-AC52-07NA27344.

UNIVERSITY OF CALIFORNIA, SAN DIEGO

Measurements of Relativistic Effects in Collective Thomson Scattering at Electron Temperatures less than 1 keV

A dissertation submitted in partial satisfaction of the
requirements for the degree
Doctor of Philosophy

in

Engineering Sciences (Engineering Physics)

by

James Steven Ross

Committee in charge:

George Tynan, Chair
Farhat Beg
Farrokh Najmabadi
Tom O'Neil
Mark Tillack
Dustin Froula

2010

Copyright
James Steven Ross, 2010
All rights reserved.

The dissertation of James Steven Ross is approved, and it is acceptable in quality and form for publication on microfilm and electronically:

Chair

University of California, San Diego

2010

EPIGRAPH

The main purpose of science is simplicity
and as we understand more things,
everything is becoming simpler.
—Edward Teller

TABLE OF CONTENTS

Signature Page iii

Epigraph iv

Table of Contents v

List of Figures vii

Acknowledgements xiv

Vita and Publications xvi

Abstract of the Dissertation xx

Chapter 1 Introduction 1
- 1.1 Thomson Scattering Overview 1
- 1.2 History of Thomson Scattering 2
- 1.3 Thomson Scattering from Inertial Confinement Fusion Plasmas 4
- 1.4 Summary of Experimental Results 5

Chapter 2 Thomson Scattering 10
- 2.1 Scattered Power Spectrum 12
- 2.2 First Order Relativistic Correction 19
- 2.3 Physical Picture of the Fluctuation Spectrum 23

Chapter 3 Experiment 26
- 3.1 Experimental Design 26
- 3.2 Jupiter Laser Facility 30
  - 3.2.1 Laser Configuration 30
  - 3.2.2 Target 32
  - 3.2.3 Thomson Scattering Configuration 32
- 3.3 Laboratory for Laser Energetics 34
  - 3.3.1 Target 35
  - 3.3.2 Laser Configuration 36
  - 3.3.3 Thomson Scattering Configuration 37
  - 3.3.4 Thomson scattering alignment and focusing . . . 40

Chapter 4 Thomson scattering from electron and ion waves in laser produced plasma 43
- 4.1 Electron-plasma waves 43
- 4.2 Ion-acoustic waves 45

4.2.1 Electron Temperature 48
4.2.2 Plasma Flow Velocity 49
4.2.3 Electron Density 50
4.2.4 Ion Temperature 50
4.3 The Complete Spectrum 50
4.3.1 Two Color Thomson Scattering 54

Chapter 5 Thomson Scattering Measurements of Hydrodynamic Evolution 58
5.1 Gas Jet Hydrodynamics 59
5.2 High Temperature Hohlraum 61

Chapter 6 Observation of Relativistic Effects in Collective Thomson Scattering in Laser Produced Plasma 64
6.1 Asymmetric Relativistic Correction 65

Chapter 7 Conclusions 72
7.1 Future Work 72
7.1.1 Thomson scattering on the NIF 72
7.1.2 Electron feature measurements with a 4ω probe . 75
7.2 Final Word 77

Appendix A Delta Lambda EPW 80

Bibliography 83

LIST OF FIGURES

Figure 1.1: The Thomson scattering spectrum as a function of the scattering parameter. The charge state (Z=10) and the electron and ion temperatures are held constant ($T_e/T_i = 1$) while the density is varied to change the scattering parameter. 2

Figure 1.2: A NIF Au hohlraum target is shown. The hohlraum surounds the spherical fuel capsule. 192 laser beams heat the gold walls which then emit x-rays which in turn ablate material from the fuel capsule. A mix of helium and hydrogen fill the hohlraum to slow the collapse of the gold walls. Cryogenic cooling rings are used to cool the target to 18 K. Image courtesy of LLNL. . 6

Figure 1.3: Thomson scattering is collective for most laser produced plasmas. The solid black line shows where $\alpha_{EPW} = 1$ assuming a 2ω probe beam and 90° scattering. The accessible parameter space for 3 different laser systems are shown. The black X's correspond to the data shown in Figure 4.1. 7

Figure 2.1: A typical Thomson scattering scattering geometry where the electron field of the incident laser ($\vec{E}_0$) is perpendicular to the direction of observation ($\vec{k}_0$). 12

Figure 2.2: The high frequency spectrum is calculated using the relativistic treatment (Eq. 2.42, black line) and the non-relativistic treatment (Eq. 2.43, blue line). Both calculations use an electron density of 4×10^{19} cm^{-3}, an electron temperature of 410 eV and a scattering angle of 90°. The scattering parameter for these conditions is $\alpha = 2.5$. The low frequency feature has been suppressed. 19

Figure 2.3: The effect of relativistic aberration is shown on a source that emits uniformly at rest (a, c). The angle between the direction of observation and the direction the source is moving is given by γ. When the source is moving to the right (b) the scattered light intensity in the direction of the observer decreases. When the source is moving to the right (d) the observer sees an increase in intensity. 20

Figure 2.4: The components of the Lorentz force on the electron are shown. $\vec{F}$ denotes the force due to the electric field and $\frac{\vec{v}}{c} \times \vec{B}$ the magnetic field. As the velocity of the particle changes directions the direction of the force due to the magnetic field changes directions as well. For a particle moving away from the observer (a) the two components of the Lorentz force are in opposite directions and the total force is reduced. When the particle is moving toward the observer (b) the components add the total force is increased. 22
Figure 2.5: Particle motion in an electrostatic potential. 24

Figure 3.1: A sample experimental setup where a pair of lenses image light scattered from the plasma into a spectrometer coupled to a streak camera. The spectrometer and streak camera slits are imaged into the plasma where their overlap with the Thomson scattering probe beam defines the Thomson scattering volume. 27
Figure 3.2: A sample of the measured spectra using this experimental setup is shown. Scattering from electron plasma waves (a) and ion-acoustic waves (b) are observed. The residual stray light from the 2ω is filtered from the electron plasma wave measurement (a) and present at 527 nm in the ion-acoustic wave measurement. 29
Figure 3.3: (a) Experimental setup. Thomson scattered light is collected 90° relative to the laser beam. Scattering from (b) electron-plasma waves and (c) ion-acoustic waves are displayed. (d) The spectral response of the system used to measure the electron-plasma wave spectra is characterized using a tungsten lamp. (e) The Thomson scattering k-vector diagram shows the orientation of the k-vector that is probed. (f) The ion-acoustic wave spectrum (dots) at 1 ns is fit by the calculated form factor (solid line) with an electron temperature of 240 eV and a density of 1.4×10^{19} cm^{-3} after subtracting the background and stray light. 31
Figure 3.4: A typical 3 ns flat in time Janus pulse. 32
Figure 3.5: (a) An interferometer is used to characterize the neutral density at the Thomson scattering volume as a function of backing pressure. (b) The gas jet density has been measured to scale linearly with backing pressure. 33

Figure 3.6: The 1/3-meter spectrometer coupled to a streak camera is calibrated for wavelength sensitivity using a tungsten lamp. The measured spectrum for an S-20 streak tube is shown (red curve). The ratio of the known spectrum (black dashed line) to the measured spectrum (red line) results in the correction factor. Two correction factors are shown, one for the S-1 (green line) streak tube and one for the S-20 (blue line) streak tube. 34
Figure 3.7: The Omega target setup is shown. The Thomson scattering volume is located 200 μm outside the LEH of a Au half-hohlraum heated with 19 beams in 3 distinct cones. A k-vector diagram shows the ion-acoustic fluctuations that are probed. 35
Figure 3.8: The Vanadium target setup is shown. The Thomson scattering volume is located 200 μm off the foil surface heated with a single beam. 36
Figure 3.9: The Omega Thomson scattering diagnostic setup is shown. The light scattered form target chamber center enters from the bottom left corner. The light is reflected off mirrors labeled M1 through M7, only mirrors M3 through M7 are shown. M4 and M7 are focusing mirrors that focus the scattered light onto the entrance slit of the spectrometers. S1 is a beam splitter. 38
Figure 3.10: The Omega Thomson scattering diagnostic installed in the Omega target bay is shown. 39
Figure 3.11: The Omega Thomson scattering diagnostic wiring diagram is shown. 40
Figure 3.12: The fiber alignment cart is used to precisely position a fiber in the Omega target chamber for Thomson scattering alignment. . 41
Figure 3.13: A alignment grid target is imaged using the Omega target positioning system (Target Plane) and the Thomson scattering diagnostic in focus mode (Detector Plane). The imaging system produces a 58° counter-clockwise rotation of the image. 42

Figure 4.1: Three streak camera records of the Thomson scattering spectrum from the electron feature are shown for different plasma conditions. The scattering parameter decreases as the density decreases:(a) 1.7×10^{19} cm^{-3}, (b) 2.5×10^{18} cm^{-3}, (c) 1.8×10^{18} cm^{-3}. The spectra at 0.5 ns in each streak record (black lines) are shown. The calculated Thomson scattering spectrum (dashed-white line) using the temperature and density is plotted for each spectra. The attenuated region at $\delta\lambda = 0$ is due to the 2ω notch filter. 44

Figure 4.2: By varying the electron temperature and density the error in the measurement can be assessed. The experimental data is shown in red and the best fit for each spectra is shown in black: $T_e = 140$ eV, $n_e = 5.8 \times 10^{18}$ cm^{-3} for (a) and (c), $T_e = 200$ eV, $n_e = 1.8 \times 10^{18}$ cm^{-3} for (b) and (d). In plot (a) n_e is increased by 15% for the blue curve and decreased by 15% for the green curve, $T_e = 140$ eV is held constant. In plot (b) n_e is increased by 15% for the blue curve and decreased by 15% for the green curve, $T_e = 200$ eV is held constant. In plot (c) $n_e = 5.8 \times 10^{18}$ cm^{-3} is held constant and T_e is increased by 10% for the blue curve and decreased by 10% for the green curve. In plot (d) $n_e = 1.8 \times 10^{18}$ cm^{-3} is held constant and T_e is increased by 25% for the blue curve and decreased by 25% for the green curve. The actual errors in the measurement of T_e and n_e is clearly less than the ranges shown here. 46

Figure 4.3: (a) Thomson scattering was measured from a Nitrogen gas jet with beam Configuration B. A 2ω notch filter is used to suppress the ion feature. (b) A lineout at 0.5 ns is compared to the Thomson scattering form factor for the listed parameters. . . . 47

Figure 4.4: A sample ion-acoustic spectrum is shown for the 3 ns pulse configuration. (b) The ion feature is calculated using Eq. (2.42) for 3 different values of ZT_e and compared to the experimental data at 1 ns. The best fit (green line) is calculated with $T_e = 240$ eV and a density of $n_e = 1.25 \times 10^{19}$ cm^{-3}. The temperature is increased by 40% (red line) and decreased by 40% (blue line) to shown the dependence on the electron temperature. The charge average ionization state is assumed to be $Z = 7$. 48

Figure 4.5: The percent error in the measurement of ZT_e is shown for two different assumptions of the ion temperature. As the ionization state increases the error in the measurement of ZT_e decreases. . 49

Figure 4.6: (a) A streak camera record of the Thomson scattering from the ion feature is shown. The spectra at 2.5 ns is plotted in (b) where the best fit is shown using the electron temperature and density from the simultaneously measured electron feature ($T_e = 240$ eV, $n_e = 1.3 \times 10^{19}$ cm^{-3}). The ion temperature is then varied to fit the ion feature spectra. The best fit is calculated for $T_i = 180$ eV. The spectra is calculated for T_i plus (blue line) and minus (green line) 60 eV for comparison. 51

Figure 4.7: The electron density (a) and temperature (b) are shown as red circles measured using electron feature using Configuration B. The ion temperature (b) is shown as blue squares measured using the ion feature. 52

Figure 4.8: The Thomson scattering form factor is calculated for $T_e = 750$ eV, $n_e = 1{\times}10^{20}$ cm^{-3}, and $\theta = 90°$ for two different probe wavelengths. The spectrum from the 2ω probe is then normalized to the 4ω probe spectrum using the difference in k-vectors. 53
Figure 4.9: The possible values of T_e and n_e for a give pair of $\Delta\lambda$'s are shown. The region where the 2ω values (grey line) overlap the 4ω values (black line) gives the values of T_e and n_e consistent with both $\Delta\lambda$ values. 55
Figure 4.10: Thomson-scattering data from the 2ω probe(a) and the 4ω probe(b). 2ω spectra(c) and the 4ω spectra(d) are shown (black line) with the best fit of the theoretical form factor (blue line). The increased width of the 2ω spectra may be an effect of a slightly larger 2ω spot size increasing the Thomson-scattering volume. . 56

Figure 5.1: The electron temperature and density are measured as a function of time. The red points show data measured from the primary beam and the blue points are measured from the low energy probe beam. The measurements while the primary beam is off are compared to a simple adiabatic expansion model (black line) and the same model including temperature equilibration between the electrons and ions (blue line). The initial conditions for the calculated density are assumed to equal the measured temperature and density at 1.65 ns. 59
Figure 5.2: Electron temperature and density is measured from 800 ps to 1500 ps relative to the heater beams which turn on at 0 ps and off at 1000 ps. The electron density is normalized by the critical density for 3ω light ($n_c = 9.0 \times 10^{21}$ cm^{-3}), the primary wavelength of the Omega lasers. 62

Figure 6.1: Top panels: raw streak data. Bottom panels: experimental data (solid-black line) at 2 ns normalized to the blue-shifted feature and compared to the non-relativistic (blue-dashed line) and relativistic (solid-red line) form factors. As the temperature and density increase, the phase velocity of the electron-plasma wave increases (a) $\beta = 0.03$, (b) $\beta = 0.06$, (c) $\beta = 0.09$ and the difference between the non-relativistic and relativistic form factors becomes more pronounced. 65

Figure 6.2: The measured peak powers in the red-shifted feature are divided by the calculated peak powers [Eq. (6.2), diamonds] and are plotted as a function of phase velocity. The electron temperature ranged from 85 eV to 720 eV. Data in perfect agreement with the non-relativistic form factor would have a value of unity. The ratio of the relativistic peak power (solid line) and the corrected non-relativistic peak power [Eq. (6.3), grey circles] divided by the non-relativistic peak power are shown. . 66

Figure 6.3: The ratio of the blue-shifted feature divided by the red-shifted feature is shown using Eq. (6.1) (black line) and Eq. (6.4) (dotted line) both are plotted as a function of phase velocity. The scattering parameter, α, is held constant at 1.5 (a) and 2.5 (b) for each calculation. Eq. (6.4) shows good agreement with Eq. (6.1) for small values of the scattering parameter and low phase velocity. 68

Figure 6.4: The scattering geometry is shown for a series of scattering angles, (a) $\theta < 40°$, (b) $\theta \approx 40°$ and (c) $\theta > 40°$. Both the red-shifted scattered wave vector, $\vec{k}_s^{red}$, and the blue-shifted scattered wave vector, $\vec{k}_s^{red}$ are shown. 69

Figure 6.5: (a) The relationship between the scattering angle, the angle between $\vec{k}_0$ and $\vec{k}$, and the angle between $\vec{k}_s$ and $\vec{k}$ is shown for both $\vec{k}_s^{red}$ and $\vec{k}_s^{blue}$. The scattering parameter and the density are held constant. (b) The ratio of the blue-shifted correction divided by the red-shifted correction is shown for the relativistic aberration term and the $\vec{v} \times \vec{B}$ term, plotted as a function of scattering angle. The scattering parameter, α, is held constant at 1.7 by changing the electron temperature, the density is fixed at 1×10^{20} cm^{-3}. 70

Figure 6.6: As the scattering angle decreases the magnitude of $\vec{k}$ decreases causing an increase in the normalized phase velocity $\beta = \omega/kc$. 70

Figure 7.1: A Thomson scattering diagnostic is currently under development on the NIF to measure the plasma conditions inside an ignition hohlraum. A 4ω probe beam is currently being designed to deliver 1 kJ of energy in a 3 ns flat-in-time pulse to target chamber center. The Thomson scattered light will then be collected and propagated to a diagnostic platform. An example Thomson scattered spectrum from Omega is shown. . . . 73

Figure 7.2: The non-relativistic [Eq. (2.43), blue-dashed line], first order relativistic [Eq. (2.42), red-dotted line] and fully relativistic (solid-black line) form factors are compared for typical plasma conditions on the NIF: an electron temperature of 10 keV, electron density of 8.0×10^{20} cm^{-3}, and a scattering angle of 35 degrees using a Thomson scattering probe beam with a wavelength of 263.5 nm. These conditions result in a normalized electron-plasma wave phase velocity of 0.37. 74
Figure 7.3: High-frequency Thomson scattering data measured from a Vanadium foil target at Omega using a 4ω probe beam. A $3\omega/2$ block is used to suppress light generated by the 3ω heater beam. . . . 76
Figure 7.4: (a) The electron feature and (b) ion feature are measured from a Vanadium foil target and compared to the Thomson scattering form factor (Eq. 2.42) with an electron temperature of 1.1 keV and an electron density of 2.1×10^{20} cm^{-3}. 77
Figure 7.5: (a) The electron temperature and (b) density are shown for a NIF hohlraum hydrodynamic simulation at peak laser power [60]. A quarter of the hohlraum is shown with the fuel capsule centered at (0, 0), the hohlraum wall extends along the top left region and the LEH is centered at (4.5 mm, 0). 78
Figure 7.6: The wavelength of the blue-shifted Thomson scattering resonance is calculated using the electron temperatures and densities shown in Fig. 7.5 with a scattering angle of $\theta = 147°$. The 195 nm contour is shown. The region with scattered wavelengths between 150 and 195 nm would be completely absorbed by propagation in air. 79

ACKNOWLEDGEMENTS

While this dissertation is a summary of the work completed during my years as a graduate student there are a number of people who's support made this work possible. I would like start by thanking Holly for her constant support and understanding. After weeks of long hours at JLF and travel to Omega in Rochester she was always understanding of the time and commitment required to complete a Ph.D after just completing her own.

I'd like to thank my advisor Prof. George Tynan for giving me the opportunity to succeed and the support to excel. I'd also like to thank Dr. Dustin Froula as my most steadfast proponent and the person who read the most drafts, wether it was a journal article I was writing or this dissertation. I'd like to acknowledge Dr. Siegfried Glenzer for his mentorship and encouragement. I also need to acknowledge the laser crews at both the JLF and Omega for their support.

This work was performed, under the auspices of the Department of Energy, by Lawrence Livermore National Laboratory under Contract No. DE-AC52-07NA27344.

Chapter 4, in part, is a reprint of material as it appears in: Ross, J. S, Glenzer, S. H, Palastro, J. P, Pollock, B. B, Price, D, Tynan, G. R, Froula, D. H. "Thomson scattering measurements in the collective and non-collective regimes in laser produced plasma" (Invited) *Rev Sci Instrum* 81, 10D523 (2010). The dissertation author was the primary investigator and author of this paper.

Chapter 5, in part, is a reprint of material as it appears in: Ross, J. S, Glenzer, S. H, Palastro, J. P, Pollock, B. B, Price, D, Tynan, G. R, Froula, D. H. "Thomson scattering measurements in the collective and non-collective regimes in laser produced plasma" (Invited) *Rev Sci Instrum* 81, 10D523 (2010). The dissertation author was the primary investigator and author of this paper.

Chapter 6, in part, is a reprint of material as it appears in: Ross, J. S, Glenzer, S. H, Palastro, J. P, Pollock, B. B, Price, D, Divol, L, Tynan, G. R, Froula,

D. H. "Observation of Relativistic Effects in Collective Thomson Scattering" *Phys Rev Lett* (2010) vol. 104 (10) pp. 105001. The dissertation author was the primary investigator and author of this paper.

VITA

2003	B. A. in Physics, Pomona College
2003-2005	M. S. in Engineering, Applied Science, University of California, Davis
2007-2010	Ph. D. in Mechanical and Aerospace Engineering, University of California, San Diego

PUBLICATIONS

Ross, J. S, Glenzer, S. H, Palastro, J. P, Pollock, B. B, Price, D, Divol, L, Tynan, G. R, Froula, D. H. "Observation of Relativistic Effects in Collective Thomson Scattering" *Phys Rev Lett* (2010) vol. 104 (10) pp. 105001

Ross, J. S, Glenzer, S. H, Palastro, J. P, Pollock, B. B, Price, D, Tynan, G. R, Froula, D. H. "Thomson scattering measurements in the collective and non-collective regimes in laser produced plasma" (Invited) *Rev Sci Instrum* vol. 81, 10D523 (2010).

Ross, J. S, Froula, D. H, Mackinnon, A. J, Sorce, C, Meezan, N, Glenzer, S. H, Armstrong, W, Bahr, R, Huff, R, Thorp, K. "Implementation of imaging Thomson scattering on the Omega Laser" *Rev Sci Instrum* (2006) vol. 77 (10) pp. 10E520

Froula, D. H, Divol, L, London, R. A, Berger, R. L, Doppner, T. Meezan, N. B, Ralph, J, **Ross, J. S**, Suter, L. J, Glenzer, S. H. "Experimental basis for laser-plasma interactions in ignition hohlraums at the National Ignition Facility" *Phys Plasmas* (2010) vol. 17 (5) pp. 056302

Clayton, C. E, Ralph, J. E, Albert, F, Fonseca, R. A, Glenzer, S. H, Joshi, C, Lu, W, Marsh, K. A, Martins, S. F, Mori, W. B, Pak, A, Tsung, F. S, Pollock, B. B, **Ross, J. S**, Silva, L. O, Froula, D. H. "Self-Guided Laser Wakefield Accerleration beyong 1 GeV Using Inization-Induced Injection" *Phys Rev Lett* (2010) vol. 105, 105003

Palastro, J. P, **Ross, J. S**, Pollock, B, Divol, L, Froula, D. H, Glenzer, S. H. "Fully relativistic form factor for Thomson scattering" *Phys Rev E* (2010) vol. 81 (3) pp. 036411

Froula, D. H, Clayton, C. E, Doppner T, Marsh, K. A, Barty, C. P. J, Divol, L, Fonseca, R. A, Glenzer, S. H, Joshi, C, Lu, W, Martins, S. F, Michel, P, Mori, W. B, Palastro, J. P, Pollock, B. B, Pak, A, Ralph, J. E, **Ross, J. S**, Siders, C. W, Silva, L. O, Wang, T. "Measurements of the Critical Power for Self-Injection of Electrons in a Laser Wakefield Accelerator" *Phys Rev Lett* (2009) vol. 103 (21) pp. 215006

Froula, D. H, Divol, L, London, R. A, Berger, R. L, Doppner, T, Meezan, N. B, **Ross, J. S**, Suter, L. J, Sorce, C, Glenzer, S. H. "Observation of the Density Threshold Behavior for the Onset of Stimulated Raman Scattering in High-Temperature Hohlraum Plasmas." *Phys. Rev. Lett.* (2009) 103, 045006.

Petrasso, R. D, Li, C. K, Seguin, F. H, Rygg, J. R, Frenje, J. A, Betti, R, Knauer, J. P, Meyerhofer, D. D, Amendt, P. A, Froula, D. H, Landen, O. L, Patel, P. K, **Ross, J. S**, Town, R. P. J. "Lorentz Mapping of Magnetic Fields in Hot Dense Plasmas" *Phys Rev Lett* (2009) vol. 103 (8) pp. 085001

Neumayer, P, Berger, R, Divol, L, Froula, D. H, London, R. A, MocGowan, B. J, Meezan, N. B, **Ross, J. S**, Sorce, C, Suter, L. J, Glenzer, S. H. "Suppression of stimulated Brillouin scattering by increased Landau damping in multiple-ion-species hohlraum plasmas" *Phys Rev Lett* (2008) vol. 100 (10) pp. 105001

Kline, J. L, Montgomery, D. S, Rose, H. A, Goldman, S. R, Froula, D. H, **Ross, J. S**, Stevenson, R. M, Lushnikov, P. M. "Mitigation of stimulated Raman scattering in hohlraum plasmas" *Journal of Phys* (2008) vol. 112 (2) pp. 022030

Divol, L, Berger, R. L, Meezan, N. B, Froula, D. H, Dixit, S, Michel, P, London, R, Strozzi, D, **Ross, J. S**, Williams, E. A, Still, B, Suter, L. J, Glenzer, S. H. "Three-dimensional modeling of laser-plasma interaction: Benchmarking our predictive modeling tools versus experiments". *Phys Plasmas* (2008) vol. 15 (5) pp. 056313

Neumayer, P, Berger, R. L, Callahan, D, Divol, L, Froula, D. H, London, R. A, MacGowan, B. J, Meezan, N. B, Michel, P. A, **Ross, J. S**, Sorce, C, Widmann, K, Suter, L. J, Glenzer, S. H "Energetics of multiple-ion species hohlraum plasmas" *Phys Plasmas* (2008) vol. 15 (5) pp. 056307

Niemann, C, Berger, R. L, Divol, L, Froula, D. H, Jones, O, Kirkwood, R. K, Meezan, N, Moody, J. D, **Ross, J. S**, Sorce, C, Suter, L. J, Glenzer, S. H. "Green frequency-doubled laser-beam propagation in high-temperature hohlraum plasmas" *Phys Rev Lett* (2008) vol. 100 (4) pp. 045002

Kugland, N. L, Constantin, C. G, Neumayer, P, Chung, H. -K, Collette, A, Dewald, E. L, Froula, D. H, Glenzer, S. H, Kemp, A, Kritcher, A. L, **Ross, J. S**, Niemann, C. "High K alpha x-ray conversion efficiency from extended source gas jet targets irradiated by ultra short laser pulses" *Appl Phys Lett* (2008) vol. 92 (24) pp. 241504

Froula, D. H, Divol, L, Berger, R. L, London, R. A, Meezan, N. B, Strozzi, D. J, Neumayer, P, **Ross, J. S**, Stagnitto, S, Suter, L. J, Glenzer, S. H. "Direct measurements of an increased threshold for stimulated Brillouin scattering with polarization smoothing in ignition hohlraum plasmas" *Phys Rev Lett* (2008) vol. 101 (11) pp. 115002

Froula, D. H, Divol, L, London, R. A, Michel, P, Berger, R. L, Meezan, N. B, Neumayer, P, **Ross, J. S**, Wallace, R, Glenzer, S. H. "Pushing the limits of plasma length in inertial-fusion laser-plasma interaction experiments" *Phys Rev Lett* (2008) vol. 100 (1) pp. 015002

Froula, D. H, Divol, L, Meezan, N. B, Dixit, S, Moody, J. D, Neumayer, P, Pollock, B. B, **Ross, J. S**, Glenzer, S. H. "Ideal laser-beam propagation through high-temperature ignition hohlraum plasmas" *Phys Rev Lett* (2007) vol. 98 (8) pp. 085001

Meezan, N. B, Berger, R. L, Divol, L, Froula, D. H, Hinkel, D. E, Jones, O. S, London, R. A, Moody, J. D, Marinak, M. M, Niemann, C, Neumayer, P. B, Prisbrey, S. T, **Ross, J. S**, Williams, E. A, Glenzer, S. H, Suter, L. J. "Role of hydrodynamics simulations in laser-plasma interaction predictive capability" *Phys Plasmas* (2007) vol. 14 (5) pp. 056304

Froula, D. H, **Ross, J. S**, Pollock, B. B, Davis, P, James, A. N, Divol, L, Edwards, M. J, Offenberger, A. A, Price, D, Town, R. P. J, Tynan, G. R, Glenzer, S. H. "Quenching of the nonlocal electron heat transport by large external magnetic fields in a laser-produced plasma measured with imaging thomson scattering" *Phys Rev Lett* (2007) vol. 98 (13) pp. 135001

Froula, D. H, Divol, L, Meezan, N. B, Dixit, S, Neumayer, P, Moody, J. D, Pollock, B. B, **Ross, J. S**, Suter, L, Glenzer, S. H. "Laser beam propagation through inertial confinement fusion hohlraum plasmas" *Phys Plasmas* (2007) vol. 14 (5) pp. 055705

Froula, D. H, Rekow, V, Sorce, C, Piston, K, Knight, R, Alvarez, S, Griffith, R, Hargrove, D, **Ross, J. S**, Dixit, S, Pollock, B, Divol, L, Glenzer, S. H, Armstrong, W, Bahr, R, Thorp, K, Pien, G. "3ω transmitted beam diagnostic at the Omega Laser Facility" *Rev Sci Instrum* (2006) vol. 77 (10) pp. 10E507

Pollock, B. B, Froula, D. H, Davis, P. F, **Ross, J. S**, Fulkerson, S, Bower, J, Satariano, J, Price, D, Krushelnick, K, Glenzer, S. H. "High magnetic field generation for laser-plasma experiments" *Rev Sci Instrum* (2006) vol. 77 (11) pp. 114703

Schneider, M. B, Hinkel, D, Landen, O. L, Froula, D. H, Heeter, R. F, Langdon, A. B, May, M. J, McDonald, J, **Ross, J. S**, Singh, M. S, Suter, L. J, Widmann, K, Young, B. K, Baldis, H. A, Constantin, C, Bahr, R, Glebov, V. Yu, Seka, W, Stoeckl, C. "Plasma filling in reduced-scale hohlraums irradiated with multiple beam cones" *Phys Plasmas* (2006) vol. 13 (11) pp. 112701

Reighard, A. B, Drake, R. P, Donajkowski, T, Grosskopf, M, Dannenberg, K. K, Froula, D, Glenzer, S, **Ross, J. S**, Edwards, J. "Thomson scattering from a shock front" *Rev Sci Instrum* (2006) vol. 77 (10) pp. 10E504

Froula, D. H, **Ross, J. S**, Divol, L, Meezan, N, MacKinnon, A. J, Wallace, R, Glenzer, S. H. "Thomson-scattering measurements of high electron temperature hohlraum plasmas for laser-plasma interaction studies" *Phys Plasmas* (2006) vol. 13 (5) pp. 052704

Froula, D. H, **Ross, J. S**, Divol, L, Glenzer, S. H. "Thomson-scattering techniques to diagnose local electron and ion temperatures, density, and plasma wave amplitudes in laser produced plasmas" (invited). *Rev Sci Instrum* (2006) vol. 77 (10) pp. 10E522

ABSTRACT OF THE DISSERTATION

Measurements of Relativistic Effects in Collective Thomson Scattering at Electron Temperatures less than 1 keV

by

James Steven Ross

Doctor of Philosophy in Engineering Sciences (Engineering Physics)

University of California, San Diego, 2010

George Tynan, Chair

Simultaneous scattering from electron-plasma waves and ion-acoustic waves is used to measure local laser-produced plasma parameters with high spatiotemporal resolution including electron temperature and density, average charge state, plasma flow velocity, and ion temperature. In addition, the first measurements of relativistic modifications in the collective Thomson scattering spectrum from thermal electron-plasma fluctuations are presented [1]. Due to the high phase velocity of electron-plasma fluctuations, relativistic effects are important even at low electron temperatures ($T_e < 1$ keV). These effects have been observed experimentally and agree well with a relativistic treatment of the Thomson scattering form factor [2]. The results are important for the interpretation of scattering measurements

from laser produced plasmas.

Thomson scattering measurements are used to characterize the hydrodynamics of a gas jet plasma which is the foundation for a broad series of laser-plasma interaction studies [3, 4, 5, 6]. The temporal evolution of the electron temperature, density and ion temperature are measured. The measured electron density evolution shows excellent agreement with a simple adiabatic expansion model.

The effects of high temperatures on coupling to hohlraum targets is discussed [7]. A peak electron temperature of 12 keV at a density of $4.7 \times 10^{20}\text{cm}^{-3}$ are measured 200 μm outside the laser entrance hole using a two-color Thomson scattering method we developed in gas jet plasmas [8]. These measurements are used to assess laser-plasma interactions that reduce laser hohlraum coupling and can significantly reduce the hohlraum radiation temperature.

Chapter 1

Introduction

1.1 Thomson Scattering Overview

Thomson scattering is the process by which an incident electromagnetic wave is elastically scattered by a free electron ($\hbar\omega < mc^2$). The incident electromagnetic wave causes an electron to oscillate in its electric field. This oscillating electron then emits radiation at the frequency of oscillation. If the electron has an initial velocity, independent of the motion induced by the electromagnetic field, a Doppler shift will be observed [9].

If scattering is observed from an uncorrelated ensemble of electrons, the scattered spectrum is a direct measure of the velocity distribution and referred to as non-collective scattering. If the scattering is from a correlated ensemble of electrons, namely a plasma wave, the scattering is referred to as collective scattering. Two possible collective scattering modes, scattering from ion-acoustic fluctuations and scattering from electron-plasma fluctuations, are the focus of this dissertation [10, 11].

The criteria for collective scattering from ion-acoustic fluctuations is $\alpha_{IAW} > (ZT_e/3.45T_i - 1)^{-1/2}$ where the scattering parameter $\alpha_{IAW} = 1/k_a\lambda_D$, k_a is the wave number of the scattering ion-acoustic wave, λ_D is the Debye length, Z is the average charge state, T_e is the electron temperature, T_i is the ion temperature, and $-1/3.45$ is the minimum real value of the plasma dispersion function. When $\alpha_{IAW} < (ZT_e/3.45T_i - 1)^{-1/2}$ there is strong ion wave damping and the scattered

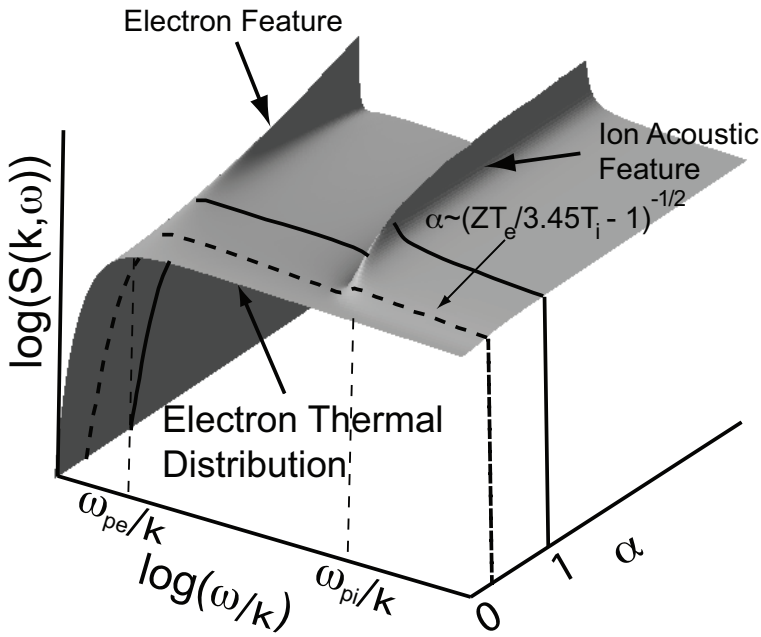

Figure 1.1: The Thomson scattering spectrum as a function of the scattering parameter. The charge state (Z=10) and the electron and ion temperatures are held constant ($T_e/T_i = 1$) while the density is varied to change the scattering parameter.

spectrum is dominated by non-collective effects. For electron-plasma waves the criteria is simply $\alpha_{EPW} > 1$, where $\alpha_{EPW} = 1/k_{epw}\lambda_D$ and k_{epw} is the wave number of the scattering electron-plasma wave. This transition from non-collective to collective scattering is shown in Figure 1.1.

1.2 History of Thomson Scattering

Until the late 19th century scientists believed atoms were the smallest form of matter, this was proven to be incorrect by J. J. Thomson when he discovered that atoms contained particles known as electrons. He was later awarded the Nobel prize in 1906 for discovering the electron. He went on to develop a theory for the scattering of electromagnetic radiation from free electrons, the process that now carries his name.

The first applications of Thomson scattering to measure plasma parameters took place in 1958. Thomson scattering from the free electrons in the ionospheric

plasma was first suggested by W. E. Gordon [12] in 1958 using a vertically directed radar pulse. Working from this suggestion later that year, Bowles made the first direct observation of electromagnetic radiation scattering from free electrons [13] by observing radar backscatter from the earth's ionosphere. He found that the width of the measured frequency spectrum was consistent with the ion temperature rather than the electron temperature. This was explained by Kahn [14] the following year as a result of Coulomb interactions between the electrons and ions. The general form of the scattering spectrum from a plasma, including Coulomb interactions, was determined independently by Fejer [15], Renau [16], Dougherty & Farley [17], and Salpeter [18].

The first reports of Thomson scattering in the laboratory used ruby lasers and were published in 1963 by Thompson & Fiocco [19], Funfer [20], and Schwarz [21]. Thompson & Fiocco were the first to report Thomson scattering in the laboratory by scattering a 20 Joule pulse off an electron beam. H.-J. Kunze, working in the group of E. Funfer, was the first to report the observation of Thomson scattering from a theta pinch plasma. Schwarz reported Thomson scattering from a hydrogen discharge plasma. These early experiments focused on demonstrating adequate signal levels for spectral analysis, in effect showing that plasma parameters measured via Thomson scattering were consistent with other diagnostic techniques.

The first application of Thomson scattering on plasma devices used in fusion research was published by Kunze in 1965. He was able to measure electron temperatures up to 215 eV on the Garching ISAR I megajoule theta pinch device [22]. By the end of 1966 Thomson scattering measurements had been published by a number of groups [23, 24, 25, 26] in multiple countries and was recognized around this time to be a proven experimental technique to measure plasma properties.

In 1969 a group led by N. Peacock used Thomson scattering to successfully measure plasma parameters on the T-3 Tokamak at the Kurchatov Institute in Moscow [27]. Thomson scattering quickly became a standard diagnostic on magnetic confinement devices and much of the development in the following years was stimulated by the magnetic fusion energy community. This continued theoretical development included the addition of magnetic fields [28], collisional effects [29],

relativistic effects [30], nonthermal plasmas [31], as well as plasma impurities [32], which were confirmed experimentally.

Relativistic effects, of special interest relating to work discussed in Sections 2.2 and 6.1, were measured from a 50 keV electron beam in 1971 by Ward [33]. Two relativistic effects, of order v/c, were attributed to the modifications to the scattered spectrum; a relativistic blue shift due to relativistic aberration and a finite-scattering volume effect. The finite-scattering volume effect, also referred to as the finite transit time effect, was later shown to be inconsistent with scattering measurements in the collective regime where the effect was attributed to electrons interacting with the magnetic field of the Thomson scattering probe beam [1]. A complete treatment of relativistic modifications to the collective Thomson scattering spectrum was reported in 2010 by J. Palastro [2].

1.3 Thomson Scattering from Inertial Confinement Fusion Plasmas

Inertial confinement fusion (ICF) is the process of compressing and heating a target until it reaches temperatures and density at which nuclear fusion can occur. This process is currently being studied at a number of laboratories around the world, most notably the National Ignition Facility (NIF) at Lawrence Livermore National laboratory. There are two primary goals for the NIF, the first is to develop the technical understanding required to design a laser-driven fusion power plant for energy generation and the second goal is to promote stockpile stewardship by recreating conditions in the laboratory that can only be found in stars or detonating nuclear weapons. Both of these goals require a burning fusion target. The standard ICF target is a spherical capsule filled with a mix of deuterium and tritium that is bombarded with electromagnetic radiation. As the outer layer of the capsule is heated it begins to ablate material which then results in a force that compresses and heats the target. If the target is compressed symmetrically to high temperatures and densities a central hotspot can reach the conditions required for nuclear fusion. Once this central core is burning it will heat the nearby material, which is confined

near the central core by its own inertia, hence the name inertial confinement fusion. The nearby fuel, once heated, will undergo fusion. The goal is to burn a significant fraction of the fuel, this is called ignition.

There are two main approaches to ICF, direct drive and indirect drive. Both most typically use high-energy lasers to create the high-energy density conditions required for fusion. In the direct drive approach, the lasers directly heat the fusion capsule. The indirect drive approach uses a hohlraum, or radiation cavity, to convert laser light to x-rays which then heat the fusion capsule. While the use of a hohlraum reduces the laser-target coupling efficiency it significantly improves implosion symmetry. The indirect drive approach to ignition is currently being pursued on the National Ignition Facility at Lawrence Livermore National Laboratory where credible attempts at ignition are scheduled for 2011. A schematic of the NIF target design is shown in Figure 1.2.

Thomson scattering from inertial confinement fusion hohlraum plasmas was pioneered by S. Glenzer on the Nova Laser Facility [34]. Using Thomson scattering he was able to measure the electron and ion temperatures as well as the plasma flow velocity inside a gas-filled hohlraum [35]. These measurements were used to benchmark hydrodynamic simulations and are important for understanding the physical processes that take place inside the hohlraum. The high-density, high-temperature conditions found inside hohlraums typically result in collective Thomson scattering. The parameter spaces accessible by the Janus Laser, the Omega Laser, and the NIF are shown in Figure 1.3. A majority of the accessible parameter space falls in the collective Thomson scattering regime.

1.4 Summary of Experimental Results

A series of experiments completed at the Jupiter Laser Facility and the Laboratory for Laser Energetics are presented in this dissertation. The goal was to determine plasma parameters to study plasma [8] as well as laser-plasma behavior [36, 37] and to demonstrate Thomson scattering in plasmas relevant to Inertial Confinement Fusion.

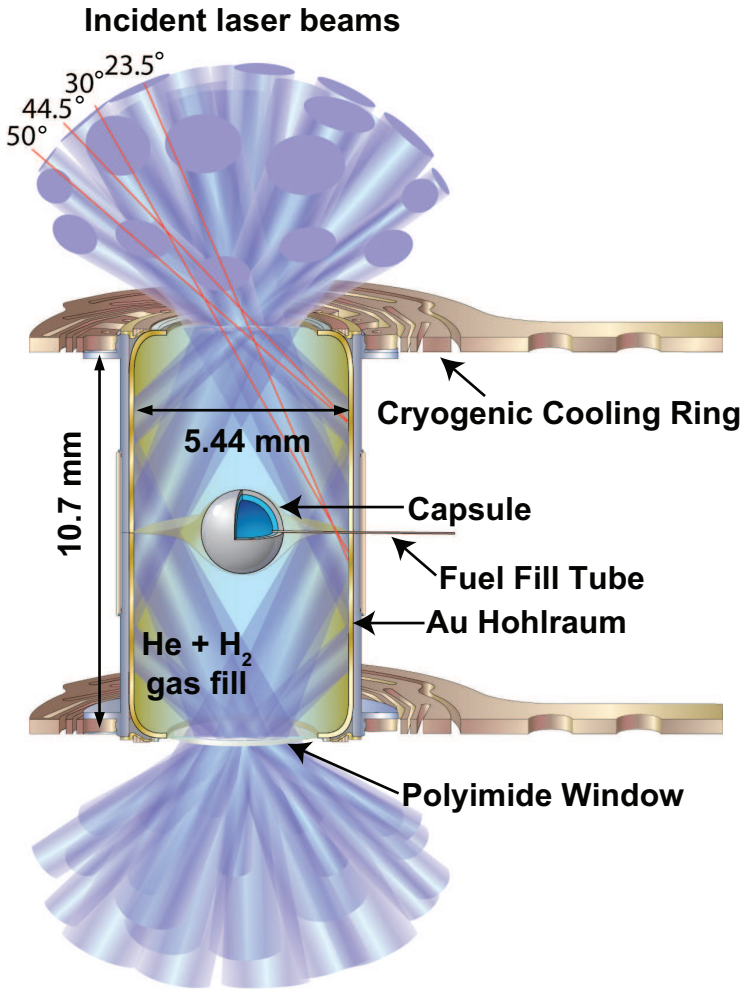

Figure 1.2: A NIF Au hohlraum target is shown. The hohlraum surounds the spherical fuel capsule. 192 laser beams heat the gold walls which then emit x-rays which in turn ablate material from the fuel capsule. A mix of helium and hydrogen fill the hohlraum to slow the collapse of the gold walls. Cryogenic cooling rings are used to cool the target to 18 K. Image courtesy of LLNL.

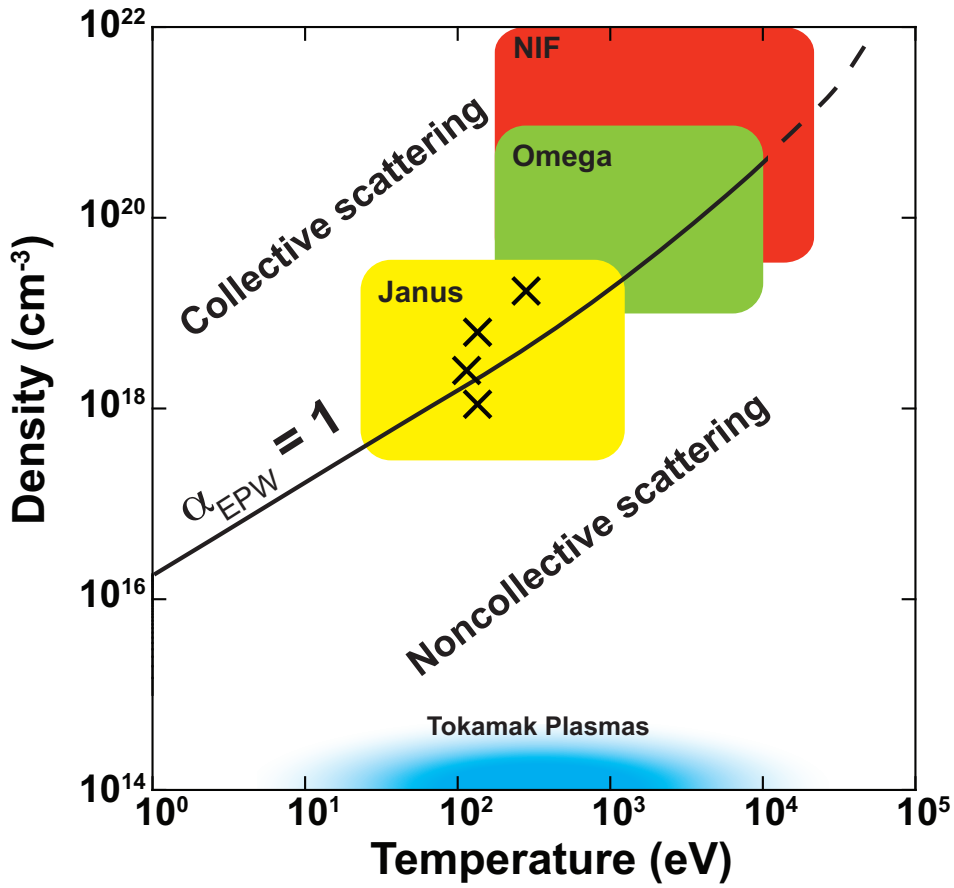

Figure 1.3: Thomson scattering is collective for most laser produced plasmas. The solid black line shows where $\alpha_{EPW} = 1$ assuming a 2ω probe beam and 90° scattering. The accessible parameter space for 3 different laser systems are shown. The black X's correspond to the data shown in Figure 4.1.

Simultaneous Thomson scattering measurements of light scattered from ion-acoustic and electron plasma fluctuations in a N_2 gas jet plasma are presented from the Jupiter Laser Facility. By varying the plasma density from 1.5×10^{18} cm^{-3} to 4.0×10^{19} cm^{-3} and the temperature from 100 eV to 600 eV the transition from the collective regime ($\alpha_{EPW} > 1$) to the non-collective regime ($\alpha_{EPW} < 1$) in the electron feature is observed. These measurements allow an accurate local measurement of fundamental plasma parameters: plasma fluid flow, electron temperature, density, and ion temperature. These experiments demonstrated the first relativistic effects on a collective scattering experiment and show that relativistic effects in collective scattering are governed by the phase velocity of the wave. Therefore, it is shown that even at low temperatures, relativistic corrections to the scattered power must be included.

At the Laboratory for Laser Energetics, Thomson scattering measurements were made on hohlraum and foil targets. The electron temperature and density were measured 200 μm outside the laser entrance hole of a high temperature hohlraum using multiple-wavelength Thomson scattering [8]. This region is of critical importance for the coupling of the laser beams to the hohlraum and for the production of hohlraum radiation temperatures of $T_R \gtrsim 300$ eV [7]. The electron temperature was measured from 11.8 keV to 2.9 keV, with the maximum temperature observed 100ps before the termination of the heater beams. The electron density was measured simultaneously and ranged from 1.0×10^{21} cm^{-3} to 4.7×10^{20} cm^{-3}. These measurements were made in the $\alpha \sim 1$ regime where multiple-wavelength Thomson scattering from the ion-acoustic feature is used to make an accurate measurement of the electron temperature and density.

Thomson scattering from both ion-acoustic waves and electron plasma waves was measured from a Vanadium foil target. These are the first collective Thomson scattering measurements of the electron feature using a 4ω probe beam. The electron temperature and density are measured 400 μm from the target surface. Once this technique is perfected it will be possible to directly measure the average ionization state as a function of temperature in high-Z materials. Previous Thomson scattering measurements typically assume an average ionization state based on

hydrodynamic simulations [38, 36], use a Thomas-Fermi ionization model [3], or use spectroscopy to bound the possible range of ionization states. Very few measure the average ionization state in the Thomson scattering volume [39], and it has never been accomplished with a 4ω probe. The advantages and disadvantages of a 4ω probe are also discussed.

Chapter 2

Thomson Scattering

Collective Thomson scattering is the process of scattering from density fluctuations in the plasma. The standard approach to access these density fluctuations utilizes the Vlasov equation to develop a two fluid model for the plasma. This method is valid when the criteria $N_D >> 1$ [40], where $N_D = 1.7 \times 10^9 (T_e^3/n_e)^{1/2}$ is the number of particles in the Debye sphere, is satisfied. In this case, collective effects are dominant for particle motion and wave field generation. For all of the results presented in this dissertation $N_D > 250$ and fine scale collisional interactions will be ignored. Using the two fluid model where the electrons are one fluid and the ions the other, there are two naturally occurring charge density fluctuations in a plasma (assuming no imposed magnetic fields). These fluctuations have a characteristic frequency determined by the electrons and/or ions. The fluctuations correspond to two plasma waves, a high frequency wave called the electron-plasma wave and a low frequency wave called the ion-acoustic wave. Using the fluid equations the dispersion relation for the electron plasma wave is,

$$\omega^2 = \omega_p^2 + 3v_{th}^2 k^2, \tag{2.1}$$

where $v_{th} = \sqrt{T_e/m_e}$ and ω_p is the plasma frequency. For the ion-acoustic wave,

$$\omega = \pm k \sqrt{\frac{T_e}{M}\left[\frac{Z}{(1+k^2\lambda_D^2)} + \frac{3T_i}{T_e}\right]} \tag{2.2}$$

where T_e is the electron temperature, T_i is the ion temperature, M is the ion mass, and Z is the charge state.

It is important to note that the amplitude of these fluctuations can be affected by collisionless Landau damping. Using the Vlasov equation the damping rate for electron plasma waves can be derived [40],

$$\frac{\gamma}{\omega} = \frac{\pi}{2}\frac{\omega_p^2}{k^2}\frac{\partial}{\partial v}\bar{f}\left(\frac{\omega}{k}\right) \tag{2.3}$$

where γ is the damping rate, $\bar{f} = f/n_e$, f is the particle distribution function, and n_e is the electron density. In the case of a Maxwellian distribution,

$$\frac{\gamma}{\omega} = -\sqrt{\frac{\pi}{8}}\frac{\omega_p^2\omega}{|k^3|\, v_{th}^3}\exp\left(-\frac{\omega^2}{2k^2v_{th}^2}\right), \tag{2.4}$$

where it is important to note that the damping rate is highly sensitive to the phase velocity (ω/k) and the thermal velocity (v_{th}). This sensitivity will be exploited in Section 4.1 to measure the electron temperature and density from electron-plasma wave fluctuations.

Thomson scattering from these density fluctuations is governed by the following equations,

$$\omega = \omega_s - \omega_0, \tag{2.5}$$

$$\vec{k} = \vec{k}_s - \vec{k}_0, \tag{2.6}$$

where Eq. (2.5) relates to conservation of energy and Eq. (2.6) to conservation of momentum. By prudent selection of the scattering geometry it is possible to observe Thomson scattering from collective plasma behavior, i.e. ion-acoustic waves and electron plasma waves. In the case of scattering from ion-acoustic waves, the observed radiation is Doppler shifted by an amount proportional to the ion-acoustic sound speed plus any shift from bulk plasma motion. When scattering from electron-plasma waves, the shift is proportional to the electron-plasma wave frequency. In this regime, the observed radiation is preferentially scattered from electrons traveling near the phase velocity of the wave which will be discussed in Section 2.3.

A typical scattering geometry is shown in Fig. 2.1 where an incident laser with wave number k_0 interacts with a plasma wave with wave number k. The resulting scattered light is observed at an angle θ from the incident light and has a wave number k_s.

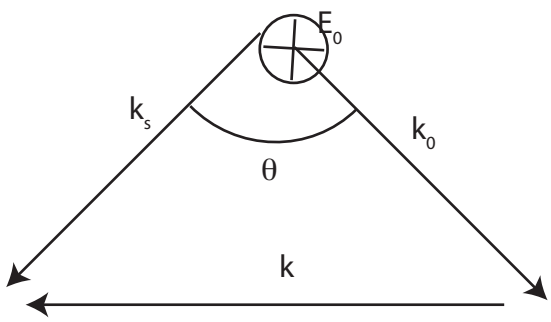

Figure 2.1: A typical Thomson scattering scattering geometry where the electron field of the incident laser ($\vec{E}_0$) is perpendicular to the direction of observation ($\vec{k}_0$).

2.1 Scattered Power Spectrum

A derivation of the Thomson scattered power spectrum including first order terms of v/c, typically called the first order relativistic form factor, is presented following the approached of Ref. [2]. The derivation assumes an incident plane electric field with an amplitude small enough such that the original trajectory of an electron is only slightly modified.

$$\vec{E}_i = \vec{E_{i,0}} \cos(\vec{k}_i \cdot \vec{r} - \omega_i t'), \tag{2.7}$$

where $\vec{k}_i$ and ω_i are the wavenumber and frequency of the incident electromagnetic wave, and t' refers to the retarded time, i.e. the time measured in the electron's frame. Time in the observation frame will be referred to as t. For simplicity we choose our observation of the scattered field in the plane perpendicular to the incident electric field as shown in Fig 2.1. Defining $\vec{k}_s$ as the wavenumber of the scattered electromagnetic wave, we can write both $\vec{k}_s \cdot \vec{E}_i = 0$ and $\vec{k}_i \cdot \vec{E}_i = 0$. We also define $\hat{s}$, $\hat{i}$, and $\hat{e}$ as unit vectors along $\vec{k}_s$, $\vec{k}_i$, and $\vec{E}_i$ respectively. The components of the normalized electron velocity, $\vec{\beta} = \vec{v}/c$, are then $\beta_s = \hat{s} \cdot \vec{\beta}$, $\beta_i = \hat{i} \cdot \vec{\beta}$, and $\beta_E = \hat{e} \cdot \vec{\beta}$ and $\cos\theta = \hat{i} \cdot \hat{s}$. If the calculations are limited to an observation distance, R defined as the distance from an origin in the scattering region to the observer, much larger than both the distance traversed by a charge during the observation time, T, and the sample size, L, only the scattered far field of the electron needs to be considered ($R >> cT, R >> L$). Under these assumptions the retarded time, t', can be written in terms of the observation time,

t, as follows:

$$t' = t - \frac{R}{c} + \frac{\hat{s}}{c} \cdot \vec{r}(t), \tag{2.8}$$

where $\vec{r}(t)$ is the position of the electron in the observation frame relative to an origin in the scattering region. The scattered electric field due to one electron is then in this far field approximation,

$$\vec{E}_s(R,t) = \frac{r_e}{R} E_{i,0} \vec{G}(\vec{\beta}) \cos(\vec{k_i} \cdot \vec{r} - \omega_i t') \tag{2.9}$$

where r_e is the classical electron radius. The factor $\vec{G}(\vec{\beta})$ is the velocity dependent geometric factor

$$\begin{aligned} \vec{G}(\vec{\beta}) = \frac{(1-\beta^2)^{1/2}}{(1-\beta_s)^3} \Big[& (1-\beta_s)(1-\beta_i)\hat{e} - (\cos\theta - \beta_s)\beta_E \hat{s} \\ & + (1-\beta_s)\beta_E \hat{i} - (1-\cos\theta)\beta_E \hat{\beta} \Big] \end{aligned} \tag{2.10}$$

and $\vec{G}(\vec{\beta})$ is to be evaluated in the retarded frame. A proper treament of $\vec{G}(\vec{\beta})$ is required for a fully relativistic Thomson scattering form factor [2]. Here the treatment has been simplified by limiting $\vec{G}(\vec{\beta})$ to terms of order β, assuming the scattering plane is perpendicular to the electric field, and that we select only the part of the scattered electric field parallel to $\hat{e}$ [11]:

$$\vec{G}(\vec{\beta}) \approx (1 + 2\beta_s - \beta_i)\hat{e} - \cos\theta \beta_E \hat{s} + \beta_E \hat{i}. \tag{2.11}$$

Eq. (2.9) describes the scattered electric field for a single particle. To calculate the scattering from a volume of plasma a sum over all of the particles is required. The Klimontovich distribution, which describes precisely the position and velocity of all particles in the plasma, is expressed as

$$F_e(\vec{r}, \vec{v}, t') = \sum_j \delta[\vec{r} - \vec{r}_j(t)] \delta[\vec{v} - \vec{v}_j(t)] \delta\left(t' - t + \frac{R}{c} - \frac{\hat{s}}{c} \cdot \vec{r}_j(t)\right). \tag{2.12}$$

The total scattered electric field is then written as the sum of the scattered electric fields due to each available scatterer in a volume V. Using Eq. (2.11) in Eq. (2.9) and then integrating over the Klimontovich distribution function the total scattered field is then,

$$\vec{E}_s^T(R,t) = \frac{r_e}{R} E_{i,0} \int_V dx^3 \int d\vec{v} \vec{G}(\vec{\beta}) F_e(\vec{r}, \vec{v}, t') \cos(\vec{k_i} \cdot \vec{r} - \omega_i t'), \tag{2.13}$$

where the superscript T refers to total. The time averaged scattered power for a given scattered frequency is then given as,

$$P_s(R,\omega_s) = \frac{cR^2}{4\pi^2}\lim_{\gamma\to 0}\gamma\int_{\omega_s-\Delta\omega_s/2}^{\omega_s+\Delta\omega_s/2} d\omega_s \left|\int_0^\infty dt\vec{E}_s^T(t)e^{-(\gamma+i\omega_s)t}\right|^2, \tag{2.14}$$

where Eq. (2.13) is used for $\vec{E}_s^T(t)$, $\omega_s \pm \Delta\omega_s/2$ is the scattered frequency integral to reflect the frequency interval measured by a detector and γ is a real number introduced by the inverse Laplace transform.

We seek to evaluate the Laplace transform of $E_s^T(t)$ appearing in Eq. (2.14), which we can write as $L_{\omega_s}\left[\vec{E}_s^T(t)\right] = \int dt\vec{E}_s^T(t)e^{-(\gamma+i\omega_s)t}$, by substituting Eq. (2.13) for $E_s^T(t)$, then

$$L_{\omega_s}\left[\vec{E}_s^T(t)\right] = \frac{r_e}{2R}E_{i,0}\int_0^\infty dt'\int_V dx^3\int d\vec{v}(1-\beta_s)\vec{G}(\vec{\beta})F_e(\vec{r},\vec{v},t')\Big[e^{i\vec{k}_+\cdot\vec{r}-i\omega_+t'} + e^{i\vec{k}_-\cdot\vec{r}-i\omega_-t'}\Big] \tag{2.15}$$

and the frequency and wave numbers are defined as follows: $\vec{k}_+ = \vec{k}_s + \vec{k}_i$, $\vec{k}_- = \vec{k}_s - \vec{k}_i$, $\vec{\omega}_+ = \vec{\omega}_s + \vec{\omega}_i$, and $\vec{\omega}_- = \vec{\omega}_s - \vec{\omega}_i$. Noting that the integrals over time and space are Laplace and Fourier transforms respectively, we find

$$L_{\omega_s}\left[\vec{E}_s^T(t)\right] = \frac{r_e}{2R}E_{i,0}\int d\vec{v}(1-\beta_s)\vec{G}(\vec{\beta})\left[F_e(\vec{k}_+,\vec{v},\omega_+ + i\gamma) + F_e(\vec{k}_-,\vec{v},\omega_- + i\gamma)\right]. \tag{2.16}$$

where $F_e\left(\vec{k},\vec{v},\omega+i\gamma\right)$ is the Fourier and Laplace transform of $F_e\left(\vec{r},\vec{v}\,t'\right)$ from Eq. (2.15). The Laplace transforms have been performed assuming a positive scattered frequency, $\omega_s > 0$. Allowing ω_s to range over both positive and negative values, we have

$$L_{\omega_s}\left[\vec{E}_s^T(t)\right] = \frac{r_e}{2R}E_{i,0}\int d\vec{v}(1-\beta_s)\vec{G}(\vec{\beta})F_e(\vec{k},\vec{v},\omega+i\gamma), \tag{2.17}$$

where we have dropped the $\pm$ subscripts, and $\omega = \omega_s - \omega_i$ and $\vec{k} = \vec{k}_s - \vec{k}_i$. Eq. (2.17) can now be substituted back into Eq. (2.14) and we find the scattered power spectrum to be

$$P_s(R,\omega_s) = \frac{P_i r_e^2}{2\pi^2 a}\lim_{\gamma\to 0}\gamma\left|\int d\vec{v}(1-\beta_s)\vec{G}(\vec{\beta})F_e(\vec{k},\vec{v},\omega+i\gamma)\right|^2, \tag{2.18}$$

where $P_i = (cE_{i0}^2/8\pi)a$, and a is the cross-sectional area of the incident beam. We can now insert Eq. (2.11) into Eq. (2.18) and, only keeping terms of order β, the scattered power then becomes,

$$P_s(R,\omega_s) = \frac{P_i r_e^2}{2\pi^2 a} \lim_{\gamma\to 0} \gamma \left| \int d\vec{v} \left[(1+\beta_s - \beta_i)\hat{e} - \cos\theta\beta_E \hat{s} + \beta_E \hat{i} \right] F_e(\vec{k},\vec{v},\omega + i\gamma) \right|^2 . \tag{2.19}$$

For simplicity the integrand of Eq. (2.19) can be written in terms of the following three vectors,

$$\vec{H}_e \equiv \hat{e} \int (1+\beta_s - \beta_i) F_e(\vec{k},\vec{v},\omega) d\vec{v} \tag{2.20}$$

$$\vec{H}_s \equiv -\hat{s} \int \cos\theta\beta_E F_e(\vec{k},\vec{v},\omega) d\vec{v} \tag{2.21}$$

$$\vec{H}_i \equiv \hat{i} \int \beta_E F_e(\vec{k},\vec{v},\omega) d\vec{v}, \tag{2.22}$$

and becomes,

$$P_s(R,\omega_s) = \frac{P_i r_e^2}{2\pi^2 a} \lim_{\gamma\to 0} \gamma \left| \vec{H}_e + \vec{H}_s + \vec{H}_i \right|^2 . \tag{2.23}$$

$\vec{H}_e$, $\vec{H}_s$ and $\vec{H}_i$ are the components of the scattered electric field in the $\hat{e}$, $\hat{s}$ and $\hat{i}$ directions respectively for the electrons evolving under the classical Lorentz force of the incident wave. Using our conditions that $\hat{e}\cdot\hat{i} = 0$ and $\hat{e}\cdot\hat{s} = 0$ there are four terms that need to be considered in the scattered power: $|\vec{H}_e|^2$, $|\vec{H}_s|^2$, $|\vec{H}_i|^2$, and $|\vec{H}_s \cdot \vec{H}_i|$. Of these terms only $|\vec{H}_e|^2$ results in a term of order β. $|\vec{H}_s|^2$, $|\vec{H}_i|^2$, and $|\vec{H}_s \cdot \vec{H}_i|$ result in terms that are second order in β and will be ignored. The scattered power to first order in β is now simply,

$$P_s(R,\omega_s) = \frac{P_i r_e^2}{2\pi^2 a} \lim_{\gamma\to 0} \gamma \left| \vec{H}_e \right|^2 . \tag{2.24}$$

In order to evaluate Eq. (2.24) we derive an expression for $F_e(\vec{k},\vec{v},\omega)$ that does not require explicit knowledge of the position and velocity of every electron in the system at all times. Expressing the total distributions F_e and F_i as a sum of the average system state $F_{0e} = n_{0e} f_{0e}(\vec{v})$ and $F_{0i} = n_{0i} f_{0i}(\vec{v})/Z$ plus a fluctuation contribution, F_{1q}, we have,

$$F_e = n_{0e} f_{0e}(\vec{v}) + F_{1e} \tag{2.25}$$

$$F_i = n_{0i} f_{0i}(\vec{v}) Z^{-1} + F_{1i}. \tag{2.26}$$

The equilibrium plasma is taken to be charge neutral such that $\int (f_{0e} - f_{0i}) d\vec{v} = 0$, where f_{0x} is the total distribution normalized by the density and charge state. The Klimontovich system is composed of the collisionless Klimontovich equation

$$\left(\frac{\partial}{\partial t} + \vec{v} \cdot \nabla + \frac{q\vec{E}_f}{m_q} \cdot \nabla_p \right) F_q = 0 \tag{2.27}$$

where ∇_p is the gradient along the momentum direction, and Poisson's equation

$$\nabla \cdot \vec{E}_f = 4\pi e \int (ZF_{1i} - F_{1e}) d\vec{v}, \tag{2.28}$$

where $\vec{E}_f$ is the electrostatic field generated by thermal fluctuations. Here the relativistic Vlasov equation, Eq. (2.27), is written in terms of the momentum gradient ∇_p and not the velocity gradient ∇_v. As a result, the F_q appearing in Eq. (2.27) is actually the momentum distribution, which can be transformed to the velocity distribution via a Jacobian transformation. When an integration is over the coordinates $d\vec{v}$ or $d\vec{p}$ the distributions are understood to be velocity or momentum distributions respectively. The operator ∇_p is also understood to act on the momentrum distribution.

To find F_{1q}, we insert Eqs. (2.25) and (2.26) into Eq. (2.27) and linearize with respect to the fluctuating field amplitude. We find that the fluctuating component of the distribution function can be expressed as follows:

$$F_{1q}(\vec{k}, \vec{v}, \omega) = -i \frac{F_{1q}(\vec{k}, \vec{v}, t = 0)}{\omega - \vec{k} \cdot \vec{v} - i\gamma} - \frac{4\pi q}{mk^2} \frac{n_{0q} \rho_1(\vec{k}, \omega) \vec{k} \cdot \nabla_p f_{0q}}{\omega - \vec{k} \cdot \vec{v} - i\gamma} \tag{2.29}$$

where $\rho_1(\vec{k}, \omega)$ is the spectral fluctuation density

$$\rho_1(\vec{k}, \omega) = Zen_{1i}(\vec{k}, \omega) - en_{1e}(\vec{k}, \omega) \tag{2.30}$$

and $n_{1i}(\vec{k}, \omega)$ and $n_{1e}(\vec{k}, \omega)$ are the Fourier transforms for their respective density perterbations.

We continue our calculation of the scattered power by inserting Eq. (2.29) into Eq. (2.20) which becomes,

$$\vec{H}_e = -i\hat{e} \int (1 + \beta_s - \beta_i) \left[\frac{F_{1q}}{\omega - \vec{k} \cdot \vec{v} - i\gamma} d\vec{v} + \frac{4\pi q}{mk^2} \frac{n_{0q} \rho_1(\vec{k}, \omega) \vec{k} \cdot \nabla_p f_{0q}}{\omega - \vec{k} \cdot \vec{v} - i\gamma} d\vec{p} \right]. \tag{2.31}$$

This equation can be rewritten,

$$\vec{H}_e = -i\hat{e}\sum_{j=1}^{N}(1+\beta_s-\beta_i)\frac{e^{-i\vec{k}\cdot\vec{r}_j(0)}}{\omega-\vec{k}\cdot\vec{v}-i\gamma}d\vec{v} - \hat{e}\frac{X_e}{e}\rho_1(\vec{k},\omega) \tag{2.32}$$

where we have defined

$$X_e \equiv \frac{4\pi q}{mk^2}\int(1+\beta_s-\beta_i)\frac{n_{0q}\vec{k}\cdot\nabla_p f_{0q}}{\omega-\vec{k}\cdot\vec{v}-i\gamma}d\vec{p}, \tag{2.33}$$

which is analogous to the classical electron susceptibility. Now we can derive an expression for $|\vec{H}_e|^2$ using the following expression for $\rho_1(\vec{k},\omega)$ where the sum over l is for the ions,

$$\rho_1(\vec{k},\omega) = -\frac{ie}{\epsilon}\left[\sum_{j=1}^{N}\frac{e^{-i\vec{k}\cdot\vec{r}_j(0)}}{\omega-\vec{k}\cdot\vec{v}_j-i\gamma} - Z\sum_{l=1}^{N/Z}\frac{e^{-i\vec{k}\cdot\vec{r}_l(0)}}{\omega-\vec{k}\cdot\vec{v}_l-i\gamma}\right] \tag{2.34}$$

Inserting this equation into Eq. (2.32) and taking the magnitude squared leads to the following expression,

$$\begin{aligned}
|\vec{H}_e|^2 = &\sum_{j=1}^{N}(1+\beta_s-\beta_i)\frac{e^{-i\vec{k}\cdot\vec{r}_j(0)}}{\omega-\vec{k}\cdot\vec{v}_j-i\gamma}\sum_{n=1}^{N}(1+\beta_s-\beta_i)\frac{e^{i\vec{k}\cdot\vec{r}_n(0)}}{\omega-\vec{k}\cdot\vec{v}_n+i\gamma} \\
&+\left|\frac{X_e}{\epsilon}\right|^2\left|\sum_{j=1}^{N}\frac{e^{-i\vec{k}\cdot\vec{r}_j(0)}}{\omega-\vec{k}\cdot\vec{v}_j-i\gamma} - Z\sum_{l=1}^{N/Z}\frac{e^{-i\vec{k}\cdot\vec{r}_l(0)}}{\omega-\vec{k}\cdot\vec{v}_l-i\gamma}\right|^2 \\
&-\frac{X_e}{\epsilon}\left(\sum_{j=1}^{N}\frac{e^{-i\vec{k}\cdot\vec{r}_j(0)}}{\omega-\vec{k}\cdot\vec{v}_j-i\gamma} - Z\sum_{l=1}^{N/Z}\frac{e^{-i\vec{k}\cdot\vec{r}_l(0)}}{\omega-\vec{k}\cdot\vec{v}_l-i\gamma}\right)\sum_{n=1}^{N}(1+\beta_s-\beta_i)\frac{e^{i\vec{k}\cdot\vec{r}_n(0)}}{\omega-\vec{k}\cdot\vec{v}_n+i\gamma} \\
&-\frac{X_e^*}{\epsilon^*}\left(\sum_{j=1}^{N}\frac{e^{i\vec{k}\cdot\vec{r}_j(0)}}{\omega-\vec{k}\cdot\vec{v}_j+i\gamma} - Z\sum_{l=1}^{N/Z}\frac{e^{i\vec{k}\cdot\vec{r}_l(0)}}{\omega-\vec{k}\cdot\vec{v}_l+i\gamma}\right)\sum_{j=1}^{N}(1+\beta_s-\beta_i)\frac{e^{-i\vec{k}\cdot\vec{r}_j(0)}}{\omega-\vec{k}\cdot\vec{v}_j-i\gamma}.
\end{aligned} \tag{2.35}$$

Assuming electrons and ions are spatially uncorrelated, which is reasonable given the Debye shielding present in the plasma, allows us to drop the cross terms in the summations. Defining,

$$h_q(\vec{k},\vec{v},\omega) \equiv \frac{f_{q0}(\vec{v})}{(\omega-\vec{k}\cdot\vec{v})^2+\gamma^2} \tag{2.36}$$

and grouping terms we find,

$$\frac{|\vec{H}_e|^2}{N} = \int d\vec{v} \left|(1+\beta_s-\beta_i) - \frac{X_e}{\epsilon}\right|^2 h_e + Z\left|\frac{X_e}{\epsilon}\right|^2 \int d\vec{v} h_i. \tag{2.37}$$

The scattered power is then,

$$P_s(R,\omega_s) = \frac{P_i N r_e^2}{2\pi^2 a} \lim_{\gamma\to 0} \gamma \int d\vec{v} \left|(1+\beta_s-\beta_i) - \frac{X_e}{\epsilon}\right|^2 h_e + Z\left|\frac{X_e}{\epsilon}\right|^2 \int d\vec{v} h_i. \tag{2.38}$$

In the first order β limit, the Doppler shifted scattered frequency can be related to the incident frequency via the relation $\omega_s(1-\beta_s) = \omega_i(1-\beta_i)$ [10] which leads to the following relation, $\beta_s - \beta_i \approx (\omega/\omega_i)$ and in this limit $X_e \approx \chi_e(1+\frac{\omega}{\omega_i})$, where the electron and ion susceptibility, χ_q, is defined as follows,

$$\chi_q = \int d\vec{v} \frac{4\pi e^2 n_q}{m_q k^2} \frac{\vec{k}\cdot\partial f_{q0}/\partial\vec{v}}{\omega - \vec{k}\cdot\vec{v} - i\gamma}. \tag{2.39}$$

Using these approximations Eq. (2.38) becomes,

$$\begin{aligned} P_s(R,\omega_s) = \frac{P_i N r_e^2}{2\pi a} \lim_{\gamma\to 0} \gamma \int d\vec{v} \left|\left(1+\frac{\omega}{\omega_i}\right) - \frac{\chi_e}{\epsilon}\left(1+\frac{\omega}{\omega_i}\right)\right|^2 h_e \\ + Z\left|\frac{\chi_e}{\epsilon}\left(1+\frac{\omega}{\omega_i}\right)\right|^2 \int d\vec{v} h_i. \end{aligned} \tag{2.40}$$

where the term $(1+\omega/\omega_i)^2$ is independent of the integration and again keeping only first order terms becomes, $(1+2\omega/\omega_i)$. The arguments of both integrals are now simply h_q and in the limit when γ goes to zero the scattered power is,

$$P_s(R,\omega_s) = \frac{P_i N r_e^2}{2ak}\left(1+2\frac{\omega}{\omega_i}\right)\left[\left|1-\frac{\chi_e}{\epsilon}\right|^2 f_{e0}(\beta_k) + Z\left|\frac{\chi_e}{\epsilon}\right|^2 f_{i0}(\beta_k)\right], \tag{2.41}$$

where $\beta_k = \omega/kc$. Using the longitudinal dielectric function $\epsilon = 1+\chi_e+\chi_i$ the scattered power can be written in the form presented by Sheffield [10],

$$P_s(R,\omega_s) = \frac{P_i N r_e^2}{2ak}\left(1+2\frac{\omega}{\omega_i}\right)\left[\left|\frac{1+\chi_i}{\epsilon}\right|^2 f_{e0}(\beta_k) + Z\left|\frac{\chi_e}{\epsilon}\right|^2 f_{i0}(\beta_k)\right], \tag{2.42}$$

which is the Thomson scattering spectra correct to first order in beta. The non-relativistic Thomson scattered power spectrum [15, 11] is,

$$P_{\mathrm{nr}}(k,\omega) = \frac{P_i r_e^2 N}{2ak}\left[\left|\frac{1+\chi_i}{\varepsilon}\right|^2 f_{e0}(\beta_k) + Z\left|\frac{\chi_e}{\varepsilon}\right|^2 f_{i0}(\beta_k)\right]. \tag{2.43}$$

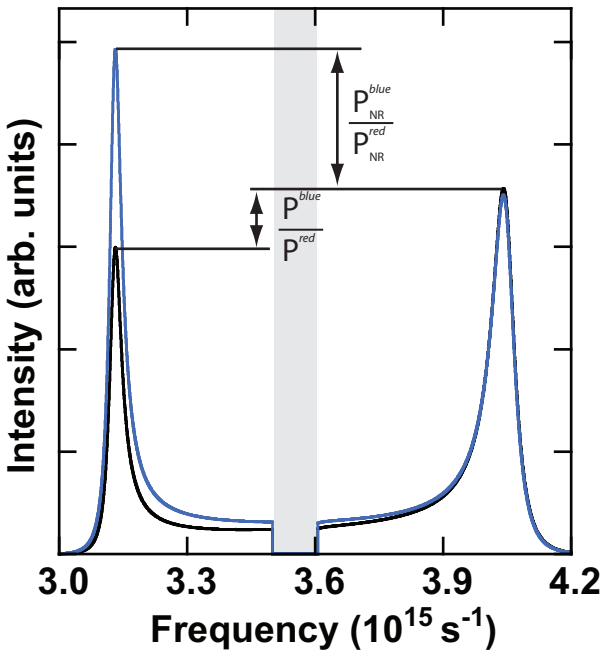

Figure 2.2: The high frequency spectrum is calculated using the relativistic treatment (Eq. 2.42, black line) and the non-relativistic treatment (Eq. 2.43, blue line). Both calculations use an electron density of 4×10^{19} cm^{-3}, an electron temperature of 410 eV and a scattering angle of 90°. The scattering parameter for these conditions is $\alpha = 2.5$. The low frequency feature has been suppressed.

Comparing Eq. (2.42) and (2.43), we see that the first order beta correction is given by the term $1 + 2\omega/\omega_i$ which is discussed in detail in Section 2.2. Figure 2.2 shows a comparison of Eq. (2.42) and (2.43). Both calculated spectra are normalized to the high frequency, blue shifted, peak.

2.2 First Order Relativistic Correction

The first order relativistic correction $(1+2\omega/\omega_i)$ in the asymmetric scattering spectrum and can be attributed to two effects. The first effect is due to relativistic aberration, also referred to as the relativistic "headlight" effect (Fig. 2.3), where light is preferentially directed in the emitter's direction of propagation [41]. The change in intensity assuming a source that is isotropic in the co-moving frame

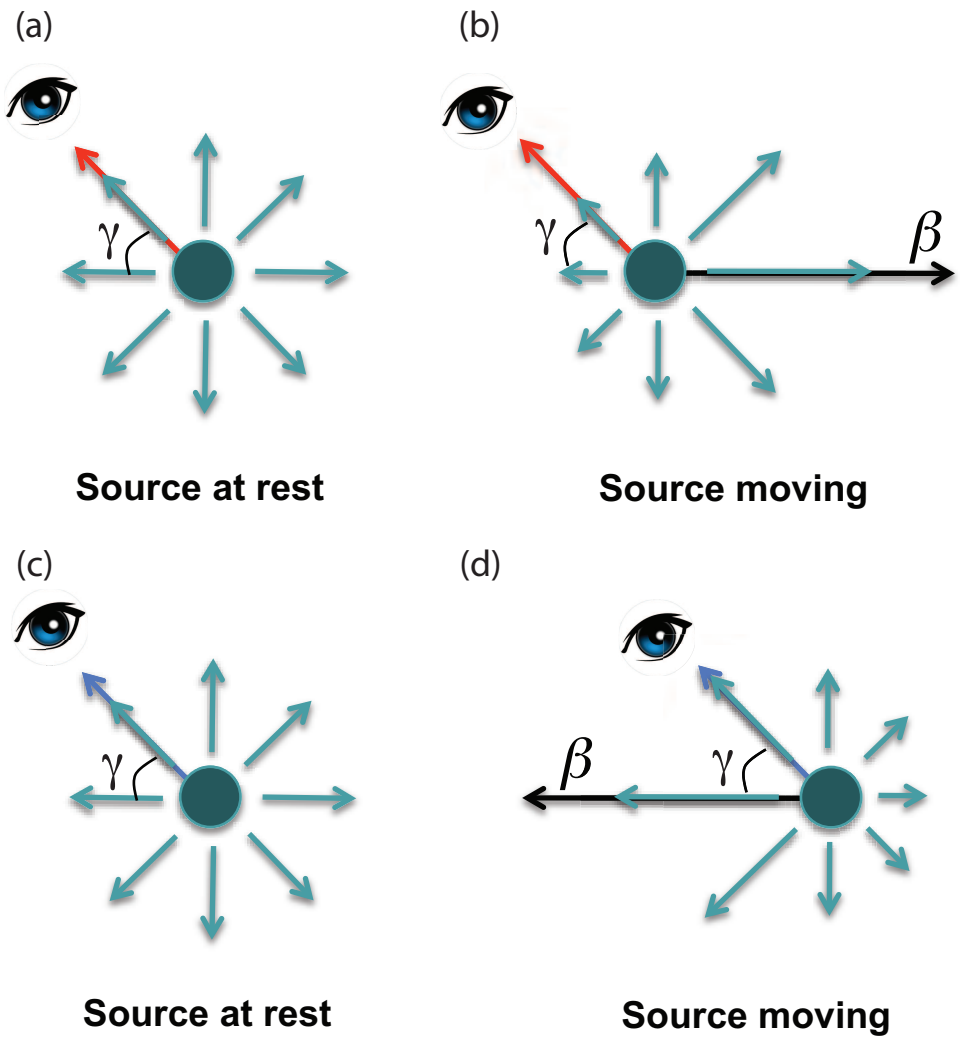

Figure 2.3: The effect of relativistic aberration is shown on a source that emits uniformly at rest (a, c). The angle between the direction of observation and the direction the source is moving is given by γ. When the source is moving to the right (b) the scattered light intensity in the direction of the observer decreases. When the source is moving to the right (d) the observer sees an increase in intensity.

can be derived from the Lorentz transformation and is expressed,

$$\frac{I(\gamma)}{I_0} = \frac{1-\beta^2}{(1+\beta\cos\gamma)^2}, \tag{2.44}$$

where I_0 is the initial intensity, γ is the angle between the direction of motion and observation, and β is the normalized velocity of the source. Making the assumption that the red shifted and blue shifted resonances are caused by sources traveling at the same speed but moving in opposite directions, the ratio between the two resonances due to relativistic aberration becomes,

$$\frac{I_{blue}}{I_{red}} = \frac{(1+\beta\cos\gamma)^2}{(1-\beta\cos\gamma)^2}. \tag{2.45}$$

As the velocity toward the observer increases, the amount of blue shifted light emitted from the source in the direction of observation increases and the red shifted intensity is reduced.

The second effect is a result of the relativistic electrons involved in scattering with the magnetic field of the Thomson scattering probe laser. The resulting $\vec{v}_i \times \vec{B}$ force, a first order in β correction and neglected in the non-relativistic treatment, is in the same direction as the force of the incident electric field. When the electron is moving towards the detector, the $\vec{v}_i \times \vec{B}$ force adds to the force on the electron due to the electric field of the laser ($q\vec{E}$) and enhances the scattered power. When the electron is moving away from the detector, the $\vec{v}_i \times \vec{B}$ force is in the opposite direction and the scattered power is reduced. The change in scattered power can be estimated by looking at the change in the force on the electron. The scattered power is proportional to,

$$P_s \propto |E_0|^2 \left(1 \mp \left|\frac{\vec{v}}{c}\right| \cos\Phi\right)^2 \tag{2.46}$$

where Φ is the angle between the incident laser direction and the direction of the wave shown in Fig. 2.4. The minus sign is for the red-shifted resonance and the plus sign for the blue. The ratio in the scattered power due to the $\vec{v}_i \times \vec{B}$ term is then

$$\frac{P_{blue}^{\vec{v}\times\vec{B}}}{P_{red}^{\vec{v}\times\vec{B}}} = \frac{(1+\beta\cos\Phi)^2}{(1-\beta\cos\Phi)^2}. \tag{2.47}$$

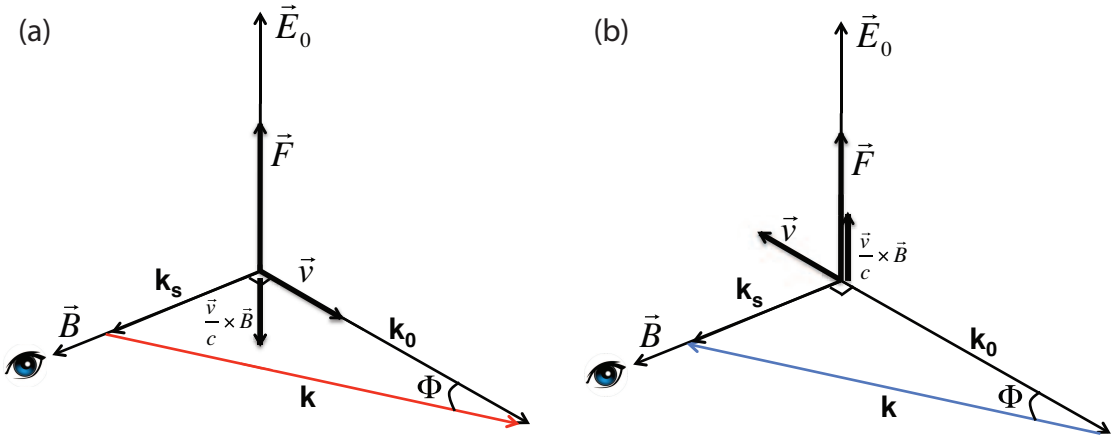

Figure 2.4: The components of the Lorentz force on the electron are shown. $\vec{F}$ denotes the force due to the electric field and $\frac{\vec{v}}{c}\times\vec{B}$ the magnetic field. As the velocity of the particle changes directions the direction of the force due to the magnetic field changes directions as well. For a particle moving away from the observer (a) the two components of the Lorentz force are in opposite directions and the total force is reduced. When the particle is moving toward the observer (b) the components add the total force is increased.

Again, we see an increase in the scattered power into the blue feature and a decrease into the red feature for increasing normalized velocity.

The effects of these corrections on Thomson scattering from electron plasma waves can be estimated by taking the ratio of the peak power in the blue- and red-shifted electron-plasma wave resonances,

$$\frac{P^{blue}}{P^{red}} \approx \underbrace{\frac{P_{\rm nr}^{blue}}{P_{\rm nr}^{red}}}_{A}\underbrace{\frac{(1+\beta\cos\gamma)^2}{(1-\beta\cos\gamma)^2}}_{B}\underbrace{\frac{(1+\beta\cos\Phi)^2}{(1-\beta\cos\Phi)^2}}_{C}, \tag{2.48}$$

where γ is the angle between $\hat{k}$ and $\hat{k}_s$, Φ is the angle between $\hat{k}$ and $\hat{k}_0$, and $P_{\rm nr}^{blue(red)}$ is the peak blue (red) shifted value of Eq. (2.43) shown in Figure 2.2. The asymmetry in term A of Eq. (2.48) is due to Landau damping, the blue-shifted and red-shifted features have different phase velocities resulting in different damping rates. The asymmetry term B is due to relativistic aberration, and term C is due to the initial particle motion interacting with the magnetic field.

It is interesting to note that with a few assumptions it is possible to recover Eq. (2.42) from our simple model described by Eq. (2.48). By looking at the

power scattered into the blue-shifted feature Eq. (6.3) becomes,

$$P \approx P_{\mathrm{nr}}(1+\beta\cos\gamma)^2(1+\beta\cos\Phi)^2, \tag{2.49}$$

and for the conditions where $\gamma = \Phi$, and keeping terms of order β the power scattered becomes,

$$P \approx P_{\mathrm{nr}}(1+4\beta\cos\gamma). \tag{2.50}$$

Noting that $\beta = v/c \approx \omega/kc$ and assuming $k_i \approx k_s$ the k-vector of the scattering wave becomes $k = 2k_0\cos\gamma$, and the scattered power is,

$$P \approx P_{\mathrm{nr}}\left(1+4\frac{\omega}{kc}\cos\gamma\right) \approx P_{\mathrm{nr}}\left(1+4\frac{\omega}{2k_o c\cos\theta}\cos\gamma\right) \approx P_{\mathrm{nr}}\left(1+2\frac{\omega}{\omega_0}\right). \tag{2.51}$$

Which is the result derived in Section 2.1.

2.3 Physical Picture of the Fluctuation Spectrum

In the previous section the first order relativistic effects are investigated from a single particle approach using the phase velocity of the electron-plasma wave as the particle velocity. The goal of this section is to justify that assumption. In the collective regime, the Thomson scattered light is emitted from high frequency electron fluctuations and in the case of scattering from low amplitude thermal fluctuations the majority of scattering is observed from electrons traveling near the phase velocity of the fluctuation. Figure 2.5 shows how particles interact with a traveling potential and in turn sustain that potential. In the case of electron-plasma waves, the potential is created by fluctuations in the electron density and the particles are individual electrons. In the frame of reference moving with the phase velocity of the traveling wave, electrons with a velocity slightly higher than the phase velocity are seen to move to the right and electrons with velocities below the phase velocity move to the left. These moving particles interact with the potential of the wave and gain energy as they move from a region of high potential to low potential and then lose energy as they move back to a high potential region. Electrons traveling near the phase velocity of the wave can become trapped if they

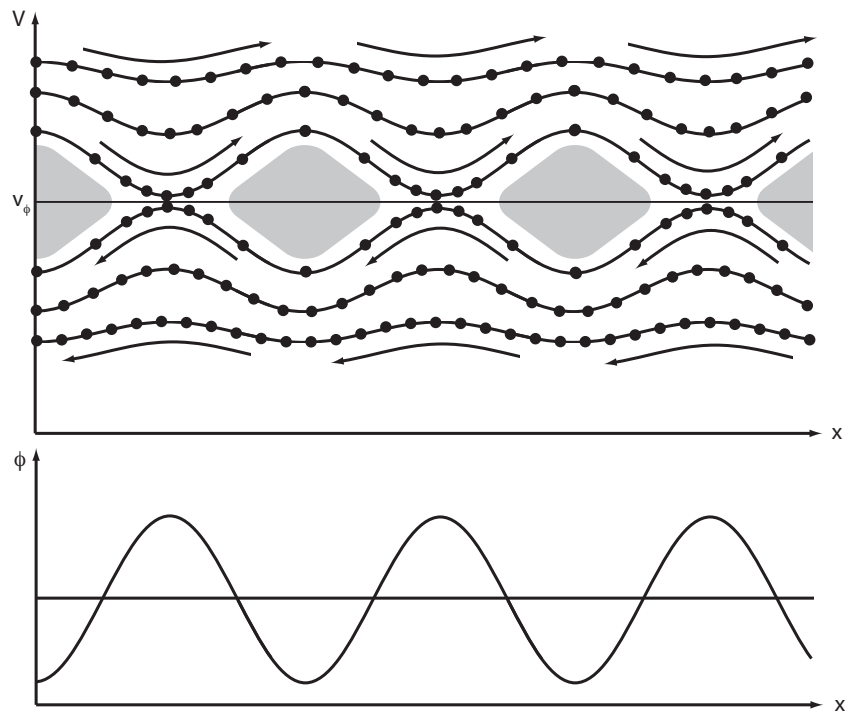

Figure 2.5: Particle motion in an electrostatic potential.

are moving near the low potential areas of the wave and the amplitude of the wave is large enough, these electrons are found in the grey regions of Fig. 2.5.

The electrons traveling near the phase velocity of the wave have the lowest velocity relative to the wave and see a slowly varying potential. The electrons slow down in the high potential regions and accelerate in the low potential regions. This leads to an increased electron density near the high potential regions and a low density elsewhere. Particles traveling much faster or much slower than the phase velocity see a rapidly varying potential and are therefore less affected by the potential (i.e. smaller density perturbations). In effect, the particles moving near the phase velocity have the largest relative variation in velocity. These velocity variations, which tend to cause the electrons to move at a velocity closer to the phase velocity, lead to density perturbations which in turn support the electron-plasma wave.

Then in the presence of a Thomson scattering probe beam light will be scattered by the electrons in the plasma. Light scattered from the electrons that

travel near the phase velocity, which can be visualized as a moving density grating, will add coherently resulting in distinct collective features in the scattered spectrum. The phase velocity of the electron plasma wave is primarily a function of the electron density. This can result in a phase velocity of a few precent the speed of light for high electron densities and low temperatures. In this case, relativistic effects must be taken into account when calculating the Thomson scattering spectrum. This was done in detail in section 2.1 using a kinetic model where relativistic effects are included.

Chapter 3

Experiment

This chapter describes a series of experiments that were performed at the Jupiter Laser Facility on the Janus Laser and at the Laboratory for Laser Energetics on the Omega Laser. Also presented are a description of how a Thomson scattering diagnostic is designed and a description of the diagnostics used for the experiments discussed in this dissertation.

3.1 Experimental Design

Thomson scattering is a powerful experimental technique for a number of reasons, one of which is that it is a localized measurement of plasma parameters. Thomson scattered light is only collected from a selected region of plasma, called the Thomson scattering volume. This volume is defined by the overlap of the Thomson scattering probe beam and the image of the spectrometer and streak camera entrance slits in the plasma. A schematic view of the arrangement used in this work is shown in Fig. 3.1. The size of the Thomson scattering volume is governed by the magnification of the imaging system, the width of the spectrometer and streak camera slits, and the Thomson scattering probe beam diameter. For example if a streak camera and spectrometer use 200 μm entrance slits and the imaging system has a magnification of 2 these slits will have a width of 100 μm when imaged into the plasma. When the slit image overlaps a Thomson scattering probe beam with a 100 μm diameter light will only be collected from the region

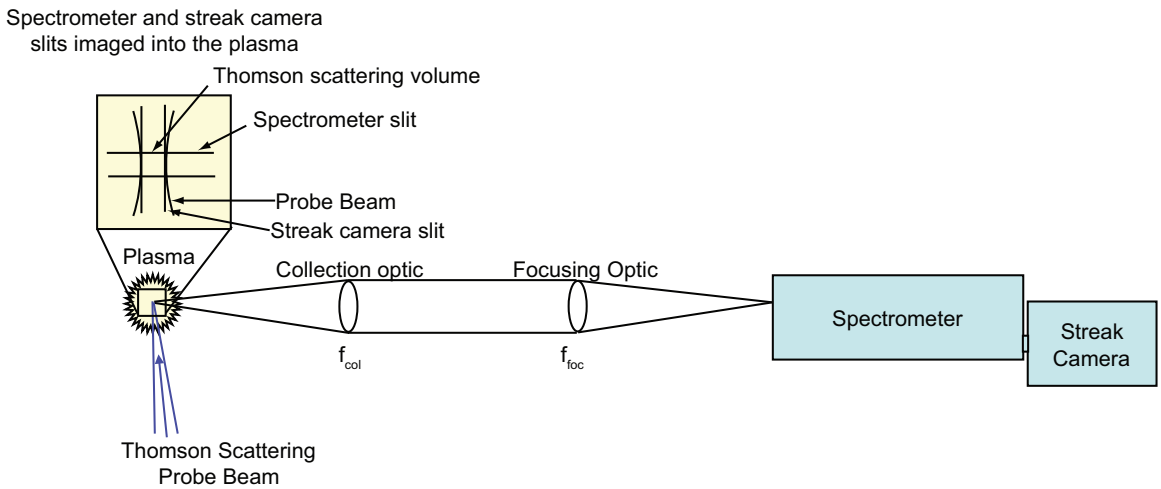

Figure 3.1: A sample experimental setup where a pair of lenses image light scattered from the plasma into a spectrometer coupled to a streak camera. The spectrometer and streak camera slits are imaged into the plasma where their overlap with the Thomson scattering probe beam defines the Thomson scattering volume.

where the slit image overlaps the probe beam. In this example, Thomson scattering volume is then a 100 μm diameter cylinder that is 100 μm long; these dimensions are significantly smaller than the dimensions of the laser produced plasma, which can typically be millimeters or, in the case of NIF hohlraums, 10 or so millimeters long.

By spectrally resolving the light scattered from the Thomson scattering volume a great deal of information can be determined about the plasma conditions within this volume. In the collective regime distinct resonances are observed and it is helpful to estimate the separation between resonances to determine the required spectral resolution. In these experiments, ion acoustic waves (IAWs) and electron plasma waves (EPWs) exist. The density fluctuations associated with these waves or collective electron motion can then be used to determine local plasma conditions such as electron density, electron temperature and so forth. For example, the wavelength separation between the ion-acoustic wave resonances can be estimated using the ion-acoustic wave dispersion relation,

$$\omega_a = \pm k_a \sqrt{\frac{T_e}{M}\left[\frac{Z}{(1+k_a^2\lambda_D^2)} + \frac{3T_i}{T_e}\right]} \tag{3.1}$$

where M is the ion mass, T_e is the electron temperature, T_i is the ion temperature, Z is the charge state and k_a is the wave vector of the ion-acoustic wave. When scattering from low-frequency fluctuations ($k_0 \approx k_s$) the ion-acoustic wave vector can be approximated,

$$k_a \approx 2k_0 \sin\left(\frac{\theta}{2}\right) \tag{3.2}$$

where θ is the scattering angle shown in Fig. 2.1. The wavelength separation between the ion-acoustic wave resonances is then,

$$\frac{\Delta\lambda}{\lambda_0} \approx \frac{4}{c}\sin\left(\frac{\theta}{2}\right)\sqrt{\frac{T_e}{M}\left[\frac{Z}{(1+k_a^2\lambda_D^2)} + \frac{3T_i}{T_e}\right]} \tag{3.3}$$

where c is the speed of light.

A similar expression can be derived for electron-plasma resonances although the condition ($k_0 \approx k_s$) is no longer valid. Using the linear dispersion relation of the electron-plasma wave,

$$\omega^2 = \omega_p^2 + 3v_{th}^2 k^2 \tag{3.4}$$

where $v_{th} = \sqrt{T_e/m_e}$ is the electron thermal velocity, an expression for the expected separation between the scattering resonances can be calculated. Assuming $3v_{th}^2 << c^2$, low densities ($n_e/n_c \lesssim 0.05$), and 90° scattering the expression becomes,

$$\frac{\Delta\lambda}{\lambda_0} \approx 2\left[\frac{n}{n_c} + 6\left(\frac{v_{th}}{c}\right)^2\right]^{1/2}\left(1 + \frac{3}{2}\frac{n}{n_c}\right), \tag{3.5}$$

where n is the electron density and n_c is the critical density for light with wavelength λ_0. A complete derivation of Eq. (3.5) is shown in Appendix A. An example using a fully ionized nitrogen plasma ($T_e = 1$ keV, $T_e/T_i = 3$, $n_e = 10^{20}$ cm^{-3} and $Z = 7$) with a scattering angle of 90° results in an ion-acoustic separation of $\Delta\lambda/\lambda_0 = 2.5 \times 10^{-3}$ and an electron-plasma-wave feature separation of $\Delta\lambda/\lambda_0 = 3.8 \times 10^{-1}$.

Fig. 3.1 shows a typical Thomson scattering system for measuring these features. A lens collects and collimates light scattered from the plasma which is then transported via a series of mirrors to a second lens that focuses the collected light onto the entrance slit of a spectrometer. A high-resolution 1-meter spectrometer is typically used to measure scattering from ion-acoustic waves and a 1/3-meter

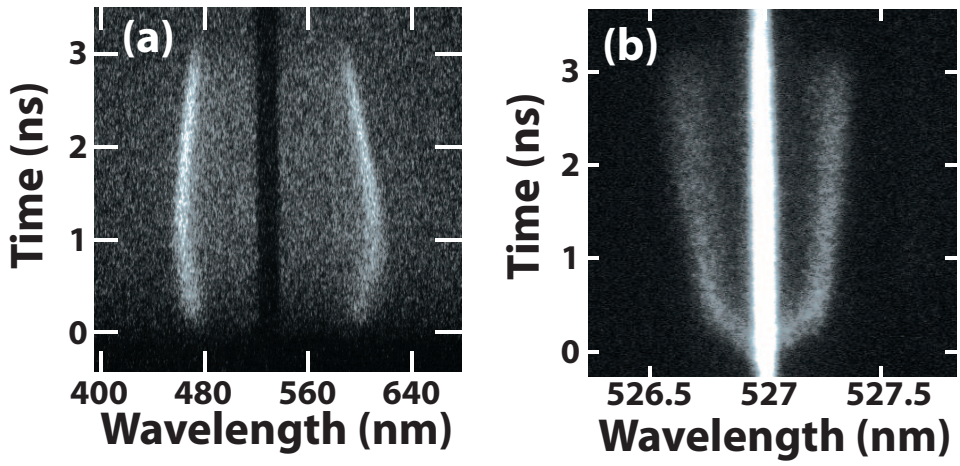

Figure 3.2: A sample of the measured spectra using this experimental setup is shown. Scattering from electron plasma waves (a) and ion-acoustic waves (b) are observed. The residual stray light from the 2ω is filtered from the electron plasma wave measurement (a) and present at 527 nm in the ion-acoustic wave measurement.

spectrometer is used for electron-plasma wave scattering. The output of the spectrometer is coupled to a streak camera for a time resolved measurement, or coupled to a gated CCD camera for a spatially resolved measurement. The spectrometer grating is selected to achieve the desired resolution taking into account the incident Thomson scattering probe wavelength. The temporal resolution is limited by the temporal smear introduced by the spectrometer, given by $\Delta\tau = \eta m \lambda_0 / c$ [42] where η is the number of grooves illuminated, m is the spectral order, and c is the speed of light, as well as the inherent resolution of the streak camera. For a typical ion-acoustic wave system this results in a temporal resolution of $\Delta\tau \approx 200$ ps and for an electron-plasma wave system $\Delta\tau \approx 50$ ps. An example of experimental measurements are shown in Fig. 3.2.

Another important aspect of Thomson scattering is that it can be used as a non-perturbing diagnostic. If the energy deposited by the probe beam in the scattering volume is low compared to the electron thermal energy density it can be assumed that the probe does not affect the plasma conditions. A calculation of the maximum temperature rise for singly charged ions has been presented by

Sheffield [43, Eq. 4.6.6],

$$\frac{\Delta T_e}{T_e} = 1.28 \times 10^2 \frac{n_i \ln\Lambda}{\omega_i^2 A \left(T_e\right)^{5/2}} \int_0^\tau P_i dt \tag{3.6}$$

where $\Lambda = 12 n_e \lambda_{De}^3$, A is the area of the Thomson scattering beam, and τ is the pulse length. The maximum temperature rise occurs when τ is less than the electron-ion equilibration time as well as the thermal conduction time. For ions with an average charge state, Z, the maximum temperature rise becomes,

$$\frac{\Delta T_e}{T_e} = 1.28 \times 10^2 \frac{Z n_e \ln\Lambda}{\omega_i^2 A \left(T_e\right)^{5/2}} \int_0^\tau P_i dt. \tag{3.7}$$

From this equation it is clear the probe will cause large perturbations in the plasma conditions when the electron temperature is low or the density is high.

3.2 Jupiter Laser Facility

The Jupiter Laser Facility is an institutional user facility at Lawrence Livermore National Laboratory designed to provide experimental flexibility and high laser shot rates. The facility consists of 5 laser systems. The Janus Laser system was used for the experiments described in this dissertation. This system employs a Nd:glass laser and a series of rod and disk amplifiers to deliver a maximum of 400 J of 527 nm (2ω) light with a 3 ns pulse length. Pulse shaping capabilities allow pulse lengths between 100 ps and 20 ns with energies ranging from 40 to 450 J.

3.2.1 Laser Configuration

The Janus experiments use a 300 J, 527 nm (2ω), laser focused at target chamber center (TCC) using an $f/6.7$ lens [Fig 3.3(a)]. A continuous phase plate is used to produce a 600-μm super Gaussian focal spot. The standard pulse length is a 3-ns long plateau with a 150 ps rise and fall, a typical measurement of the pulse shape is shown in Fig. 3.4. A second pulse configuration used a 1-ns long square pulse, followed 4-ns later, by a 200-ps full width half maximum Gaussian pulse. When the 1-ns pulse configuration was used, a second low energy (2-3 Joules) 4-ns probe beam was focused orthogonally to both the collection direction and the

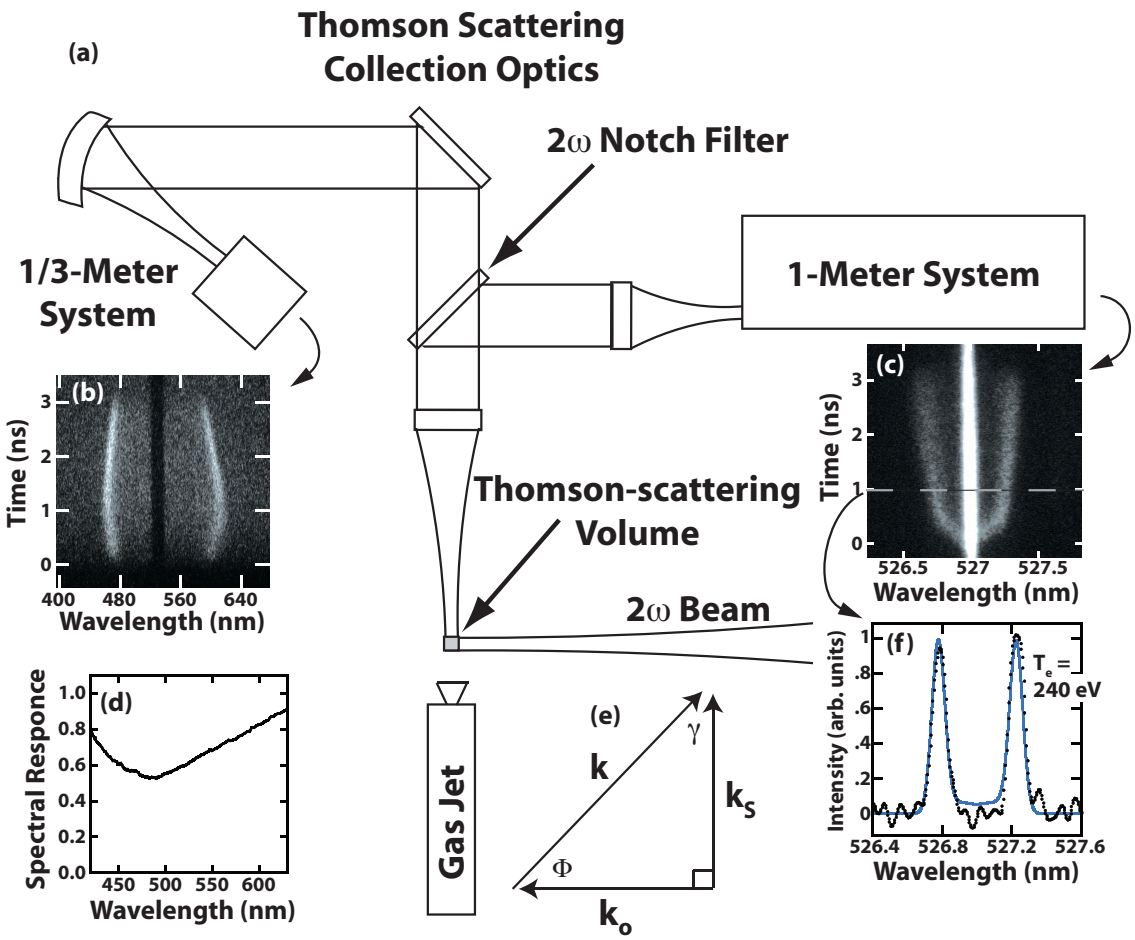

Figure 3.3: (a) Experimental setup. Thomson scattered light is collected 90° relative to the laser beam. Scattering from (b) electron-plasma waves and (c) ion-acoustic waves are displayed. (d) The spectral response of the system used to measure the electron-plasma wave spectra is characterized using a tungsten lamp. (e) The Thomson scattering k-vector diagram shows the orientation of the k-vector that is probed. (f) The ion-acoustic wave spectrum (dots) at 1 ns is fit by the calculated form factor (solid line) with an electron temperature of 240 eV and a density of 1.4×10^{19} cm^{-3} after subtracting the background and stray light.

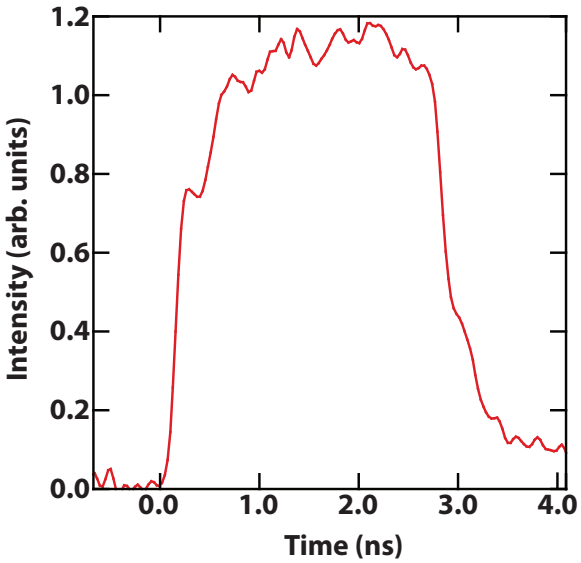

Figure 3.4: A typical 3 ns flat in time Janus pulse.

primary probe beam at target chamber center. This two beam configuration will be referred to as Configuration B throughout this dissertation.

3.2.2 Target

A 1.5-mm diameter gas jet with a nitrogen backing pressure ranging from 10 to 400 psi positioned 1.0 mm below TCC provides neutral gas densities between 1.4×10^{18} cm^{-3} and 1×10^{19} cm^{-3}. The neutral density at target chamber center has been characterized for different backing pressures using an interferometer. An example image from the interferometer is shown in Fig. 3.5 (a). The neutral density scales linearly with backing pressure [Fig. 3.5 (b)].

3.2.3 Thomson Scattering Configuration

An $f/4$ collection lens collimated light scattered 90° relative to the laser beam from the Thomson scattering volume located at TCC. The scattered light is split using a 532 nm notch filter (Iridian Spectral Technologies LR000003-006) and propagated to a pair of spectrometers. The notch filter reflectes light with a wavelength of 532 nm ± 10 nm which is focused onto the entrance slit of a 1-

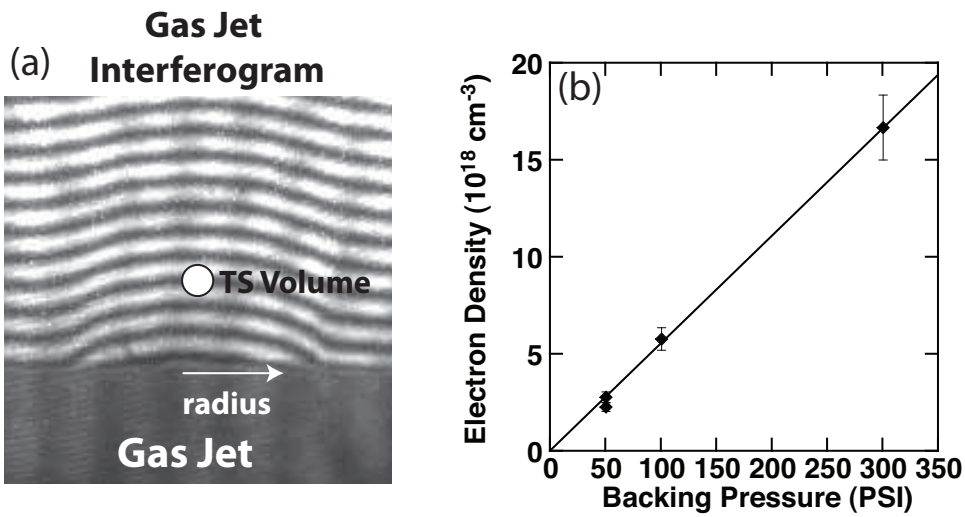

Figure 3.5: (a) An interferometer is used to characterize the neutral density at the Thomson scattering volume as a function of backing pressure. (b) The gas jet density has been measured to scale linearly with backing pressure.

meter spectrometer using an $f/10$ focusing lens. The light transmitted through the notch filter was focused onto the entrance slit of a 1/3-meter spectrometer using an $f/10$ spherical focusing mirror. Both optical systems provide a magnification of 2.5. The 1-meter and 1/3-meter spectrometers are coupled to an S-20 and S-1 Hamamatsu streak camera respectively. Both systems use a spectrometer entrance slit of 200 μm and a streak camera entrance slit of 400 μm. A 2400 grooves/mm grating in the 1-meter system results in a spectral resolution of $\delta\lambda = 0.056$ nm and a temporal resolution of $\Delta\tau = 290$ ps [42]. The 1/3-meter system uses a 150 grooves/mm grating resulting in a spectral resolution of $\delta\lambda = 3.6$ nm and a temporal resolution of 40 ps. The Thomson scattering volume 600 μm x 160 μm x 80 μm is defined by the overlap of the spectrometer and streak camera slit images at TCC with the laser beam.

Two Thomson scattering systems with different streak tubes (S1 and S20) were tested to optimize the quantum efficiency on the high-frequency scattering diagnostic. Fig. 3.6 shows the resulting sensitivities of the systems over the wavelength region of interest. The spectral response of the complete Thomson scattering system was measured by placing the output of a calibrated tungsten lamp at the Thomson scattering volume. By dividing the known tungsten spectrum by the

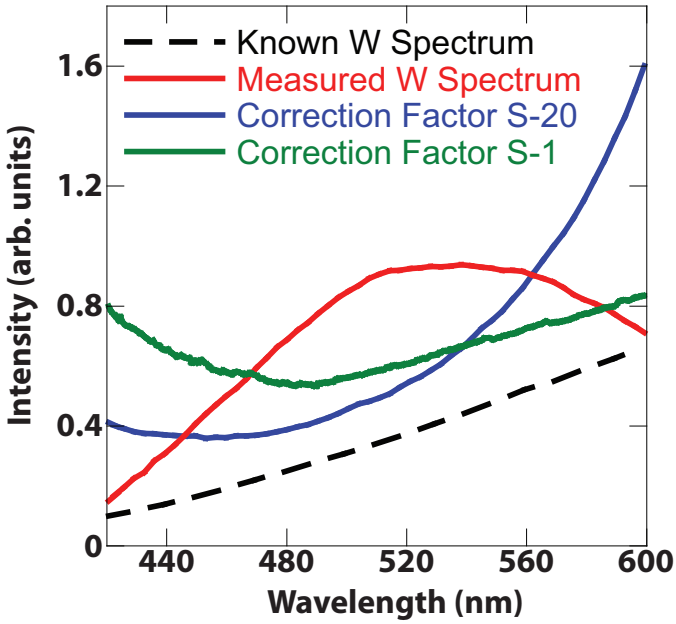

Figure 3.6: The 1/3-meter spectrometer coupled to a streak camera is calibrated for wavelength sensitivity using a tungsten lamp. The measured spectrum for an S-20 streak tube is shown (red curve). The ratio of the known spectrum (black dashed line) to the measured spectrum (red line) results in the correction factor. Two correction factors are shown, one for the S-1 (green line) streak tube and one for the S-20 (blue line) streak tube.

measured spectrum a calibration factor is found which is shown in Fig. 3.6. The uncertainty in the calibration factor was determined to be less than 5% by making a series of measurements throughout the experimental campaign for different ND filtering and camera exposure lengths. This uncertainty is quite low compared to the shot to shot uncertainty which dominated the total uncertainty of the measurements. The S1 streak tube was chosen for measurements where the intensity between the two electron plasma features was being compared. This correction is critical for comparing the intensity of the Thomson-scattering electron feature peaks which can be separated by over 100 nm.

3.3 Laboratory for Laser Energetics

The Laboratory for Laser Energetics [44] is a two laser facility in Rochester, NY consisting of the long pulse facility Omega and the short pulse facility Omega

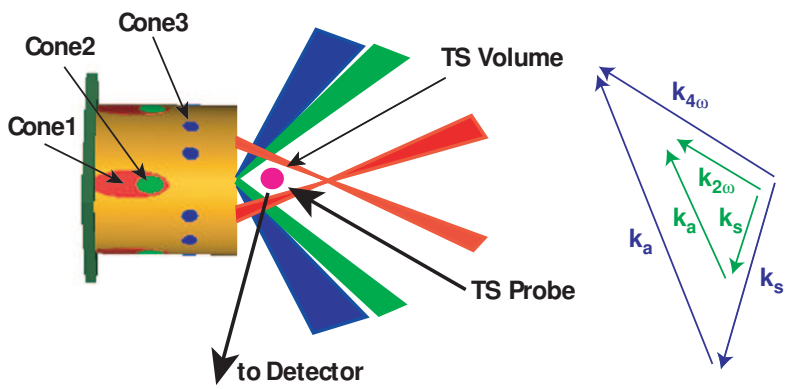

Figure 3.7: The Omega target setup is shown. The Thomson scattering volume is located 200 μm outside the LEH of a Au half-hohlraum heated with 19 beams in 3 distinct cones. A k-vector diagram shows the ion-acoustic fluctuations that are probed.

EP. The Omega facility was used for the experiments described in this dissertation. The 60 main drive beams operated at 3ω (351 nm) and provide a maximum energy of 40 kJ in a 1-ns square pulse. A series of Ten Inch Manipulators (TIMs) are used to deploy diagnostics into the 1.5 meter diameter vacuum chamber. A probe beam [45] has been implemented on the Omega laser for Thomson scattering measurements. The probe can operate at 2ω or 4ω with a maximum energy of 200J in a 1-ns square pulse. An $f/6.7$ focusing optic is used resulting in an aberration limited focal spot size of 40 μm.

3.3.1 Target

A 600 μm diameter Au radiation cavity ("hohlraum") with a length of 600 μm and a single laser entrance hole (LEH) with a diameter of 600 μm was inserted to target chamber center using the Omega target positioning system. The hohlraum is open on only one side, as shown in Fig. 3.7.

A Vanadium foil target 2 mm square with a thickness of 50 μm was also used for Thomson scattering experiments and is shown in Fig. 3.8. The foil target is aligned 200 μm from target chamber center.

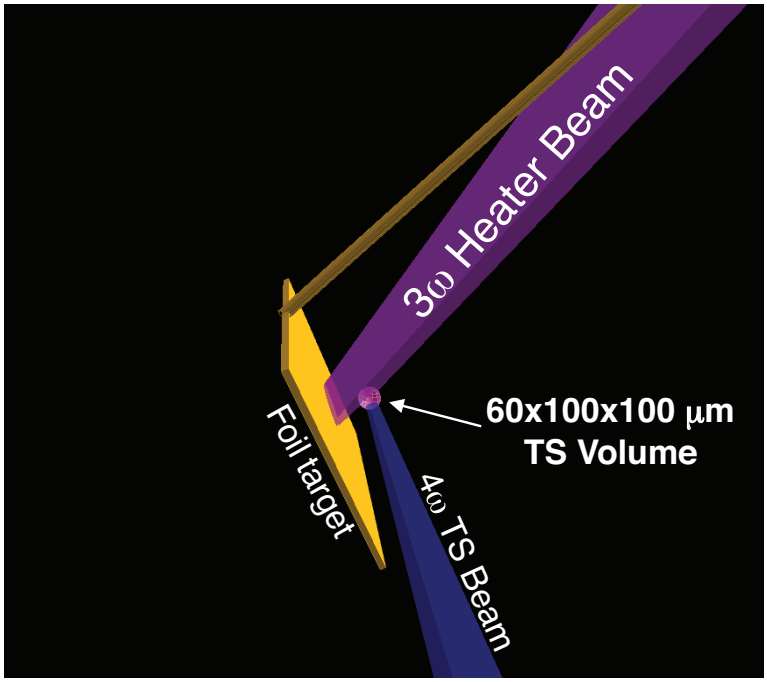

Figure 3.8: The Vanadium target setup is shown. The Thomson scattering volume is located 200 μm off the foil surface heated with a single beam.

3.3.2 Laser Configuration

The hohlraum was heated from one side with 19 Omega laser beams with a 1ns flat-top pulse shape. The Thomson scattering probe beam was a 1ns flat-top pulse and was delayed 500 ps relative to the heater beams. The heater beams entered the hohlraum from one side in 3 distinct cones shown in Fig. 3.7; Cone 1 is focused 400 μm outside the LEH and cones 2 and 3 are focused in the plane of the LEH. There are five beams in cone 1 which enter with an angle relative to the hohlraum axis of 23.2°, 5 beams in cone 2 which enter with an angle of 47.8° and 9 beams in cone 3 which enter with an angle of 58.8°. The beams were smoothed with distributed polarization rotators (DPRs) and delivered a total energy of 10 kJ on target.

The Thomson scattering probe beam enters the target chamber via port P9 ($\theta = 116.57°, \phi = 18.00°$), the poles are defined to be P1 ($\theta = 0.00°, \phi = 0.00°$) and P12 ($\theta = 180.00°, \phi = 0.00°$). The Thomson scattering volume was located along the hohlraum axis 200 μm outside the LEH. Data have been collected using

a 264 nm (4ω) Thomson scattering probe beam and a 527 nm (2ω) Thomson-scattering probe beam. The Thomson scattering volume is (75μm $\times$ 60μm $\times$ 60μm). Collection optics are located in TIM 2 (pre 2009 $\theta = 37.38°, \phi = 162.00°$) resulting in a scattering angle of 101°.

The foil target was heated with a single 3ω beam with a total energy of 490 Joules. There is an angle of 23° between the target normal and the heater beam. The 4ω probe beam was used for this target and it is perpendicular to the foil normal, 200 μm off the foil surface, focused at target chamber center. Both the heater beam and the probe beam are 1 ns flat-top pulses with the 4ω probe beam delayed 1 ns relative to the 3ω heater beam. The collection optics for this experiment where located in TIM 6 ($\theta = 116.57°, \phi = 162.00°$) and have a perpendicular view relative to the foil normal.

3.3.3 Thomson Scattering Configuration

A picture of the Thomson scattering diagnostic is shown in Fig. 3.9. A 1-meter spectrometer with a 3600 lines/mm (2400 lines/mm) grating was used for the 4ω (2ω) probe which resulted in a wavelength resolution of 0.027 nm (0.094 nm). An S-20 streak camera was coupled to the outputs of both spectrometers. The 1-meter spectrometer collected data for 5 ns with a temporal resolution of 210 ps due to the temporal dispersion of the spectrometer [46]. A 1/3-meter spectrometer with a 150 lines/mm grating is used to collect scattering the electron-plasma waves resulting in a spectral resolution of 3.6 nm and a temporal resolution of $\Delta\tau = 40$ ps. A UV grade fused silica Polka Dot beam splitter (S1 in Fig. 3.9) is used for the 4ω beam configuration due to it excellent spectral uniformity over the wavelength range of interest. A photograph of the diagnostic installed in the Omega target bay is shown in Fig. 3.10.

The Thomson scattering system is designed for remote operation due to the hazards present in the target bay. The Omega laser uses an open beam path configuration where all of the beams propagate in air before they are reflected off the final turning mirror into the target chamber. The diagnostic is armed and triggered remotely. The data is saved via a VNC connection to the LLE archiving

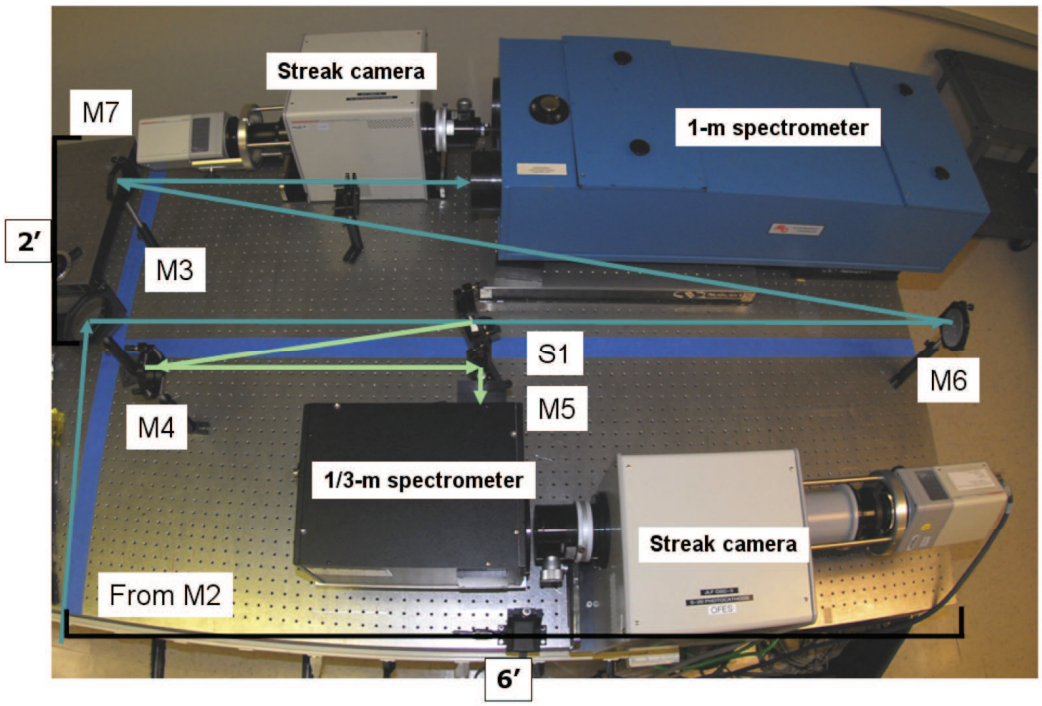

Figure 3.9: The Omega Thomson scattering diagnostic setup is shown. The light scattered form target chamber center enters from the bottom left corner. The light is reflected off mirrors labeled M1 through M7, only mirrors M3 through M7 are shown. M4 and M7 are focusing mirrors that focus the scattered light onto the entrance slit of the spectrometers. S1 is a beam splitter.

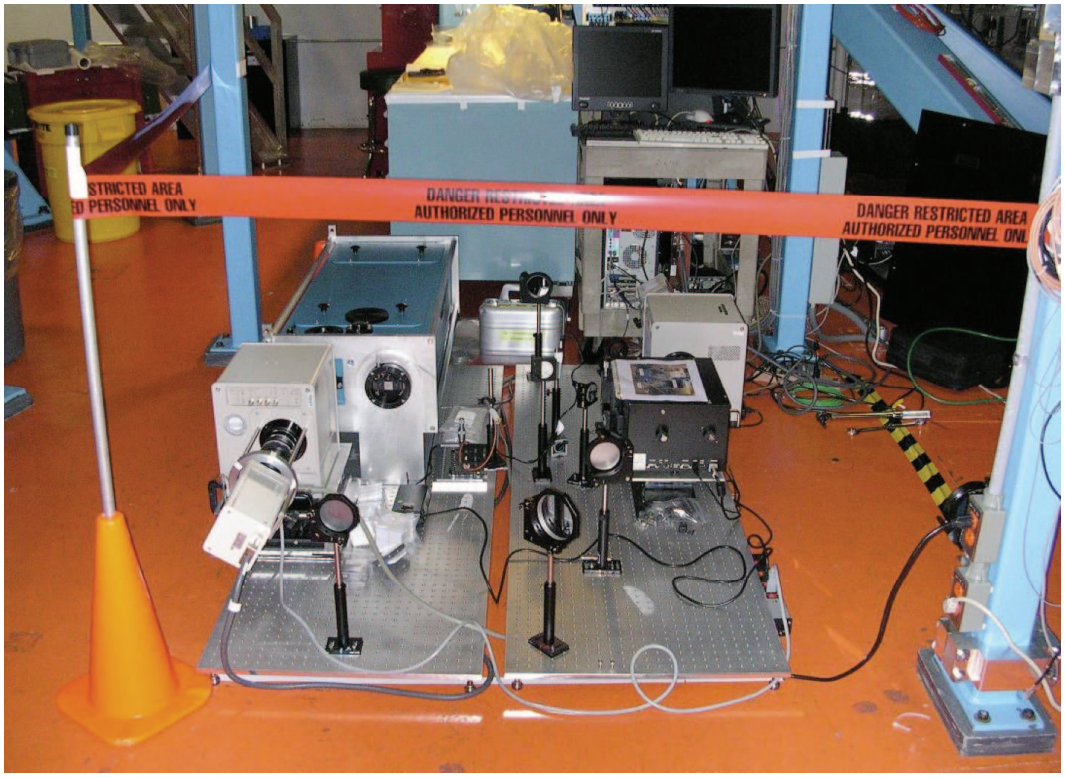

Figure 3.10: The Omega Thomson scattering diagnostic installed in the Omega target bay is shown.

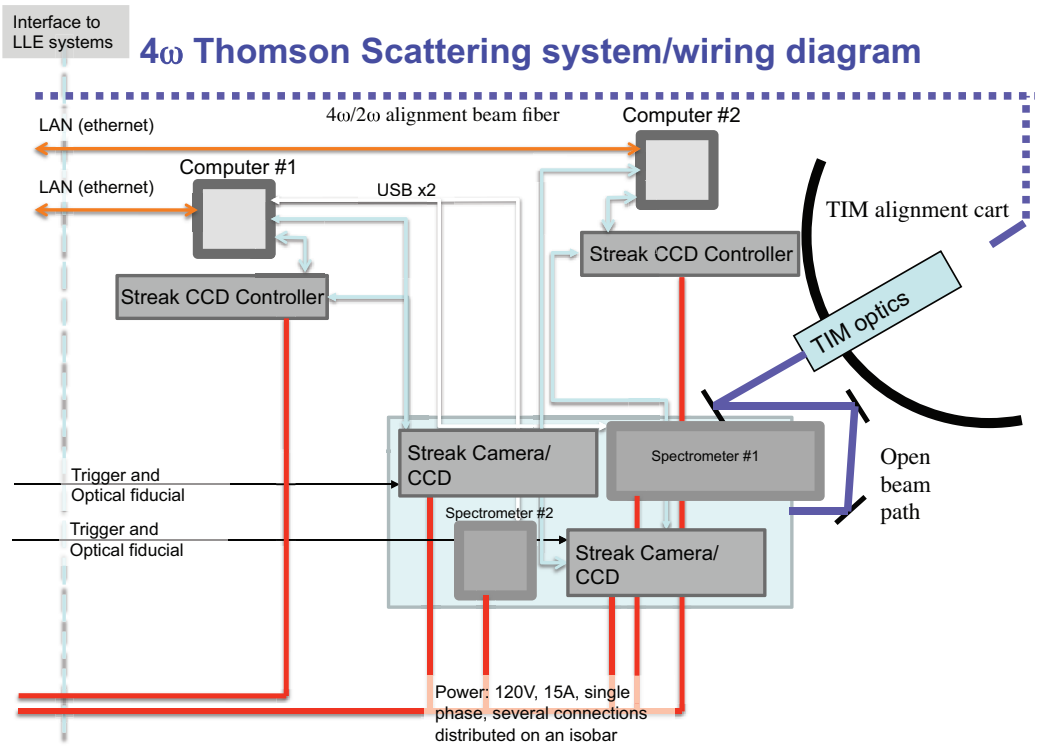

Figure 3.11: The Omega Thomson scattering diagnostic wiring diagram is shown.

system where it can then be accessed from anywhere with a web browser. Fig. 3.11 shows how the Thomson scattering diagnostic interfaces with the Omega facility.

3.3.4 Thomson scattering alignment and focusing

Thomson scattering measurements require precision alignment of the collective system to the Thomson scattering probe beam. The alignment needs to be better than 20 μm. Misalignment has been found to be the most likely cause of low or nonexistent signals. The most reliable alignment method of Thomson scattering alignment uses an alignment laser to backlight a 100 μm sphere located at the Thomson scattering volume. An alignment system was developed to inject laser light into the Omega target chamber using a fiber held by a TIM. An engineering schematic of this system is shown in Fig. 3.12. Initial alignment is completed using a 2ω alignment laser to rough in the system and confirm the beam is centered on the optics in the system. Final alignment is preformed at the wavelength of

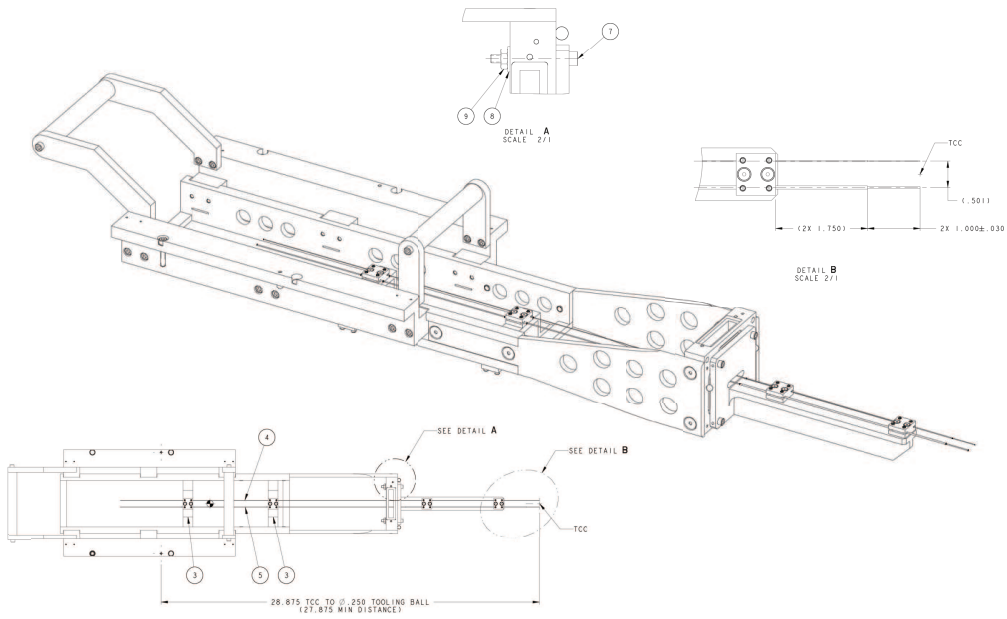

Figure 3.12: The fiber alignment cart is used to precisely position a fiber in the Omega target chamber for Thomson scattering alignment.

the Thomson scattering probe and involves imaging the sphere through the entire system. Once the sphere is visible on the streak camera in focus mode, where the streak camera is operated without applying a ramp voltage so it functions like a CCD camera, the entrance slits of both the streak camera and the spectrometer are closed to the operational widths while keeping the sphere centered between the edges of the slits. This method insures the imaging system is imaging the Thomson scattering volume.

The diagnostic is focused using an alignment target positioned at the Thomson scattering volume. A grid target, with known grid spacing, is imaged through the entire system. An example of this is shown in Fig. 3.13 where the Detector Plane images are taken using the streak camera in focus mode. The target plane images are taken with the Omega target positioning system for comparison. The imaging system produces a 58° counter-cloakwise rotation of the image. The image rotation is important because it effects the slit image in the plasma plane.

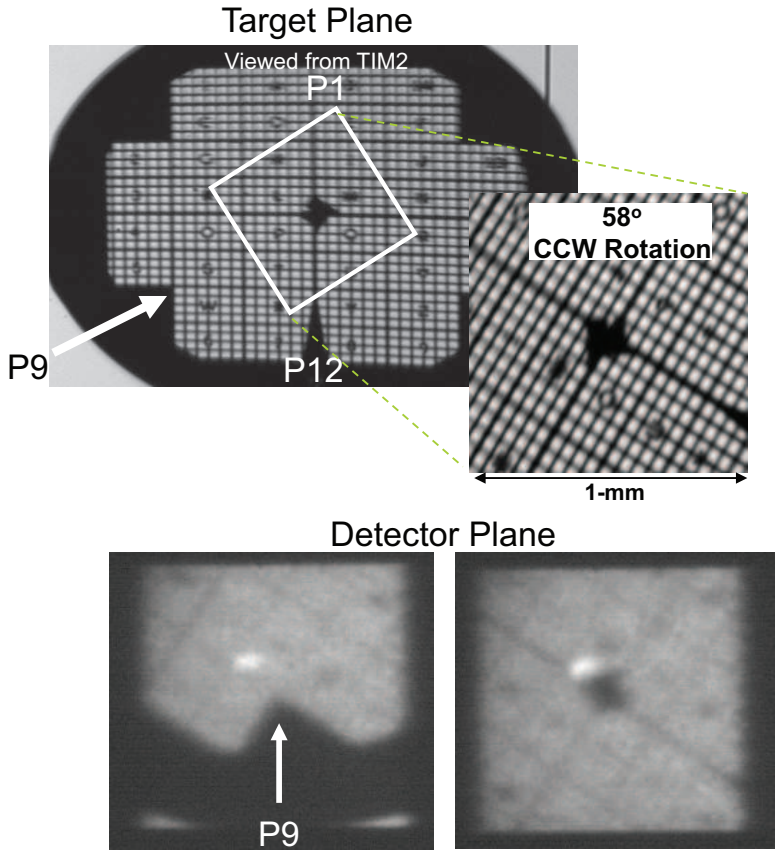

Figure 3.13: A alignment grid target is imaged using the Omega target positioning system (Target Plane) and the Thomson scattering diagnostic in focus mode (Detector Plane). The imaging system produces a 58° counter-clockwise rotation of the image.

Chapter 4

Thomson scattering from electron and ion waves in laser produced plasma

Thomson scattering is a powerful tool for measuring plasma characteristics. Comparing the observed scattering signal to the calculated form factor (Eq. 2.42) allows a measurement of the electron temperature and density, the average charge state, the plasma flow velocity, and the ion temperature. In the collective regime two features are observed, a low-frequency feature associated with the ion-acoustic waves, the ion feature, and a high-frequency feature associated with electron-plasma waves, the electron feature. These features are observed on significantly different wavelength scales, and are typically treated as two independent measurements.

4.1 Electron-plasma waves

In the collective regime ($\alpha > 1$), the wavelength associated with the peak of the electron feature is primarily a function of the density; a larger density results in an increased separation between the two electron-plasma features ($\Delta\lambda_{EPW}$). The electron temperature can be measured from the width of the electron-plasma features due to the change in Landau damping [39]. In the non-collective regime

($\alpha < 1$), the width of the electron feature is governed by the electron temperature and the density can be measured from the scattered intensity.

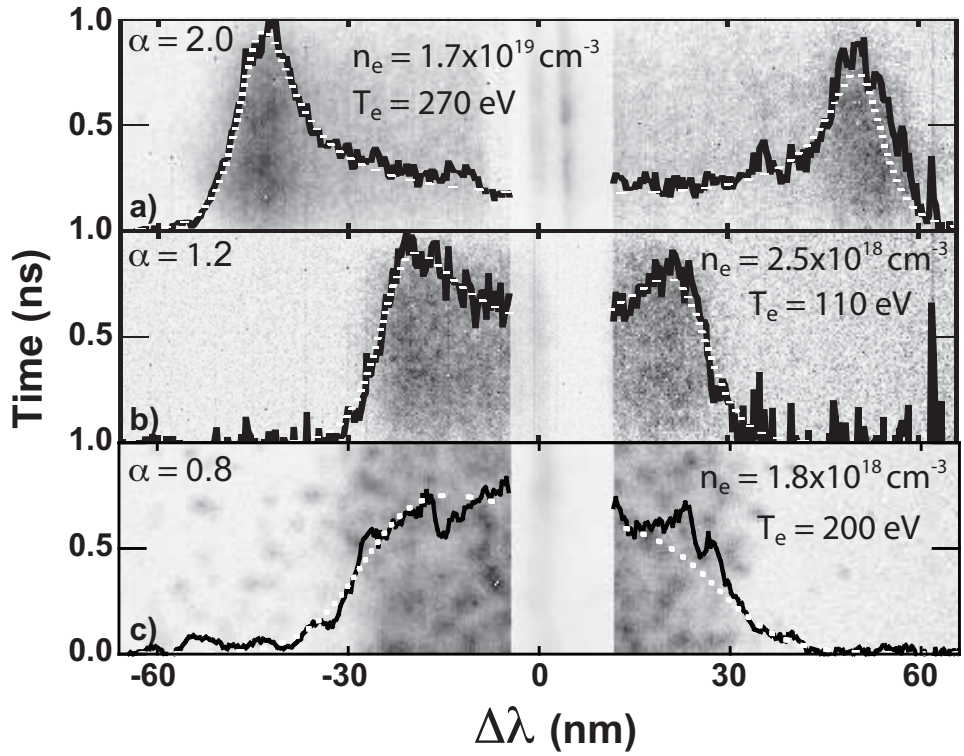

Figure 4.1: Three streak camera records of the Thomson scattering spectrum from the electron feature are shown for different plasma conditions. The scattering parameter decreases as the density decreases:(a) 1.7×10^{19} cm^{-3}, (b) 2.5×10^{18} cm^{-3}, (c) 1.8×10^{18} cm^{-3}. The spectra at 0.5 ns in each streak record (black lines) are shown. The calculated Thomson scattering spectrum (dashed-white line) using the temperature and density is plotted for each spectra. The attenuated region at $\delta\lambda = 0$ is due to the 2ω notch filter.

Fig. 4.1 shows scattering from high-frequency fluctuations where the transition from the collective regime ($\alpha > 1$) to the non-collective regime ($\alpha < 1$) is observed in the Janus gas jet experiment. The scattering parameter was varied by changing the initial gas density which resulted in a range of densities and electron temperatures. Fig. 4.1 (a) shows the scattering spectrum from electron plasma waves in the Janus gas jet experiments. Two distinct peaks are observed. By fitting the scattered spectrum (see dashed line in Fig. 4.1) to the theoretically expected scattering spectrum (Eqn. 2.42), we derive an electron density $n_e = 1.7 \times 10^{19}$ cm^{-3}

and an electron temperature $T_e = 270$ eV, which places this plasma in the collective regime with $\alpha = 2$, consistent with what is expected for the gas density and ionization of these experimental conditions. As the gas jet density is decreased, the plasma density decreases and the spectrum transitions from the collective to the non-collective scattering regime (Fig 4.1 b,c). As α decreases the peaks broaden until a single scattering feature is observed when $\alpha < 1$, Fig. 4.1 (c) is an example of this with $\alpha = 0.8$.

The electron temperature and density are measured by fitting the Thomson scattering form factor (Eq. 2.42) to the measured spectrum. Fig. 4.2 (a) shows the sensitivity of the scattering spectrum to the electron density in the collective regime. Increasing the electron density increases the separation between the shifted peaks due to the increase in the frequency of the electron-plasma waves. An electron density of 1.8×10^{18} cm^{-3} is determined from the best fit to the data. The spectra calculated when increasing and decreasing the density by 10% clearly lie outside of the measurement. Fig. 4.2(b) shows that, in the non-collective regime, the shape of the spectrum is less sensitive to the density. In the non-collective regime, usually the total scattered power is used to measure the electron density when a calibrated collection system is available.

The electron temperature is measured from the shape of the scattering spectrum. Fig. 4.2(c) and (d) show that increasing the electron temperature increases the width of the measured signal. In the collective regime, this is a result of the increased electron Landau damping while in the non-collective regime, this is a result of a broader electron distribution function.

4.2 Ion-acoustic waves

Collective ion-acoustic features can be observed in the scattering spectrum when $\alpha \gtrsim (ZT_e/3.45T_i - 1)^{-1/2}$. The scattered power spectrum (Eq. 2.42) has resonances when $\epsilon = 1 + \chi_e + \chi_i$ is minimized which imposes this condition on α. For Maxwellian distribution functions, the electron and ion susceptibilities can be

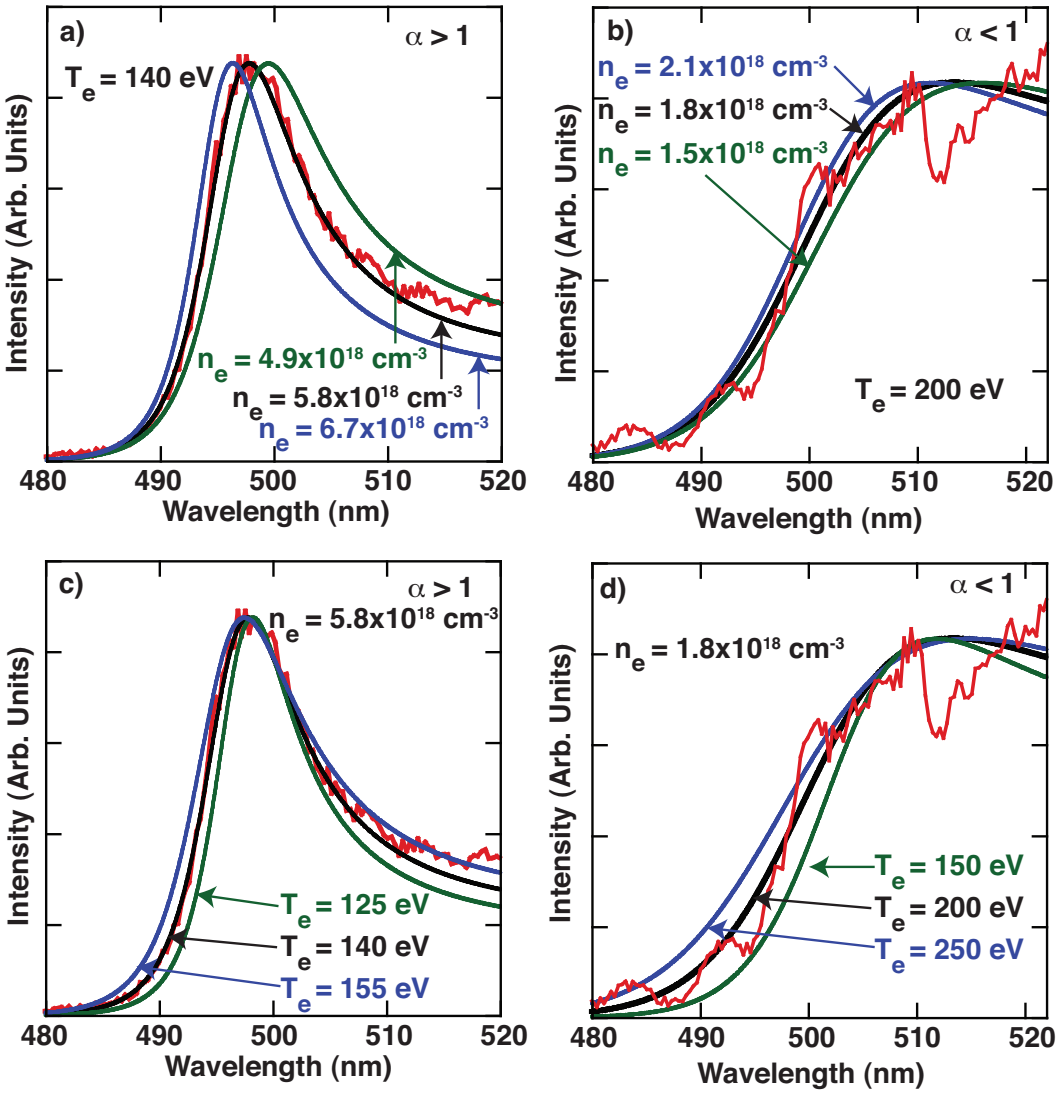

Figure 4.2: By varying the electron temperature and density the error in the measurement can be assessed. The experimental data is shown in red and the best fit for each spectra is shown in black: $T_e = 140$ eV, $n_e = 5.8 \times 10^{18}$ cm^{-3} for (a) and (c), $T_e = 200$ eV, $n_e = 1.8 \times 10^{18}$ cm^{-3} for (b) and (d). In plot (a) n_e is increased by 15% for the blue curve and decreased by 15% for the green curve, $T_e = 140$ eV is held constant. In plot (b) n_e is increased by 15% for the blue curve and decreased by 15% for the green curve, $T_e = 200$ eV is held constant. In plot (c) $n_e = 5.8 \times 10^{18}$ cm^{-3} is held constant and T_e is increased by 10% for the blue curve and decreased by 10% for the green curve. In plot (d) $n_e = 1.8 \times 10^{18}$ cm^{-3} is held constant and T_e is increased by 25% for the blue curve and decreased by 25% for the green curve. The actual errors in the measurement of T_e and n_e is clearly less than the ranges shown here.

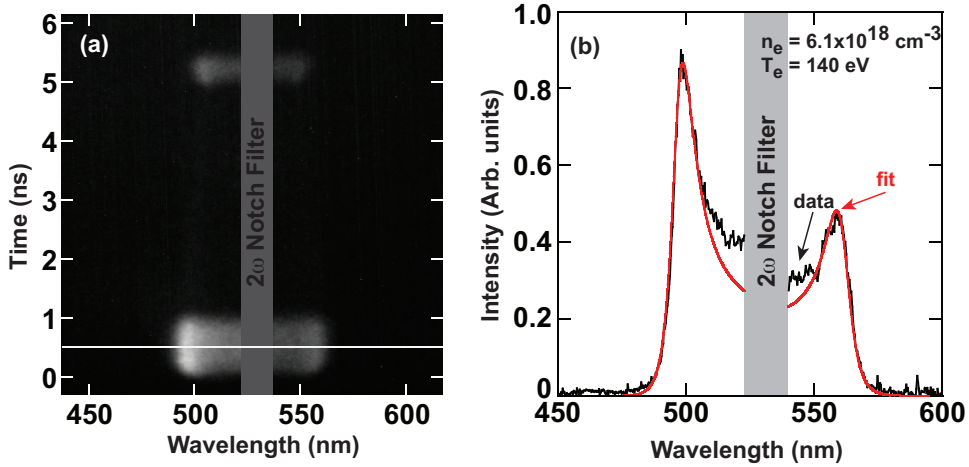

Figure 4.3: (a) Thomson scattering was measured from a Nitrogen gas jet with beam Configuration B. A 2ω notch filter is used to suppress the ion feature. (b) A lineout at 0.5 ns is compared to the Thomson scattering form factor for the listed parameters.

written,

$$\chi_e(\vec{k},\omega) = \alpha^2 \left[\mathrm{Rw}(x_e) + i\mathrm{Iw}(x_e)\right] \tag{4.1}$$

$$\chi_i(\vec{k},\omega) = \alpha^2 \frac{ZT_e}{T_i} \left[\mathrm{Rw}(x_i) + i\mathrm{Iw}(x_i)\right] \tag{4.2}$$

where $\mathrm{Iw}(x)$ and $\mathrm{Rw}(x)$ are the imaginary and real parts of the plasma dispersion function, $x_e = \omega/\sqrt{2}kv_{th}$, $x_i = \omega/\sqrt{2}kv_{ti}$, and v_{ti} is the ion thermal speed. Then the real part of ϵ becomes,

$$\epsilon = 1 + \alpha^2 \mathrm{Rw}(x_e) + \alpha^2 \frac{ZT_e}{T_i} \mathrm{Rw}(x_i). \tag{4.3}$$

For ion-acoustic waves $\mathrm{Rw}(x_e) \approx 1$ and the minimum of $\mathrm{Rw}(x_i) \approx -0.29$. Inserting these values in Eq. (4.3) leads to,

$$\epsilon = 1 + \alpha^2 + \alpha^2 \frac{ZT_e}{T_i}(-0.29) = 0. \tag{4.4}$$

which after solving for α is the condition for collective ion-acoustic features. In the collective regime fitting the Thomson scattering form factor (Eq. 2.42) to the ion-acoustic scattered spectrum makes it possible to measure ZT_e, the plasma flow velocity, the electron density, and the ion temperature, although practical constrains might limit plasma characteristics that can be measured for a given

experimental configuration. For example, temperature gradients in the Thomson scattering volume will make a measurement of the ion temperature from a single species plasma very difficult.

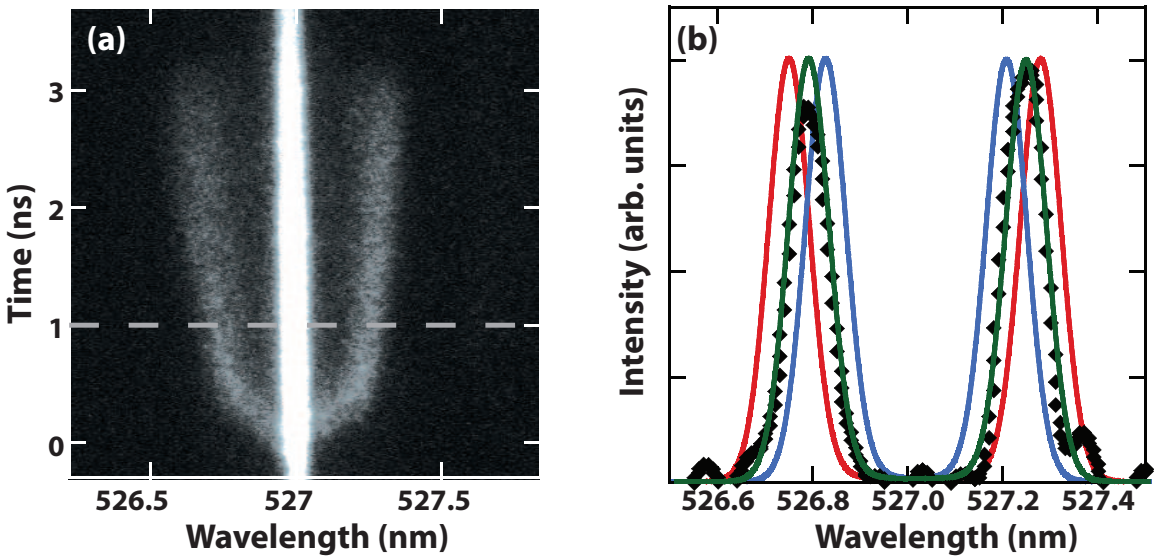

Figure 4.4: A sample ion-acoustic spectrum is shown for the 3 ns pulse configuration. (b) The ion feature is calculated using Eq. (2.42) for 3 different values of ZT_e and compared to the experimental data at 1 ns. The best fit (green line) is calculated with $T_e = 240$ eV and a density of $n_e = 1.25 \times 10^{19}$ cm^{-3}. The temperature is increased by 40% (red line) and decreased by 40% (blue line) to shown the dependence on the electron temperature. The charge average ionization state is assumed to be $Z = 7$.

4.2.1 Electron Temperature

In a high-Z material that is heated with sufficient laser power (as in the case of these experiments), $ZT_e >> 3T_i$ and the ion temperature dependence on the separation between the ion-acoustic features can be ignored. Selecting the scattering geometry such that $k^2\lambda_D^2 << 1$ results in the separation between the two ion-acoustic features being a measure of ZT_e. The Thomson scattering form factor is calculated for 3 values of ZT_e and compared to experimental data in Fig. 4.4. As ZT_e increases the separation between the two peaks in the ion feature increases.

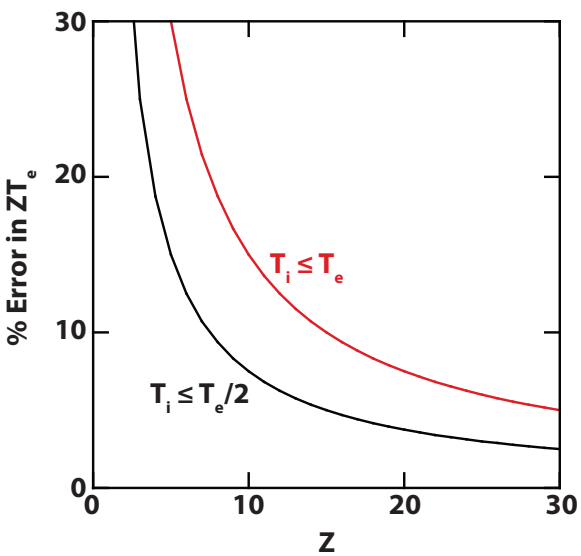

Figure 4.5: The percent error in the measurement of ZT_e is shown for two different assumptions of the ion temperature. As the ionization state increases the error in the measurement of ZT_e decreases.

In a mid- or low-Z material if the ion temperature is unmeasured, but large enough to impact the ion-acoustic dispersion relation, then one must try and estimate the impact of the ion temperature on the electron temperature measurement. In a typical laser produced plasma the dominant heating process is inverse Bremsstrahlung which heats the electrons which in turn heat the ions. For long electron-ion equilibration times, longer than the Thomson scattering probe beam duration, the ion temperature is assumed to be less than $T_e/2$. For short equilibration times, shorter than the Thomson scattering probe beam, the ion temperature is assumed to be less than T_e. This assumption affects the error in the measurement of ZT_e, and is shown in Fig. 4.5.

4.2.2 Plasma Flow Velocity

The ion-acoustic feature can also be used to measure the bulk plasma flow along the direction of $\vec{k}$. The plasma flow causes a pair of doppler shifts which can be observed in the scattered light ($\Delta\lambda_{flow}$),

$$\frac{\Delta\lambda_{flow}}{\lambda_i} = \frac{2}{c}\sin\left(\frac{\theta}{2}\right)\left(\hat{k}\cdot u_f\right) \tag{4.5}$$

where u_f is the plasma flow velocity. The first Doppler shift is due to the electron motion relative to the probe beam. The second doppler shift is due to the plasma motion relative to the detector. This combination of doppler shifts cause a wavelength shift to the entire scattered spectrum which is readily observable when measuring the ion feature.

4.2.3 Electron Density

The intensity of the ion-acoustic features can be used to measure the electron density if the Thomson scattering system is absolutely calibrated. This is typically done using Rayleigh scattering. This technique has seen limited application in high power laser systems due to the significant amount of dedicated target chamber center time required which is often unavailable at large laser facilities. While the total intensity of the ion features is a function of the electron density the relative intensity between the two ion-acoustic resonances is a function of the electron drift velocity. When the damping of the ion-acoustic resonances is dominated by the electron landau damping an electron drift will change the relative damping and result in an asymmetry in the ion-acoustic resonances.

4.2.4 Ion Temperature

In the case of a multi-ion species plasma the ion temperature can be measured using the relative amplitude of the different modes of the ion feature. For a two species plasma there are two modes in the solution to the kinetic dispersion relation due to the different ion masses and the relative damping between the two modes is a function of the ion temperature.

4.3 The Complete Spectrum

When scattering from both electron-plasma waves and ion-acoustic waves the electron and ion temperatures as well as the electron density can be measured when $ZT_e \sim 3T_i$. Looking at Eq. (3.3) it is evident that when ZT_e is on the order of

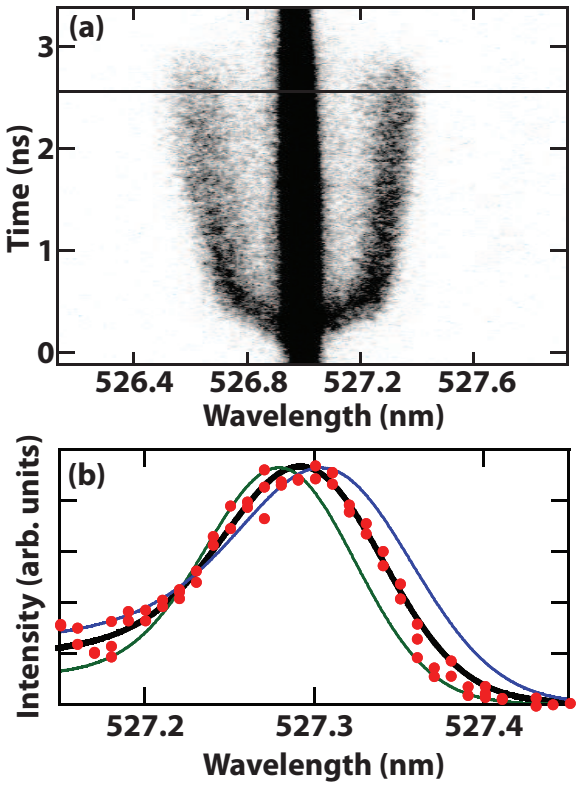

Figure 4.6: (a) A streak camera record of the Thomson scattering from the ion feature is shown. The spectra at 2.5 ns is plotted in (b) where the best fit is shown using the electron temperature and density from the simultaneously measured electron feature ($T_e = 240$ eV, $n_e = 1.3 \times 10^{19}$ cm^{-3}). The ion temperature is then varied to fit the ion feature spectra. The best fit is calculated for $T_i = 180$ eV. The spectra is calculated for T_i plus (blue line) and minus (green line) 60 eV for comparison.

$3T_i$, the separation of the ion-acoustic features is sensitive to the ion temperature. Therefore if T_e is measured using the electron feature T_i can then be measured from the ion feature. For low-Z materials, Z can be estimated with simulations to high accuracy which greatly reduces the uncertainty in the measurement of the ion temperature.

Fig. 4.6 shows collective scattering from ion-acoustic waves in the Janus gas jet experiment. The measured spectrum 2.5 ns after the rise of the heater beam is compared to the calculated spectrum [Fig. 4.6(b)]. Using an electron temperature of $T_e = 240$ eV and a density of $n_e = 1.3 \times 10^{19}$ cm^{-3} measured by the associated high-frequency spectrum, an ion temperature of $T_i = 180$ eV is measured from the

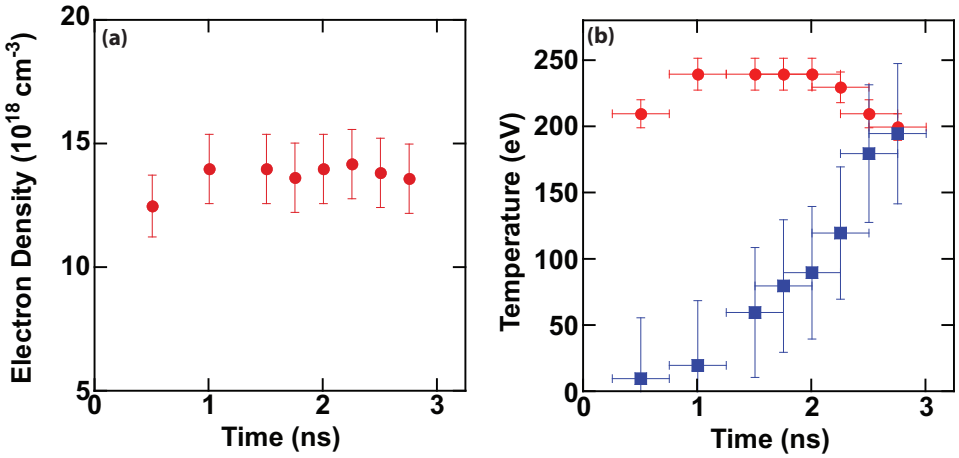

Figure 4.7: The electron density (a) and temperature (b) are shown as red circles measured using electron feature using Configuration B. The ion temperature (b) is shown as blue squares measured using the ion feature.

ion spectrum. The average ionization state of $Z = 7$ is calculated using a Thomas-Fermi ionization model [47]. The width of the ion feature is also a function of the ion temperature, but in laser produced plasmas the width is typically dominated by velocity and temperature gradients within the Thomson scattering volume and, therefore, is an unreliable measurement of the ion temperature. When multiple ion species can be added to the plasma, an ion temperature measurement can be accurately made by resolving the relative scattered power into each ion acoustic resonance [48, 49].

Fig. 4.7 (a) and (b) show the time evolution of the electron density and temperature in the Janus gas jet experiment, in which the plasma is heated by a 3 ns long beam (Configuration B). The electron temperature and density are determined from the high-frequency Thomson scattering spectrum and the average charge state is calculated to be $Z = 7$, the ion temperature is then determined by fitting the ion-acoustic scattering data. The ion temperature is measured to equilibrate with the electron temperature over nearly 3 ns while the density remains constant within the error of the measurement. The ion-electron equilibration time can be calculated using the ion-electron collision frequency [50],

$$\nu^{i|e} = 1.8 \times 10^{-19} \frac{(m_e M)^{1/2} Z^2 n_e \lambda_{ie}}{(MT_e + m_e T_i)^{3/2}} \text{sec}^{-1} \tag{4.6}$$

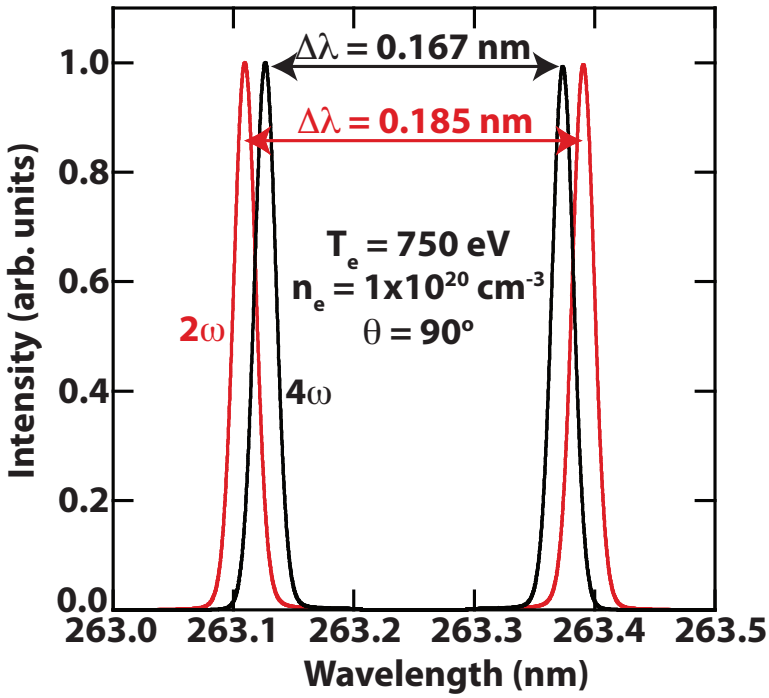

Figure 4.8: The Thomson scattering form factor is calculated for $T_e = 750$ eV, $n_e = 1\times10^{20}$ cm^{-3}, and $\theta = 90°$ for two different probe wavelengths. The spectrum from the 2ω probe is then normalized to the 4ω probe spectrum using the difference in k-vectors.

where M is the ion mass, m_e is the electron mass, and λ_{ie} is the Coulomb logarithm. The equilibration time is then one divided by the collision frequency and for the conditions in Fig. 4.7 is 2.95 ns, which is in excellent agreement with the experimental data. The error in the ion temperature is determined from both the error in the electron temperature (δT_e) and the error in the separation between the ion-acoustic features ($\delta\Delta$). The absolute error in the ion temperature is,

$$\delta T_i = \left(\frac{\Delta\lambda}{\lambda_i}\right)^2 \left(\frac{c^2 M}{24\sin^2(\theta/2)}\right)\frac{\delta\Delta\lambda}{\Delta\lambda} + \frac{ZT_e}{3\left(1+k^2\lambda_D^2\right)}\frac{\delta T_e}{T_e} \tag{4.7}$$

derived from Eq. (3.3). The error in the electron temperature is better than 5% and the error in $\Delta\lambda$ is $\sim 2.5\%$. This results in an uncertainty in T_i of 46 to 53 eV for the measurements shown in Fig. 4.7 (d).

4.3.1 Two Color Thomson Scattering

When scattering from electron-plasma waves is unavailable, it is possible to use multiple simultaneous ion feature measurements to characterize the plasma. This technique has been used to measure the electron temperature and density by scattering from significantly different k-vectors [8]. The phase velocity of ion-acoustic fluctuations is dependent on their frequency therefore measuring two ion-acoustic waves with different phase velocities gives two distinct measurements of the frequency. This is shown in Fig. 4.8 where the Thomson scattering form factor is shown for $T_e = 750$ eV, $n_e = 1{\times}10^{20}$ cm^{-3}, and $\theta = 90°$ for two different probe wavelengths. The form factor for the 2ω probe is normalized to the 4ω wavelength using the difference between the k-vectors. A larger $\Delta\lambda$ is observed for the 2ω wavelength due to the dispersion of ion-acoustic waves. This difference in phase velocities means two measurements can be used with Eq. (3.3) to create a pair of equations with identical plasma parameters (ZT_e, T_i, and λ_D) but different experimental parameters ($\Delta\lambda_{IAW}$, λ_i, θ, and k). Solving this pair of equations simultaneously then allows a measurement of the electron temperature and the electron density, assuming the ion temperature is small and the charge state is known.

Fig. 4.9 shows a visual representation of solving two equations simultaneously where the phase velocity of the scattering wave is changed by using two different probe wavelengths. For a single measurement of $\Delta\lambda$ there are a range of T_e and n_e values that satisfy Eq. (3.3) which are shown as a black line for a measurement made with a 4ω probe beam. A second measurement for $\Delta\lambda$, made with a 2ω probe beam, for the same plasma conditions is shown as the grey line. The electron temperature and density region where these two lines overlap is the region consistent with both measurements. The error in the measurement is calculated from the error in $\Delta\lambda$ which determines the width of each line and then the region where the lines overlap shows the extent of the error.

This two-color Thomson scattering technique was used to measure the electron temperature and density in the Omega hohlraum experiments. Thomson scattering measurements were made 200 μm outside the LEH of a gold hohlraum.

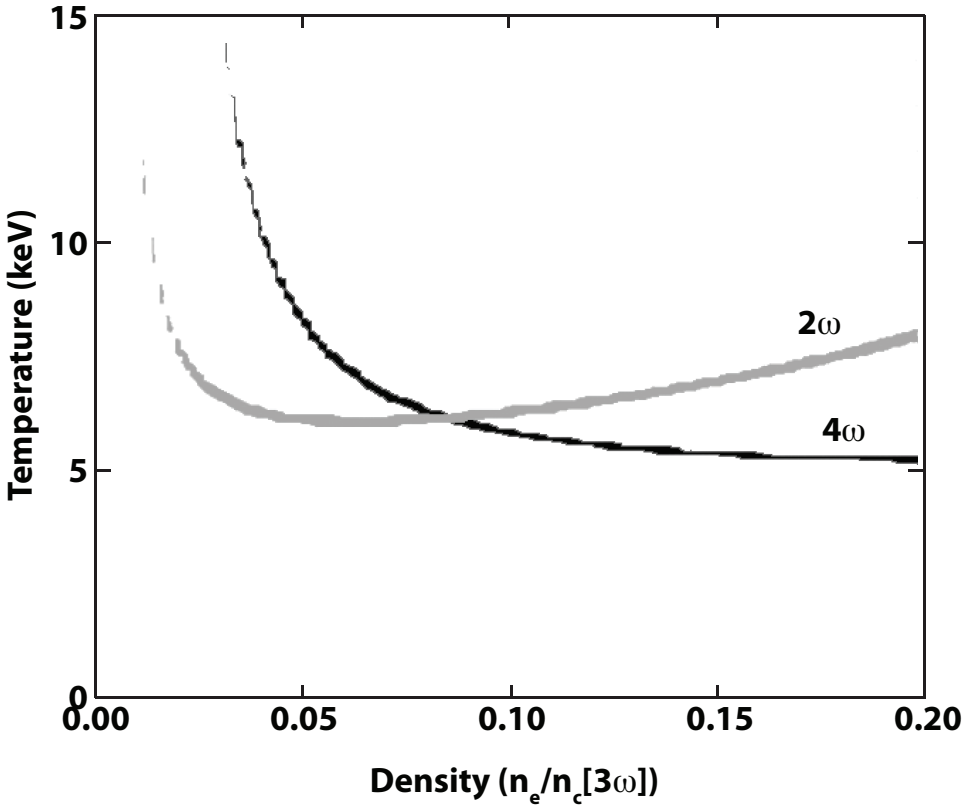

Figure 4.9: The possible values of T_e and n_e for a give pair of $\Delta\lambda$'s are shown. The region where the 2ω values (grey line) overlap the 4ω values (black line) gives the values of T_e and n_e consistent with both $\Delta\lambda$ values.

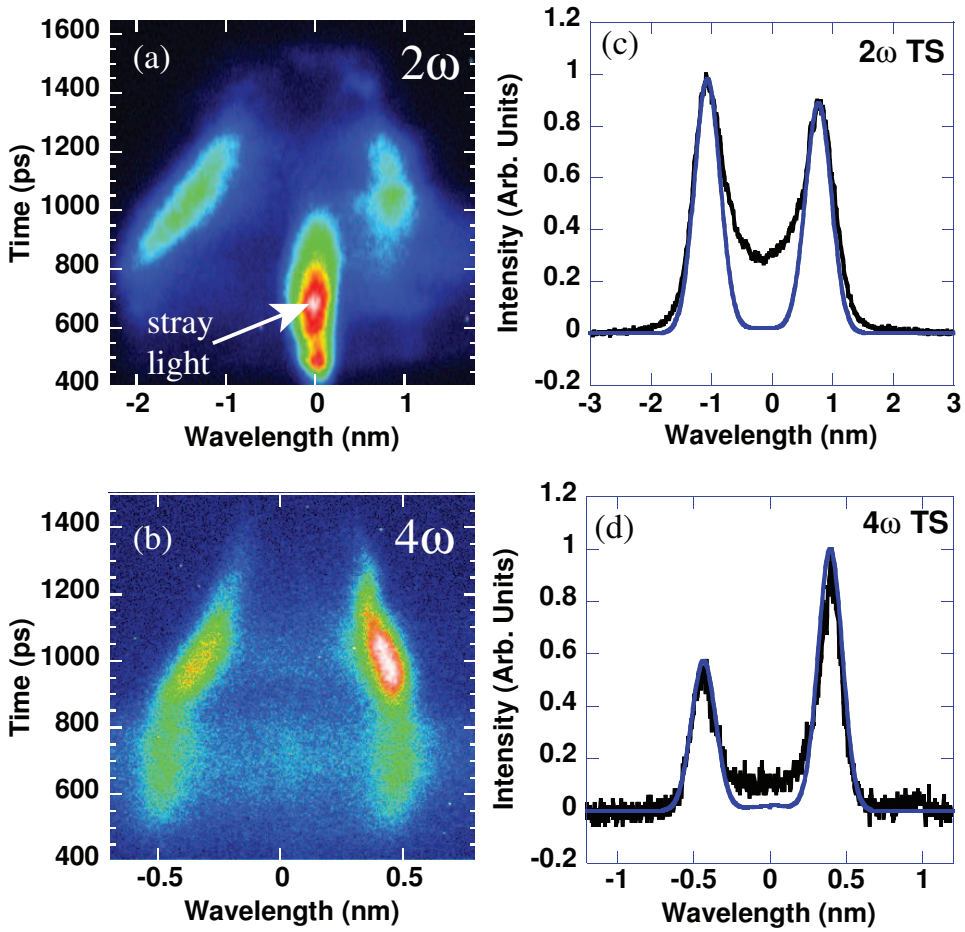

Figure 4.10: Thomson-scattering data from the 2ω probe(a) and the 4ω probe(b). 2ω spectra(c) and the 4ω spectra(d) are shown (black line) with the best fit of the theoretical form factor (blue line). The increased width of the 2ω spectra may be an effect of a slightly larger 2ω spot size increasing the Thomson-scattering volume.

The 4ω measurement is in the $\alpha \sim 1$ regime and is dependent on both ZT_e and n_e. To characterize the plasma a second measurement is required and was performed using a 2ω probe beam. Fig. 4.10 shows the raw data for the 2ω and 4ω probes with measured spectra at 1.1ns. The theoretical form factor is fit to each data set simultaneously providing a local measure of the electron temperature and density. An example fit is shown in Fig. 4.10 (b) and (d) where $T_e = 8.0$ keV and $n_e = 9.9 \times 10^{20}$ cm^{-3}. The charge state ($Z = 40T_e^{0.2}$) is measured using x-ray spectroscopy [51].

Chapter 4, in part, is a reprint of material as it appears in: Ross, J. S, Glenzer, S. H, Palastro, J. P, Pollock, B. B, Price, D, Tynan, G. R, Froula, D. H. "Thomson scattering measurements in the collective and non-collective regimes in laser produced plasma" (Invited) *Rev Sci Instrum* 81, 10D523 (2010). The dissertation author was the primary investigator and author of this paper.

Chapter 5

Thomson Scattering Measurements of Hydrodynamic Evolution

Thomson scattering is an important diagnostic for determining the plasma conditions and studying collective plasma-wave behavior in laser-produced plasmas [52, 53]. These plasmas can be vulnerable to plasma instabilities which are a strong function of the plasma conditions. For example, hohlraum targets for the National Ignition Facility (NIF) [54] require a detailed understanding of the plasma temperature and density in order to mitigate laser-plasma instabilities [55]. In this chapter the hydrodynamic evolution of gas jet and hohlraum targets are investigated.

The hydrodynamic properties of a nitrogen gas jet plasma are measured and are consistent with adiabatic expansion. These results supported a board series of experiments which studied the details of electron heat transport [3, 4] and k-α production [5].

The electron density and temperature are also measured near the LEH of a gold half hohlraum using the two-color Thomson scattering technique presented in Section 4.3.1. Electron temperatures in excess of 10 keV are measured. The effect of these high electron temperatures on laser-plasma interactions and hohlraum radiation temperature are discussed [7].

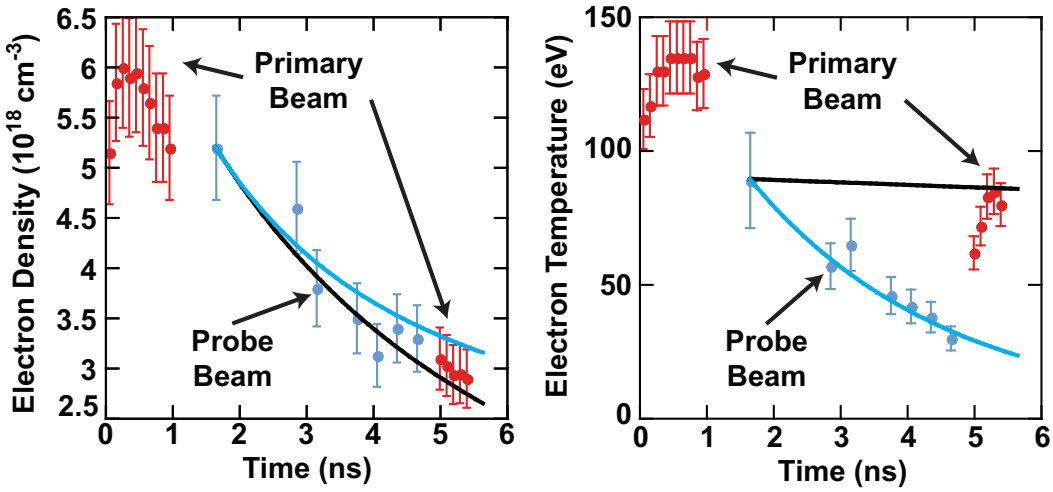

Figure 5.1: The electron temperature and density are measured as a function of time. The red points show data measured from the primary beam and the blue points are measured from the low energy probe beam. The measurements while the primary beam is off are compared to a simple adiabatic expansion model (black line) and the same model including temperature equilibration between the electrons and ions (blue line). The initial conditions for the calculated density are assumed to equal the measured temperature and density at 1.65 ns.

5.1 Gas Jet Hydrodynamics

Thomson scattering is used to measure the plasma parameters for nitrogen gas jet plasmas with two laser beam configurations (see Section 3.2). Fig. 5.1 shows the electron density and temperature measurements when the plasma is heated by a 1 ns long pulse (see Section 3.2.1). The electron temperature and density are measured from electron-plasma wave scattering, described in Section 4.1. The measurements show a rapid increase in the electron temperature and density during the initial 200-300 ps of the laser pulse which ionizes the nitrogen gas. As the temperature increases, the rate of inverse bremsstrahlung laser absorption decreases. At a temperature of 135 eV and a density of $n_e = 6.0 \times 10^{18}$ cm^{-3} the heating due to inverse bremsstrahlung balances the energy loss due to radiation and expansion, making the system nearly isothermal for the remaining 700 ps of the primary beam.

The plasma begins to cool at the termination of the primary beam (1 ns) and there is a decrease in the density which is consistent with adiabatic expansion into

vacuum at the sound speed. By assuming adiabatic expansion, $PV^{\gamma} = constant$, and that the particle number is constant, $nV = constant$, the decrease in density can be calculated by solving the following pair of differential equations,

$$n_e(t)\, k_B T_e(t)\, V^{\gamma}(t) = n_e(0)\, k_B T_e(0)\, V^{\gamma}(0)\,, \tag{5.1}$$

$$n_e(t)\, V(t) = n_e(0)\, V(0)\,, \tag{5.2}$$

where $n_e(0)$ and $T_e(0)$ are the initial electron density and temperature when the primary heater beam is turned off, r_0 is the initial radius of the heater beam, γ is the adiabatic index assumed to be $\gamma = 5/3$, the volume is a cylinder such that $V(t) = \pi\left(r_0 + \int_0^t C_s dt\right)^2 L$, where L is the gas jet diameter and assumed to be constant, and $C_s \approx \sqrt{Zk_B T_e(t)/M}$ is the sound speed. The comparison between the measured parameters and the calculated parameters are shown in Fig. 5.1.

The measured density decreases to $n_e = 3.0 \times 10^{18}$ cm^{-3} and the temperature to 30 eV by the end of the probe beam (5 ns). The temperature decrease greatly exceeds the calculated temperature decease of only 85 eV (Fig. 5.1 black line). To accurately predict the decrease in temperature additional energy loss mechanisms, such as energy transfer to the ions, must be taken into account. This has been done using the thermal equilibration equation [50],

$$\frac{\partial T_e}{\partial t} = \nu^{ei}\left(T_i - T_e\right) \tag{5.3}$$

where T_i is the ion temperature assumed to be zero and ν^{ei} is the electron-ion collision frequency,

$$\nu^{ei} = 1.8 \times 10^{-19} \frac{\left(m_e M\right)^{1/2} Z^2 n_i \lambda_{ei}}{\left(m_e T_i + M T_e\right)^{3/2}} \mathrm{sec}^{-1}, \tag{5.4}$$

where $\lambda_{ei} = 24 - \ln\left(n_e^{1/2} T_e^{-1}\right)$ is the Coulomb Logarithm. The initial temperature and density are used to calculate the collision frequency which is held constant while the electron temperature evolves. The calculated temperature and density including this additional correction is compared to the measurements in Fig. 5.1. The calculated electron temperature shows excellent agreement with the measurements (Fig. 5.1 blue line). The calculated density is now at the range of the

experimental error which is most likely due to the approximation used to calculate the sound speed which neglects the contribution from the ion temperature ($C_s \approx \sqrt{Zk_BT_e(t)/M(1+3T_i/ZT_e)}$). The ion temperature will tend to increase as the electrons cool due to electron-ion collisions which will increase the sound speed and result in a decrease the in the calculated density.

At 5 ns the 200 ps high intensity picket reheats the plasma causing an increase in temperature to 80 eV. The density continues to decrease during the picket to a final measured density of $n_e = 2.8 \times 10^{18}$ cm^{-3}. The density decrease is due primarily to the expansion of the plasma and not recombination as is evident by the lack of a density increase when the plasma is reheated.

The primary beam is off from 1 ns to 5 ns and only a low power beam is used to probe the plasma. Using Eq. (3.7) it can be shown that the possible increase in the electron temperature due to the probe beam, for the electron temperature and density shown in Fig. 5.1 from 1 to 5 ns, is less than 2% for all but the lowest density point where the possible temperature increase is 3%. This is well within the electron temperature error shown in Fig. 5.1.

5.2 High Temperature Hohlraum

High temperature hohlraums have been developed to produce a radiation source with a radiation temperature in excess of 300 eV [56, 7] for material studies at extreme conditions. These targets, described in Section 3.3.1, require efficient laser beam coupling into the hohlraum to achieve maximum radiation temperatures. Laser-plasma interactions have been reported to reduce energy deposition in the hohlraum via refraction, filamentation, and backscatter [57] resulting in a significant reduction in hohlraum radiation temperature. To assess laser-plasma interactions a detailed study of the plasma characteristics was performed.

Fig. 5.2 shows the electron temperature and density measurements as a function of time. The electron temperature ranged from 11.8 keV to 2.9 keV, with the maximum temperature coming 100 ps before the termination of the heater beams, and the electron density ranged from 1.0×10^{21} cm^{-3} to 4.7×10^{20} cm^{-3}.

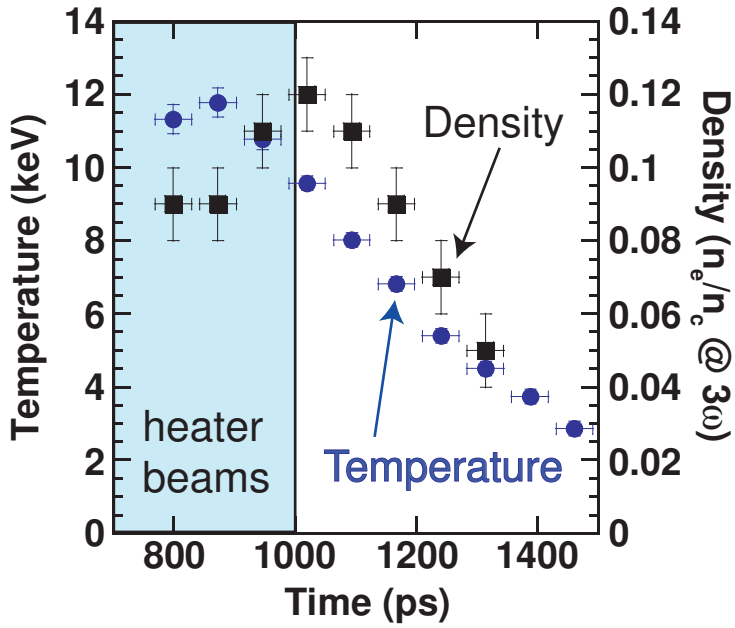

Figure 5.2: Electron temperature and density is measured from 800 ps to 1500 ps relative to the heater beams which turn on at 0 ps and off at 1000 ps. The electron density is normalized by the critical density for 3ω light ($n_c = 9.0 \times 10^{21}$ cm^{-3}), the primary wavelength of the Omega lasers.

After 1.3 ns in the experiment, the scattered spectra is no longer sensitive to density (see Eq. 3.3). The 4ω probe beam does not affect the plasma conditions. The maximum change in the electron temperature due to the probe beam is calculated to be $\Delta T_e/T_e = 0.0015$ (see Eq. 3.7).

The plasma conditions during the heater beams affect filamentation, refraction, backscatter and absorption. Laser absorption due to inverse bremsstrahlung, collisional damping of the laser, has both a temperature and density dependence [40]. Reducing the absorption in the laser entrance hole region is important to maximize coupling of laser energy to the hohlraum wall. The dependence on plasma conditions can been seen in the collisional damping rate,

$$\eta = \frac{\omega_{pe}^2}{\omega^2}\frac{\nu_{ei}}{v_g} \propto \frac{n_e^2}{T_e^{3/2}} \tag{5.5}$$

where ν_{ei} is the electron-ion collision frequency, and v_g is the group velocity of the light wave. Comparing the measured conditions to "ICF" hohlraum plasma conditions ($T_e = 3.5$ keV and $n_e = 5.0 \times 10^{20}$ cm^{-3}) previously used to study

laser-beam propagation [4] shows a decrease in the absorption rate of the high-temperature hohlraum by $\sim 45\%$. Therefore, absorption in the laser entrance hole region does not significantly effect laser propagation or the measured hohlraum radiation temperature.

Another important aspect to consider is beam spray as a result of filamentation. The onset of beam spray has recently been experimentally measured and compared to the filamentation figure of merit [4]. When the filamentation figure of merit is greater than one,

$$\frac{I_p \lambda_0^2}{10^{13}} \left(\frac{n_e}{n_{\mathrm{cr}}}\right) \left(\frac{3}{T_e}\right) \left(\frac{f^{\#}}{8}\right)^2 > 1 \tag{5.6}$$

significant filamentation and beam spray is expected. Here I_p is the power averaged intensity at best focus, λ_0 is the wavelength of the laser beam, n_{cr} is the critical density at 3ω, and $f^{\#}$ is the ratio of the focal length to the beam diameter. At 800 ps the measured $T_e = 11.3$ keV and $n_e = 8.0 \times 10^{20}$ cm^{-3} result in a filamentation threshold of $I_p = 4.8 \times 10^{15}$ W/cm^{-3}. The actual intensity of the heater beams, $I_p = 6.4 \times 10^{15}$ W/cm^{-3} is above this threshold and beam spray is expected. This is consistent with hydrodynamic simulations previously published [56] for a similar target platform which shows beam spray reducing the energy coupled to the hohlraum. This resulted in a radiation temperature that was lower than expected. The Thomson scattering measurements shown in Fig. 5.2 are consistent with this hypothesis.

Chapter 5, in part, is a reprint of material as it appears in: Ross, J. S, Glenzer, S. H, Palastro, J. P, Pollock, B. B, Price, D, Tynan, G. R, Froula, D. H. "Thomson scattering measurements in the collective and non-collective regimes in laser produced plasma" (Invited) *Rev Sci Instrum* 81, 10D523 (2010). The dissertation author was the primary investigator and author of this paper.

Chapter 6

Observation of Relativistic Effects in Collective Thomson Scattering in Laser Produced Plasma

This chapter describes the first observation of a relativistic correction to the thermal collective Thomson scattering spectrum. A factor of 1/2 between the calculated and measured amplitudes of the blue-shifted electron-plasma wave resonance is observed when using the non-relativistic Thomson scattering form factor. This result is attributed to two effects: (1) the relativistic aberration of light which causes a source that emits uniformly in the rest frame to preferentially emit in its direction of motion when moving relativistically, and (2) the interaction of the initial electron motion with the magnetic field of the Thomson scattering probe beam (See Section 2.2). In collective scattering, both of these effects are governed by the electrons moving near the phase velocity of the plasma wave. Therefore, these electrons can be relativistic even at low temperatures. As the phase velocity is reduced, the relativistic correction is reduced, but is always significant for our measurements made for phase velocities, $\beta \equiv \frac{\omega}{kc}$, between $\beta = 0.03$ and $\beta = 0.12$. These effects are ignored in the typical non-relativistic treatment of the Thomson scattering form factor [39, 58, 59].

Including relativistic effects will allow accurate electron temperature and density measurements in laser produced plasmas. This understanding will have a

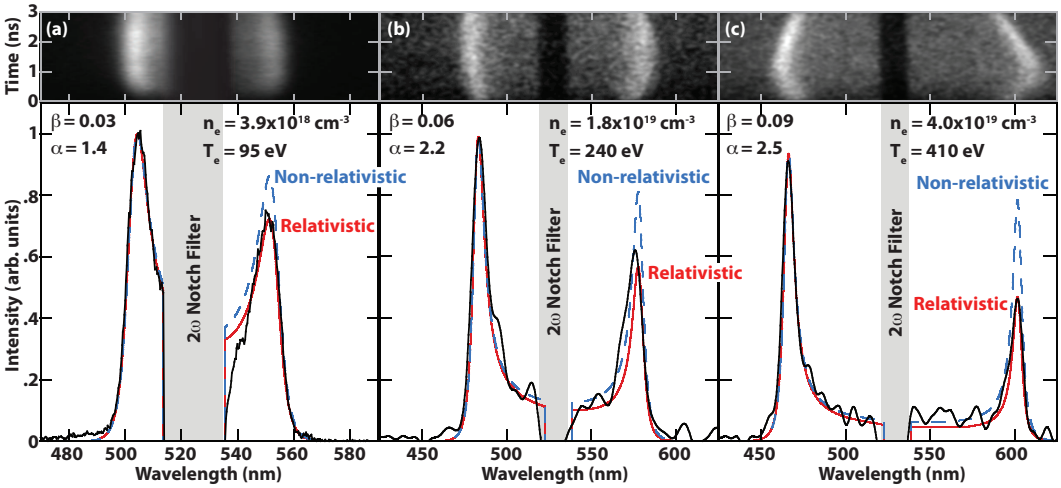

Figure 6.1: Top panels: raw streak data. Bottom panels: experimental data (solid-black line) at 2 ns normalized to the blue-shifted feature and compared to the non-relativistic (blue-dashed line) and relativistic (solid-red line) form factors. As the temperature and density increase, the phase velocity of the electron-plasma wave increases (a) $\beta = 0.03$, (b) $\beta = 0.06$, (c) $\beta = 0.09$ and the difference between the non-relativistic and relativistic form factors becomes more pronounced.

particular impact on measurements made at the NIF where a Thomson scattering diagnostic is currently being developed. An understanding of relativistic effects is crucial for interpreting Thomson scattering measurements for the National Ignition Campaign. The results presented in this chapter are the first experimental observation of relativistic effects in collective Thomson scattering from a laser-produced plasma and have had a direct impact on the design of the Thomson scattering diagnostic development for the National Ignition Facility (see Chapter 7).

6.1 Asymmetric Relativistic Correction

Figure 6.1 shows the temporally resolved collective Thomson scattering from electron-plasma waves for various phase velocities (i.e. densities) measured from the gas jet target described in Section 3.2.2. Both calculated form factors are normalized to the blue-shifted resonance. The primary difference between the non-relativistic [Eq. (6.2)] and first-order relativistic [Eq. (6.1)] form factors is observed in the reduction of the red-shifted electron-plasma wave peak. Including

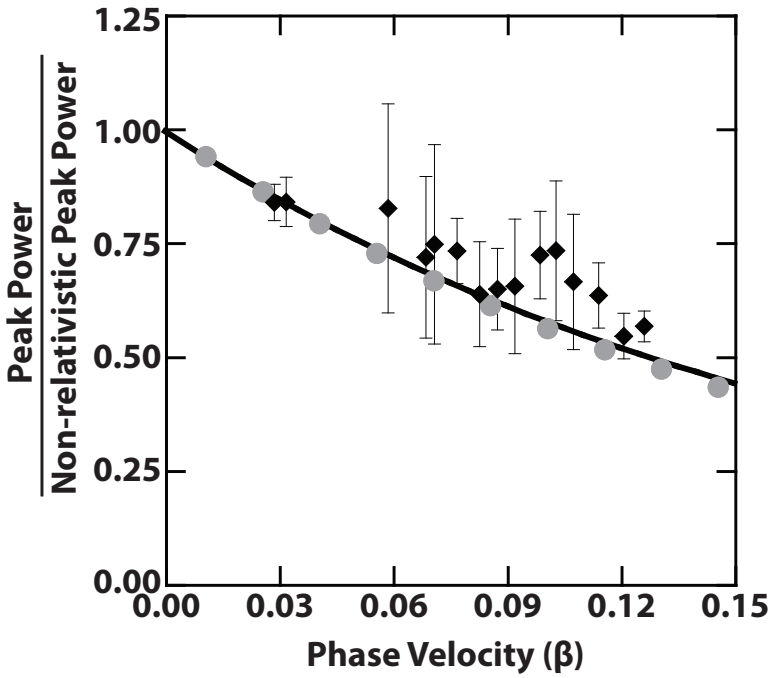

Figure 6.2: The measured peak powers in the red-shifted feature are divided by the calculated peak powers [Eq. (6.2), diamonds] and are plotted as a function of phase velocity. The electron temperature ranged from 85 eV to 720 eV. Data in perfect agreement with the non-relativistic form factor would have a value of unity. The ratio of the relativistic peak power (solid line) and the corrected non-relativistic peak power [Eq. (6.3), grey circles] divided by the non-relativistic peak power are shown.

relativistic effects tends to increase the amplitude of the blue-shifted resonance and decrease the amplitude of the red-shifted resonance, as the form factor is then normalized to the experimental data this change in amplitude becomes a large decrease in the red-shifted amplitude. As the normalized phase velocity of the electron-plasma wave increases from 0.03 to 0.09, the relativistic effects become more pronounced.

Fig. 6.2 shows agreement between the experimental data and the form factor including relativistic corrections calculated in Section 2.1 to be,

$$P_s(R,\omega_s) = \frac{P_i r_e^2 N}{2ak}\left(1+2\frac{\omega}{\omega_i}\right)\left[\left|\frac{1+\chi_i}{\epsilon}\right|^2 f_{e0}(\beta_k) + Z\left|\frac{\chi_e}{\epsilon}\right|^2 f_{i0}(\beta_k)\right], \qquad (6.1)$$

for normalized phase velocities ranging from 0.03 to 0.12. The data are compared

with calculations using the non-relativisitc power spectrum (see Section 2.1),

$$P_{\mathrm{nr}}(k,\omega) = \frac{P_i r_e^2 N}{2ak}\left[\left|\frac{1+\chi_i}{\varepsilon}\right|^2 f_{e0}(\beta_k) + Z\left|\frac{\chi_e}{\varepsilon}\right|^2 f_{i0}(\beta_k)\right], \tag{6.2}$$

where the asymmetry in the peaks is given only by the Landau damping. When using the simple model (derived in Section 2.2) to correct for the relativistic effects,

$$\frac{P^{blue}}{P^{red}} \approx \frac{P_{\mathrm{nr}}^{blue}}{P_{\mathrm{nr}}^{red}}\frac{(1+\beta\cos\gamma)^2}{(1-\beta\cos\gamma)^2}\frac{(1+\beta\cos\Phi)^2}{(1-\beta\cos\Phi)^2}, \tag{6.3}$$

the scattered power agrees with the fully relativistic form factor. The spectra are normalized to the peak power in the blue-shifted feature (see Fig. 6.1) and fit using the form factors. The measured peak scattered power in the red-shifted feature divided by the peak scattered power calculated using the non-relativistic form factor is plotted in Fig. 6.2. Thomson scattered light is observed for the full 3-ns duration of the laser beam (Fig. 6.1). The measured spectra are obtained by integrating over a 200 ps region. After 1 ns the electron temperature and density are determined at 250 ps intervals by fitting the form factor that includes relativistic corrections to the measured spectrum (Eq. 6.1). For clarity multiple shots are averaged at a particular phase velocity; the error bars represent twice the standard deviation within this average. Small discrepancies for some shots are due to noise.

The normalized phase velocity ($\beta = \omega/kc$) of the electron-plasma wave is calculated from the plasma parameters, the scattering angle, and the incident laser wavelength. Maximizing Eq. (6.1) for β provides the normalized phase velocity of the local maxima corresponding to the electron-plasma wave resonances. All normalized phase velocities reported refer to the normalized phase velocity of the red-shifted electron-plasma wave feature.

Fitting the ion-acoustic spectrum with Eq. (6.1) and (6.2) shows that relativistic corrections are not important for scattering from the ion-acoustic resonances at our conditions. Discrepancies are not expected until the phase velocity of the ion-acoustic wave is greater than one percent of the speed of light which is estimated to be when $T_e \approx 140$ keV assuming $ZT_e >> 3T_i$ and a fully ionized nitrogen plasma.

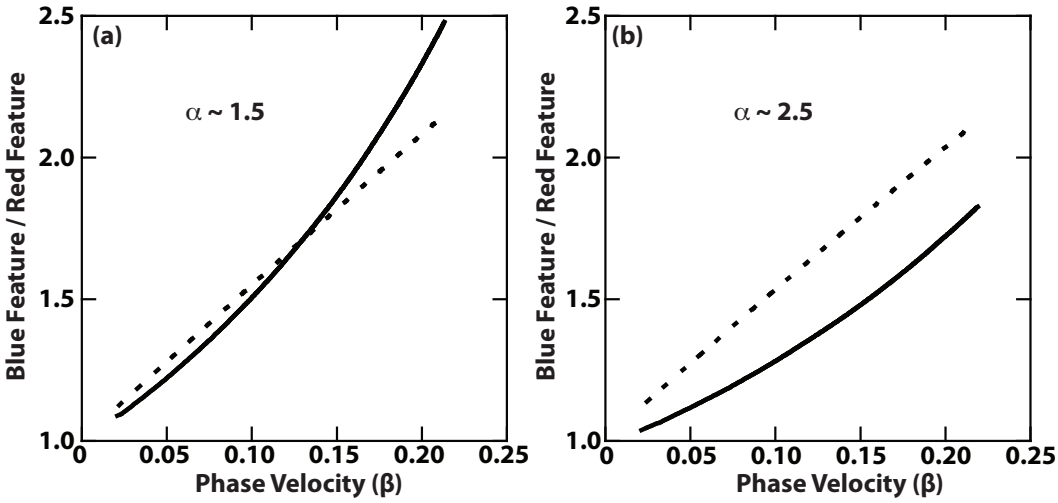

Figure 6.3: The ratio of the blue-shifted feature divided by the red-shifted feature is shown using Eq. (6.1) (black line) and Eq. (6.4) (dotted line) both are plotted as a function of phase velocity. The scattering parameter, α, is held constant at 1.5 (a) and 2.5 (b) for each calculation. Eq. (6.4) shows good agreement with Eq. (6.1) for small values of the scattering parameter and low phase velocity.

An equation has been present by Sheffield [43, Eq. 9.3.9] to estimate the ratio of the blue- to red-shifted resonances,

$$1+4\frac{\left(\omega_{pe}^2+\left(3T_e/m_e\right)k^2\right)^{1/2}}{\omega_i}\cong 1+0.8\times 10^{-2}\left(2\alpha^2+6\right)^{1/2}\sin\frac{\theta}{2}\left[T_e\left(\mathrm{eV}\right)\right]^{1/2}. \quad (6.4)$$

This equation is compared to Eq. (6.1) in Fig. 6.3 for two different scattering parameters. Good agreement is found when $\alpha \leqslant 1.5$ and $\beta < 0.15$. When $\beta > 0.15$ Eq. (6.4) begins to break down, terms of order β^2 have been ignored and are no longer negligible. Also when $\alpha > 1.5$, Landau damping decreases and both resonances are no longer strongly damped. At this point Landau damping, which is ignored in Eq. (6.4), must be taken into account when calculating the ratio of the resonances.

The relativistic effects observed are dependent on the scattering angle and the resulting angles between $\vec{k}_o$, $\vec{k}$, and $\vec{k}_s$ (see Fig. 6.4). When scattering from electron-plasma fluctuations, the direction of $\vec{k}_s$ is fixed but the magnitude is significantly different for the red-shifted and blue-shifted features. This results in different angles Φ and γ for $\vec{k}_s^{red}$ and $\vec{k}_s^{blue}$, which will be labeled Φ_r, Φ_b and γ_r, γ_b respectively. The relationship between the scattering angle, θ, and the result-

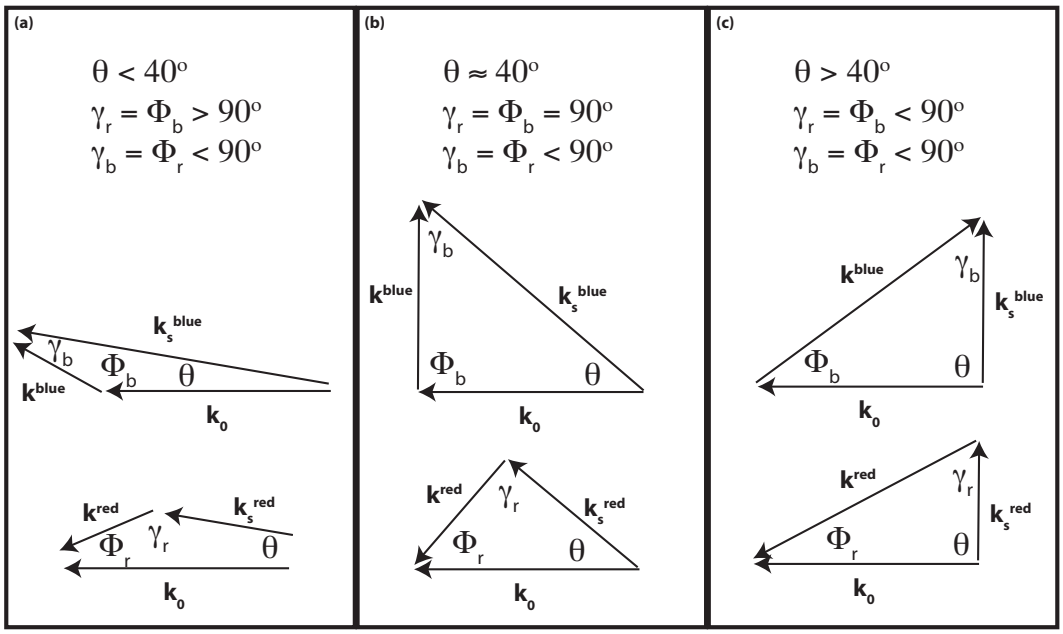

Figure 6.4: The scattering geometry is shown for a series of scattering angles, (a) $\theta < 40°$, (b) $\theta \approx 40°$ and (c) $\theta > 40°$. Both the red-shifted scattered wave vector, $\vec{k}_s^{red}$, and the blue-shifted scattered wave vector, $\vec{k}_s^{red}$ are shown.

ing Φ's and γ's are shown in Fig. 6.4. A series of scattering angles and different k-vectors are shown in Fig. 6.4 for $\theta < 40°$ (a), $\theta \approx 40°$ (b), and $\theta > 40°$ (c). For large scattering angles ($\theta > 40°$) the geometry is similar to that described in Section 2.2. When the scattering angle is approximately 40°, the angle between $\vec{k}^{blue}$ and $\vec{k}_0$ is 90° as is the case with the angle between $\vec{k}^{red}$ and $\vec{k}_s^{red}$. This critical point is due to the geometric constraints, while the magnitude of $\vec{k}_s$ is dependent on the electron temperature and density, hence the approximate angle of 40°. For scattering angles greater than 40° both relativistic aberration and the $\vec{v} \times \vec{B}$ terms enhance the blue-shifted resonance and reduce the red-shifted resonance. When the scattering angle is less than 40° this is no longer the case and the $\vec{v} \times \vec{B}$ term now enhances the red-shifted resonance and reduces the blue-shifted resonance.

In Fig. 6.5 (b) the ratio of the corrections due to relativistic aberration and the Lorenz force ($q\vec{v} \times \vec{B}$ term) are shown for a range of scattering angles. The scattering parameter α is held constant by changing the electron temperature. For large scattering angles both Φ and γ, for both features, approach zero

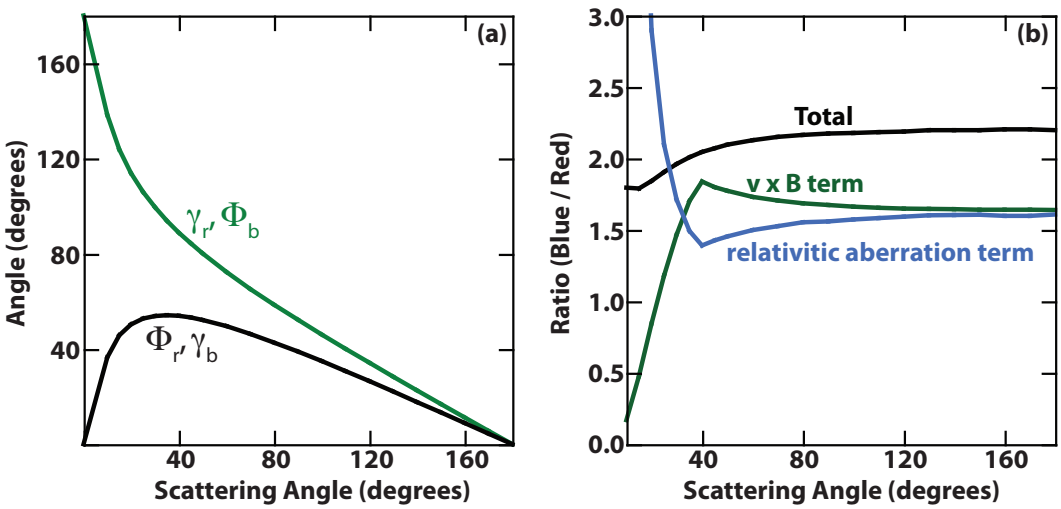

Figure 6.5: (a) The relationship between the scattering angle, the angle between $\vec{k}_0$ and $\vec{k}$, and the angle between $\vec{k}_s$ and $\vec{k}$ is shown for both $\vec{k}_s^{red}$ and $\vec{k}_s^{blue}$. The scattering parameter and the density are held constant. (b) The ratio of the blue-shifted correction divided by the red-shifted correction is shown for the relativistic aberration term and the $\vec{v} \times \vec{B}$ term, plotted as a function of scattering angle. The scattering parameter, α, is held constant at 1.7 by changing the electron temperature, the density is fixed at 1×10^{20} cm^{-3}.

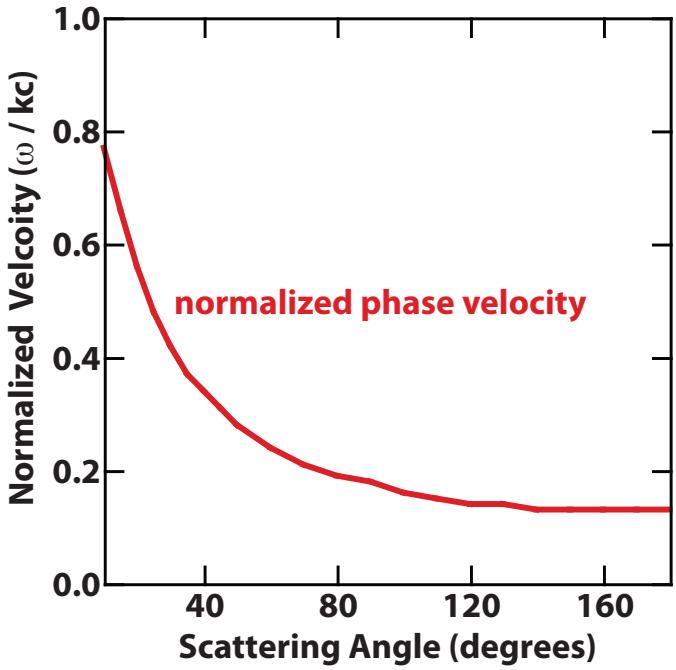

Figure 6.6: As the scattering angle decreases the magnitude of $\vec{k}$ decreases causing an increase in the normalized phase velocity $\beta = \omega/kc$.

and the relativistic effects have a similar magnitude. When the scattering angle approaches 40° the geometry goes through a transition where the angles Φ_b and γ_r pass 90°. This transition is clearly seen in the $\vec{v} \times \vec{B}$ and relativistic aberration terms shown in Fig. 6.5 (b). After this point the $\vec{v} \times \vec{B}$ term decreases for both the red-shifted and blue-shifted resonances. This correction is balanced by the relativistic aberration term which increases rapidly for small scattering angles due to the rapidly increasing phase velocity, the normalized phase velocity is shown in Fig. 6.6. Understanding the effects of scattering angle on the Thomson scattering spectrum is important for the design of future Thomson scattering diagnostics.

Chapter 6, in part, is a reprint of material as it appears in: Ross, J. S, Glenzer, S. H, Palastro, J. P, Pollock, B. B, Price, D, Divol, L, Tynan, G. R, Froula, D. H. "Observation of Relativistic Effects in Collective Thomson Scattering" *Phys Rev Lett* (2010) vol. 104 (10) pp. 105001. The dissertation author was the primary investigator and author of this paper.

Chapter 7

Conclusions

Relativistic effects in collective Thomson scattering from electron-plasma waves, which are attributed to the relativistic "headlight" effect and the electron motion in the direction of the incident light vector interacting with the magnetic field of the Thomson scattering probe, were measured. A relativistic form factor shows excellent agreement with the measured spectra and is required to accurately analyze collective Thomson scattering from electron-plasma waves in laser produced plasmas where T_e and n_e are greater than 100 eV and 1.0×10^{19} cm^{-3} respectively. These results will affect future high-energy density laboratory plasma experiments even at non-relativistic temperatures. In addition, relativistic effects on the growth of collective plasma waves by parametric laser-plasma instabilities must be examined at high phase velocities.

7.1 Future Work

7.1.1 Thomson scattering on the NIF

The next step in measuring relativistic effects in collective Thomson scattering requires higher electron temperatures and densities where relativistic mass correction and modifications to the electron distribution function become significant. These conditions will be common on the NIF, where a Thomson scattering diagnostic is currently being developed. A concept diagram for the proposed Thom-

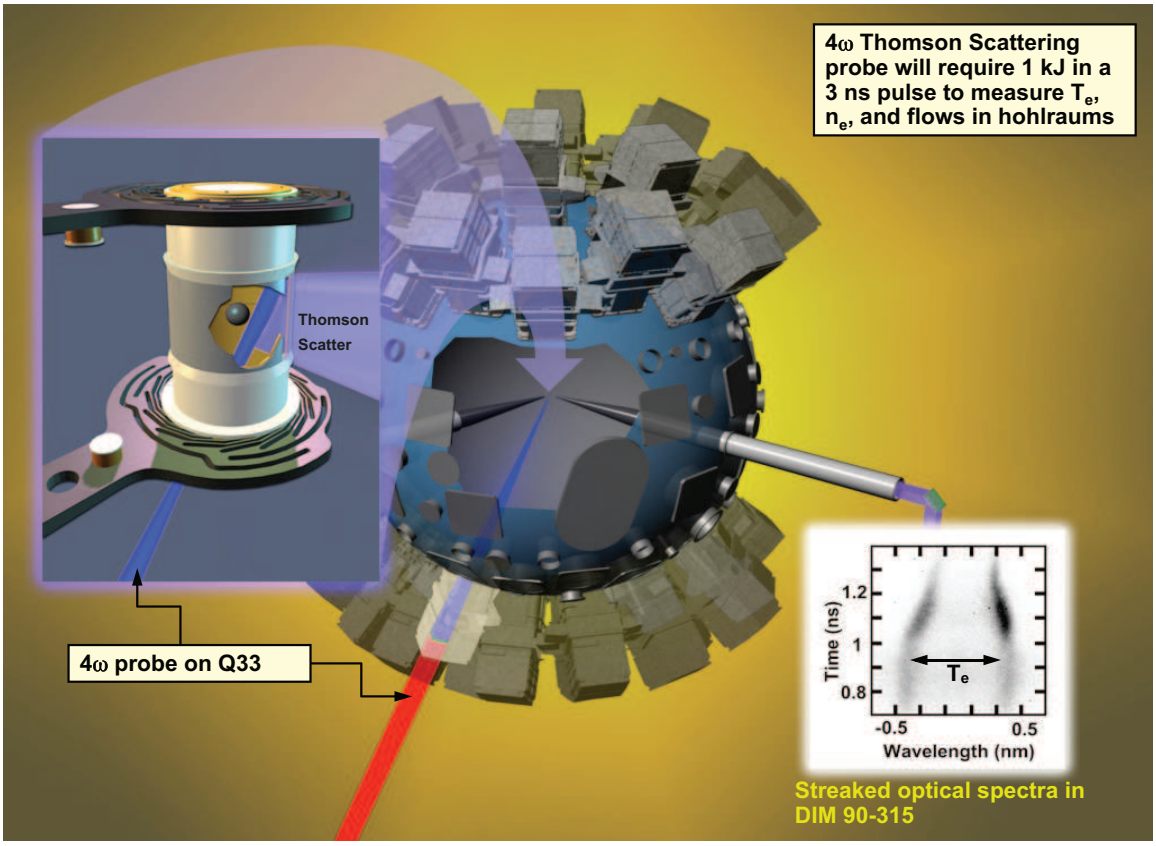

Figure 7.1: A Thomson scattering diagnostic is currently under development on the NIF to measure the plasma conditions inside an ignition hohlraum. A 4ω probe beam is currently being designed to deliver 1 kJ of energy in a 3 ns flat-in-time pulse to target chamber center. The Thomson scattered light will then be collected and propagated to a diagnostic platform. An example Thomson scattered spectrum from Omega is shown.

son scattering system is shown in Fig. 7.1. One of the NIF beams will be frequency quadrupled to generate a Thomson scattering probe beam capable of delivering 1 kJ of energy in a 3 ns pulse. At the conditions expected on the NIF the higher order relativistic effects becomes important and must be taken into account [2]. These effects tend to produce a shift in the frequency of the Thomson scattered light which can be interpreted as a change in density if not properly accounted for.

Fig. 7.2 compares the non-relativistic form factor [Eq. (2.43)], a relativistic form factor including terms of first order in β [Eq. (2.42)], and the fully relativistic form factor for typical NIF conditions. Notice that for collective high-temperature

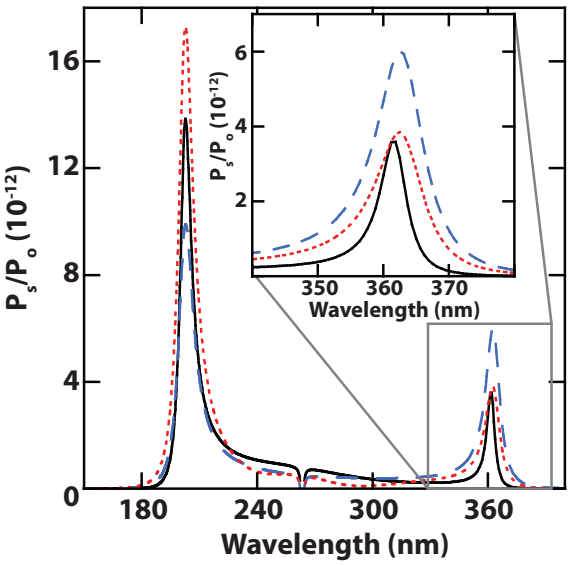

Figure 7.2: The non-relativistic [Eq. (2.43), blue-dashed line], first order relativistic [Eq. (2.42), red-dotted line] and fully relativistic (solid-black line) form factors are compared for typical plasma conditions on the NIF: an electron temperature of 10 keV, electron density of 8.0×10^{20} cm^{-3}, and a scattering angle of 35 degrees using a Thomson scattering probe beam with a wavelength of 263.5 nm. These conditions result in a normalized electron-plasma wave phase velocity of 0.37.

conditions the asymmetry between the different form factors is pronounced and a 2 nm wavelength shift resulting from the relativistic Maxwellian distribution used to evaluate the fully relativistic form factor is observed. Neglecting the relativistic frequency shift produces a 13% error in the measured electron temperature and a 5% error in the measured electron density for the conditions shown in Fig. 7.2.

7.1.2 Electron feature measurements with a 4ω probe

To prepare for Thomson scattering on the NIF an experiment was performed at the Omega laser facility to demonstrate Thomson scattering from electron-plasma waves and ion-acoustic waves using a 4ω probe beam. Ideally, Thomson scattering from electron-plasma waves will be used as a diagnostic for characterizing the electron density in laser produced plasmas but has seen only limited application at large laser facilities due to its challenging nature. When multiple laser beams are used to heat a target, the amount of background and stray light due to laser-plasma instabilities (LPI) can become overwhelming. These issues are most prevalent at the wavelengths of interest for a 2ω Thomson scattering probe beam when heating with 3ω beams (both the NIF and Omega use 3ω lasers for the primary drive beams). To avoid these high background levels and LPI, Thomson scattering probes in the ultraviolet are prefered. The Omega laser currently utilizes a 4ω probe beam and a 4ω beam is currently under development for the NIF. There are three significant advantages to utilizing a 4ω probe beam, the first is the reduced background from plasma emission at shorter wavelengths. The second advantage of a 4ω probe beam is its ability to penetrate more deeply into a plasma due to its higher critical density and the third is reduced refraction compared to a 2ω beam.

As a proof of principle test, initial measurements of Thomson scattering from the electron-plasma fluctuations have been carried out on the Omega laser using a 4ω probe beam. The measured high-frequency spectrum measured from a vanadium plasma is shown in Fig. 7.3. This is the first measurement of the electron feature from a laser produced plasma using a 4ω probe laser. The ion feature was measured simultaneously and by fitting both spectra the electron temperature

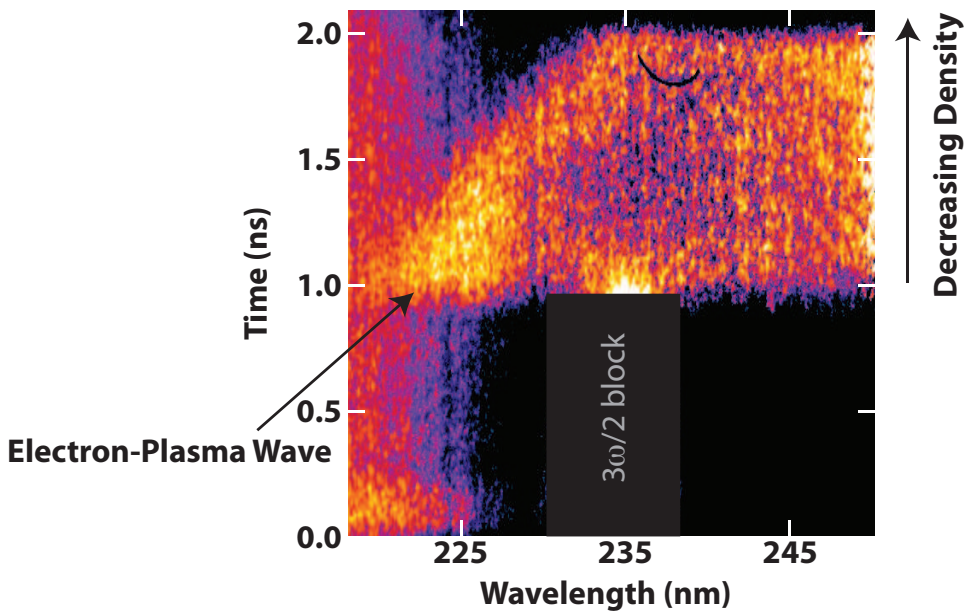

Figure 7.3: High-frequency Thomson scattering data measured from a Vanadium foil target at Omega using a 4ω probe beam. A $3\omega/2$ block is used to suppress light generated by the 3ω heater beam.

and density were measured. Fig. 7.4 shows the measured spectra at 1.5 ns after the start of the heater beam compared to the calculated Thomson scattering form factor using an electron temperature of 1.1 keV and an electron density of 2.1×10^{20} cm^{-3}.

Although Thomson scattering from electron-plasma waves has been demonstrated, there are still a number of challenges that must be addressed. One of the primary concerns is the scattered wavelength. For the Omega experiment the electron feature was observed at 230 nm. On the NIF, the plasma conditions of interest will be more dense and at a higher electron temperatures. This will result in even lower scattered wavelengths ($\sim$ 190 nm) where detector sensitivity and absorption in air become an issue.

Hydrodynamic simulations of the expected electron temperature and density are shown in Fig. 7.5 for a NIF hohlraum at peak laser power [60]. Using the electron temperatures and densities shown in Fig. 7.5 it is possible to calculate the expected wavelength of the blue-shifted Thomson scattering feature. The blue-shifted feature is of course preferred over the red-shifted feature due to its

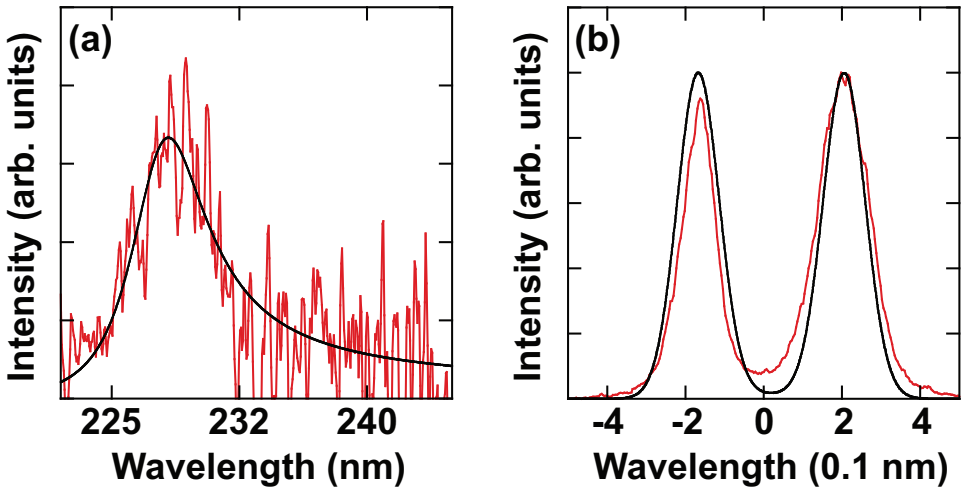

Figure 7.4: (a) The electron feature and (b) ion feature are measured from a Vanadium foil target and compared to the Thomson scattering form factor (Eq. 2.42) with an electron temperature of 1.1 keV and an electron density of 2.1×10^{20} cm^{-3}.

significantly higher intensity when accounting for relativistic effects. The current proposal for the Thomson scattering diagnostic on the NIF will have a scattering angle of $\theta = 147°$, resulting in the scattered wavelengths (calculated using Eq. 2.42) shown in Fig. 7.6. The 195 nm contour is shown. The wavelengths between 150 and 195 nm will be unable to propagate in air due to absorption by oxygen. To allow measurements in this region the NIF Thomson scattering diagnostic will be completely inclosed in a purged gas environment. The detectors and optics will also be specially designed to operate in this wavelength range.

7.2 Final Word

Thomson scattering is a powerful diagnostic for characterizing plasma conditions and studying laser-plasma interactions. With the detailed study of first order relativistic effects and Thomson scattering from electron-plasma waves presented in this dissertation it is clear that Thomson scattering measurements will be beneficial for a large range of plasma physics experiments at facilities like Omega and the NIF. It is expected that Thomson scattering will become a standard di-

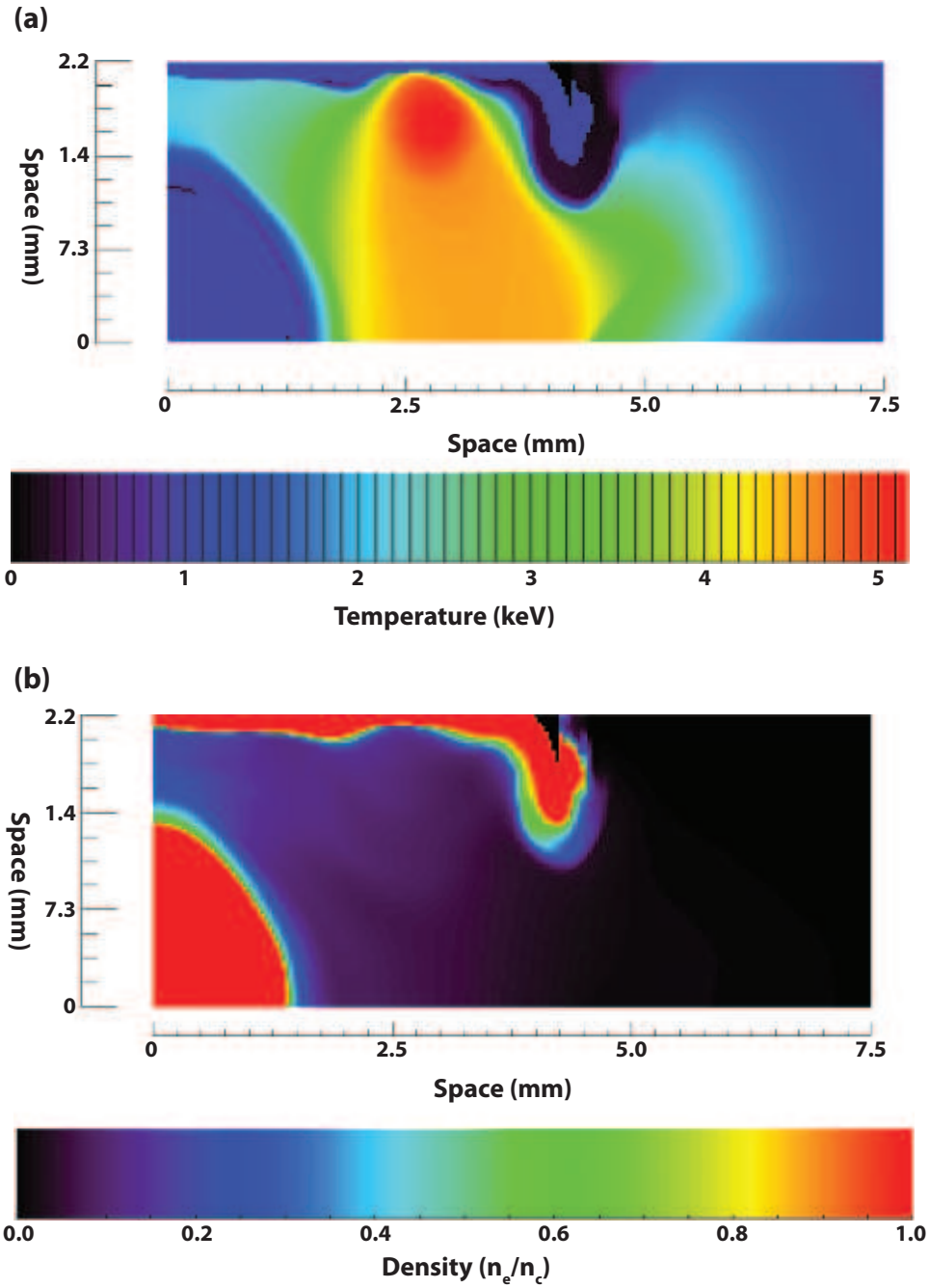

Figure 7.5: (a) The electron temperature and (b) density are shown for a NIF hohlraum hydrodynamic simulation at peak laser power [60]. A quarter of the hohlraum is shown with the fuel capsule centered at (0, 0), the hohlraum wall extends along the top left region and the LEH is centered at (4.5 mm, 0).

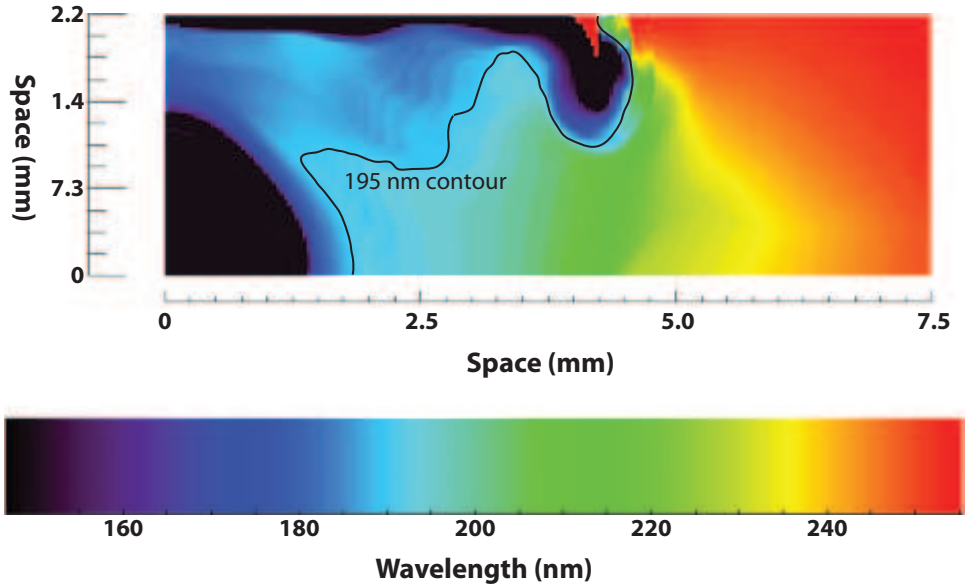

Figure 7.6: The wavelength of the blue-shifted Thomson scattering resonance is calculated using the electron temperatures and densities shown in Fig. 7.5 with a scattering angle of $\theta = 147°$. The 195 nm contour is shown. The region with scattered wavelengths between 150 and 195 nm would be completely absorbed by propagation in air.

agnostic at these facilities, much like non-collective Thomson scattering has at Tokamak facilities.

Appendix A

Delta Lambda EPW

The derivation of the expected wavelength separation for scattering from electron plasma wave resonances using the following equations,

$$\omega^2 = \omega_p^2 + 3v_t^2 k^2 \tag{A.1}$$

$$\omega_s^2 = \omega_p^2 + c^2 k_s^2 \tag{A.2}$$

$$\omega_i^2 = \omega_p^2 + c^2 k_i^2 \tag{A.3}$$

$$\omega_s = \omega + \omega_i \tag{A.4}$$

$$\vec{k}_s = \vec{k} + \vec{k}_i. \tag{A.5}$$

Now assume 1D and substitute Equations A.4 and A.5 into Equation A.2.

$$(\omega + \omega_i)^2 = \omega_p^2 + c^2 (k + k_i)^2 \tag{A.6}$$

$$\omega^2 + 2\omega\omega_i + \omega_i^2 = \omega_p^2 + c^2 k^2 + 2c^2 k k_i \cos\theta + c^2 k_i^2 \tag{A.7}$$

where θ is the angle between k and k_i. Using Equation A.3 the above equation simplifies to,

$$\omega^2 + 2\omega\omega_i = c^2 k^2 + 2c^2 k k_i \cos\theta. \tag{A.8}$$

Equation A.1 can now be used to eliminate ω.

$$\omega_p^2 + 2\left(\omega_p^2 + 3v_{th} k^2\right)^{1/2} \omega_i = \left(c^2 - 3v_{th}^2\right) k^2 + 2c^2 k k_i \cos\theta. \tag{A.9}$$

Assuming $3v_{th}^2 << c^2$.

$$2\left(\omega_p^2 + 3v_{th}k^2\right)^{1/2}\omega_i = c^2k^2 + 2c^2kk_i\cos\theta - \omega_p^2 \tag{A.10}$$

Squaring both sides,

$$4\left(\omega_p^2 + 3v_{th}k^2\right)\omega_i^2 = c^4k^4 + 4c^4k^2k_i^2\cos^2\theta + \omega_p^4 - 2c^2k^2\omega_p^2 - 4c^2kk_i\cos\theta\omega_p^2 + 4c^4k^3k_i\cos\theta. \tag{A.11}$$

Factoring terms and using Equation A.3,

$$\begin{aligned} k^4 + 4k^3k_i\cos\theta + 4k^2k_i^2\cos^2\theta\left(1 - \frac{\omega_p^2}{2c^2k_i^2\cos^2\theta} - \frac{3\omega_i^2v_{th}^2}{c^4k_i^2\cos^2\theta}\right) \\ -4kk_i\cos\theta\frac{\omega_p^2}{c^2} - 4\frac{\omega_p^2}{c^2}k_i^2\left[1 + \frac{3}{4}\frac{\omega_p^2}{c^2k_i^2}\right] = 0 \end{aligned} \tag{A.12}$$

Divide by k_i^4 and define $\Delta = k/k_i$, $\alpha = (v_{th}/c)^2$, and $R = \frac{\omega_p^2}{c^2k_i^2}$.

$$\begin{aligned} \Delta^4 + 4\cos\theta\Delta^3 + 4\Delta^2\cos^2\theta\left(1 - \frac{R}{2\cos^2\theta} - \frac{3\alpha}{\cos^2\theta}\right) \\ -4\Delta\cos\theta R - 4R\left[1 + \frac{3}{4}R\right] = 0 \end{aligned} \tag{A.13}$$

For 90° scattering $k^2 = k_i^2 + k_s^2$ and $\cos\theta = -k_i/k = -1/\Delta$.

$$\Delta^4 - 4\left(1 + \frac{R}{2} + 3\alpha\right)\Delta^2 + 4\left[1 - \frac{3}{4}R^2\right] = 0 \tag{A.14}$$

Solving for Δ^2 we find,

$$\Delta^2 = (2 + R + 6\alpha) \pm 2\left[R + R^2 + 6\alpha\left(1 + \frac{R}{2} + \frac{3}{2}\alpha\right)\right]^{1/2}. \tag{A.15}$$

Now making the approximation $R \approx \frac{n}{n_c}$.

$$\Delta^2 \approx 2 + \frac{n}{n_c} + 6\left(\frac{v_{th}}{c}\right)^2 \pm 2\left[\frac{n}{n_c} + 6\left(\frac{v_{th}}{c}\right)^2 + \left(\frac{n}{n_c}\right)^2\right]^{1/2} \tag{A.16}$$

$$\Delta \approx 2^{1/2}\sqrt{1 + \frac{n}{n_c} \pm 2\left[\frac{n}{n_c} + 6\left(\frac{v_{th}}{c}\right)^2 + \left(\frac{n}{n_c}\right)^2\right]^{1/2}} \tag{A.17}$$

$$\frac{k}{k_i} \approx 2^{1/2}\left\{1 + \frac{1}{2}\frac{n}{n_c} \pm \frac{1}{2}\left[\frac{n}{n_c} + 6\left(\frac{v_{th}}{c}\right)^2 + \left(\frac{n}{n_c}\right)^2\right]^{1/2}\right\} \tag{A.18}$$

In terms of the separation between scattering features,

$$\frac{\Delta\lambda}{\lambda_i} = \left(\frac{k_i}{k_{s,+}} - \frac{k_i}{k_{s,-}}\right) \tag{A.19}$$

and

$$\frac{k_s}{k_i} = \sqrt{\Delta^2 - 1}. \tag{A.20}$$

Then,

$$\frac{k_s}{k_i} \approx 1 \pm \left[\frac{n}{n_c} + 6\left(\frac{v_{th}}{c}\right)^2 + \left(\frac{n}{n_c}\right)^2\right]^{1/2} \tag{A.21}$$

$$\frac{\Delta\lambda}{\lambda_0} \approx 2\left[\frac{n}{n_c} + 6\left(\frac{v_t}{c}\right)^2 + \left(\frac{n}{n_c}\right)^2\right]^{1/2}\left(1 + \frac{n}{n_c}\right) \tag{A.22}$$

and dropping terms of order $(n/n_c)^2$ we arrive at the desired result,

$$\frac{\Delta\lambda}{\lambda_0} \approx 2\left[\frac{n}{n_c} + 6\left(\frac{v_t}{c}\right)^2\right]^{1/2}\left(1 + \frac{3}{2}\frac{n}{n_c}\right). \tag{A.23}$$

Bibliography

[1] J. S. Ross, S. H. Glenzer, J. P. Palastro, B. B. Pollock, D. Price, L. Divol, G. R. Tynan, and D. H. Froula, "Observation of Relativistic Effects in Collective Thomson Scattering," *Physical Review Letters*, vol. 104, MAR 12 2010.

[2] J. P. Palastro, J. S. Ross, B. Pollock, L. Divol, D. H. Froula, and S. H. Glenzer, "Fully relativistic form factor for Thomson scattering," *Physical Review E*, vol. 81, MAR 2010.

[3] G. Gregori, S. H. Glenzer, J. Knight, C. Niemann, D. Price, D. H. Froula, M. J. Edwards, R. P. J. Town, W. Rozmus, A. Brantov, W. Rozmus, and V. Y. Bychenkov, "Effect of nonlocal transport on heat-wave propagation," *Physical Review Letters*, vol. 92, no. 20, 2004.

[4] D. H. Froula, P. F. Davis, B. B. Pollock, L. Divol, J. S. Ross, J. Edwards, R. P. J. Town, D. Price, S. H. Glenzer, A. A. Offenberger, G. R. Tynan, and A. N. James, "Quenching of the nonlocal electron heat transport by large external magnetic fields in a laser produced plasma measured with imaginng thomson scattering," *Physical Review Letters*, vol. 98, no. 13, p. 135001, 2007.

[5] N. L. Kugland, C. G. Constantin, P. Neumayer, H. K. Chung, A. Collette, E. L. Dewald, D. H. Froula, S. H. Glenzer, A. Kemp, A. L. Kritcher, J. S. Ross, and C. Niemann, "High k alpha x-ray conversion efficiency from extended source gas jet targets irradiated by ultra short laser pulses," *Appl Phys Lett*, vol. 92, no. 24, p. 241504, 2008.

[6] D. H. Froula, L. Divol, R. A. London, R. L. Berger, T. Doeppner, N. B. Meezan, J. S. Ross, L. J. Suter, C. Sorce, and S. H. Glenzer, "Observation of the density threshold behavior for the onset of stimulated raman scattering in high-temperature hohlraum plasmas," *Phys Rev Lett*, vol. 103, no. 4, p. 045006, 2009.

[7] M. B. Schneider, D. E. Hinkel, O. L. Landen, D. H. Froula, R. F. Heeter, A. B. Langdon, M. J. May, J. McDonald, J. S. Ross, M. S. Singh, L. J. Suter, K. Widmann, B. K. Young, H. A. Baldis, C. Constantin, R. Bahr, V. Y.

Glebov, W. Seka, and C. Stoeckl, "Plasma filling in reduced-scale hohlraums irradiated with multiple beam cones," *Physics of Plasmas*, vol. 13, NOV 2006.

[8] D. Froula, P. Davis, L. Divol, J. Ross, N. Meezan, D. Price, and S. Glenzer, "Measurement of the dispersion of thermal ion-acoustic fluctuations in high-temperature laser plasmas using multiple-wavelength thomson scattering," *Phys Rev Lett*, vol. 95, p. 195005, Jan 2005.

[9] J. D. Jackson, *Classical Electrodynamics*. Hamilton Printing Company, thrid ed., 1998.

[10] J. Sheffield, *Plasma Scattering of Electromagnetic Radiation*. New York: Academic, 1975.

[11] I. H. Hutchinson, *Principles of Plasma Diagnostics*. 1987.

[12] W. E. Gordon *Proc. IRE*, vol. 46, no. 1824, 1958.

[13] K. Bowles, "Observation of vertical-incidence scatter from the ionosphere at 41 mc-sec," *Physical Review Letters*, vol. 1, no. 454, 1958.

[14] F. Kahn, "Long-range interactions in ionized gases in thermal equilibrium," *Astrophysical Journal*, vol. 129, no. 1, pp. 205–216, 1959.

[15] J. A. Fejer, "Scattering of radio waves by an ionized gas in thermal equilibrium," *Canadian Journal of Physics*, vol. 38, p. 1114, 1960.

[16] J. Renau, "Scattering of electromagnetic waves from a nondegenerate ionized gas," *Journal of Geophysical Research*, vol. 65, no. 11, pp. 3631–3640, 1960.

[17] J. Dougherty and D. Farley, "A theory of incoherent scattering of radio waves by a plasma," *Proceedings Of The Royal Society Of London Series A-Mathematical And Physical Sciences*, vol. 259, no. 1296, pp. 79–99, 1960.

[18] E. Salpeter, "Electron density fluctuations in a plasma," *Physical Review*, vol. 120, no. 5, pp. 1528–1535, 1960.

[19] G. Fiocco and E. Thompson, "Thomson scattering of optical radiation from an electron beam," *Physical Review Letters*, vol. 10, no. 3, pp. 89–&, 1963.

[20] E. Funfer, B. Kronast, and H. Kunze, "Experimental results on light scattering by a theta-pinch plasma using a ruby laser," *Physics Letters*, vol. 5, no. 2, pp. 125–127, 1963.

[21] S. Schwarz, "Scattering of optical pulses form a nonequilibrium plasma," *Proceedings of the IEEE*, vol. 51, no. 10, pp. 1362–&, 1963.

[22] H. Kunze, E. Funfer, and H. Rohr, "Electron temperature measurements in a megajoule theta-pinch by light scattering," *Physics Letters*, vol. 19, no. 1, pp. 11–&, 1965.

[23] P. Chan and R. Nodwell, "Collective scattering of laser light by a plasma," *Physical Review Letters*, vol. 16, no. 4, pp. 122–&, 1966.

[24] S. Ramsden and W. Davies, "Observation of cooperative effects in scattering of a laser beam from a plasma," *Physical Review Letters*, vol. 16, no. 8, pp. 303–&, 1966.

[25] O. Anderson, "Measurement of electron correlation spectrum in a plasma," *Physical Review Letters*, vol. 16, no. 22, pp. 978–&, 1966.

[26] D. Evans, M. Forrest, and Katzenst.J, "Co-operative scattering of laser light by a thetatron plasma," *Nature*, vol. 211, no. 5044, pp. 23–&, 1966.

[27] N. Peacock, D. Robinson, M. Forrest, P. Wilcock, and V. Sannikov, "Measurement of electron temperature by thomson scattering in tokamak-t3," *Nature*, vol. 224, pp. 488–&, Jan 1969.

[28] D. Evans and P. Carolan, "Measurement of magnetic field in a laboratory plasma by thomson scattering of laser light," *Physical Review Letters*, vol. 25, no. 23, pp. 1605–&, 1970.

[29] D. Masters and B. Rye, "Heterodyne-detection of co2-laser radiation scattered from a plasma arc jet," *Physics Letters A*, vol. 58, no. 2, pp. 108–110, 1976.

[30] Gondhale.AM and B. Kronast, "Relativistic effect in light-scattering spectrum of a theta-pinch plasma," *Physical Review A*, vol. 8, no. 1, pp. 441–445, 1973.

[31] B. Kronast, H. Rohr, E. Glock, H. Zwicker, and E. Funfer, "Measurements of ion and electron temperature in theta-pinch plasma by forward scattering," *Physical Review Letters*, vol. 16, no. 24, pp. 1082–&, 1966.

[32] D. E. Evans, "The effect of impurities on the spectrum of laser light scattered by a plasma," *Plasma Physics*, vol. 12, p. 573, 1970.

[33] G. Ward, R. Pechacek, and Trivelpi.AW, "Scattering of a laser beam by high-temperature plasmas," *Physical Review A*, vol. 3, no. 5, pp. 1721–&, 1971.

[34] E. Campbell, J. Hunt, E. Bliss, D. Speck, and R. Drake, "Nova experimental facility," *Review Of Scientific Instruments*, vol. 57, pp. 2101–2106, AUG 1986.

[35] S. H. Glenzer, C. A. Back, L. J. Suter, M. A. Blain, O. L. Landen, J. D. Lindle, B. J. MacGowan, G. F. Stone, R. E. Turner, and B. H. Wilde, "Thomson scattering fom inertial-confinement-fusion hohlraum plasmas," *Physical Review Letters*, vol. 79, no. 7, p. 1277, 1997.

[36] D. H. Froula, J. S. Ross, L. M. Divol, N. Meezan, A. J. Mackinnon, R. Wallace, and S. H. Glenzer, "Thomson-scattering measurements of high electron temperature hohlraum plasmas for laser-plasma interaction studies," *Phys Plasmas*, vol. 13, p. 052704, Jan 2006.

[37] R. D. Petrasso, C. K. Li, F. H. Seguin, J. R. Rygg, J. A. Frenje, R. Betti, J. P. Knauer, D. D. Meyerhofer, P. A. Amendt, D. H. Froula, O. L. Landen, P. K. Patel, J. S. Ross, and R. P. J. Town, "Lorentz Mapping of Magnetic Fields in Hot Dense Plasmas," *Physical Review Letters*, vol. 103, AUG 21 2009.

[38] S. H. Glenzer, C. A. Back, K. G. Estabrook, B. J. MacGowan, D. S. Montgomery, R. K. Kirkwood, J. D. Moody, D. H. Munro, and G. F. Stone, "Electron temperature and density measurements in laser-produced large-scale-length gas-bag plasmas by x-ray spectroscopy," *Physical Reveiw E*, vol. 55, no. 1, p. 927, 1997.

[39] S. H. Glenzer, W. Rozmus, B. J. MacGowan, K. G. Estabrook, J. D. De Groot, G. B. Zimmerman, H. A. Baldis, J. A. Harte, R. W. Lee, E. A. Williams, and B. G. Wilson, "Thomson scattering from high-z laser-produced plasmas," *Physical Review Letters*, vol. 82, no. 1, pp. 97–100, 1999.

[40] W. L. Kruer, *The Physics of laser plasma interactions*. Addison-Wesley Publishing Company, Inc., 1988.

[41] E. F. Taylor and J. A. Wheeler, *Spacetime Physics*. San Francisco and London: W. H. Freeman and Company, 1966.

[42] A. Visco, R. P. Drake, D. H. Froula, S. H. Glenzer, and B. B. Pollock, "Temporal dispersion of a spectrometer," vol. 79, p. 10F545, AIP, 2008.

[43] J. Sheffield, "Plasma scattering of electromagnetic radiation," p. 305, Jan 1975.

[44] J. M. Soures, R. L. McCrory, T. R. Boehly, R. S. Craxton, S. D. Jacobs, J. H. Kelly, T. J. Kessler, J. P. Knauer, R. L. Kremens, S. A. Kumpan, S. A. Letzring, W. D. Seka, R. W. Short, M. D. Skeldon, S. Skupsky, and C. P. Verdon, "Omega wupgrade laser for direct-drive target experiments," *Laser Particle Beams*, vol. 11, pp. 317–321, 1993.

[45] A. J. MacKinnon, S. Shiromizu, G. Antonini, J. Auerbach, H. Haney, D. H. Froula, J. Moody, G. Gregori, C. Constantin, C. Sorce, L. Divol, R. Griffith, S. H. Glenzer, J. Satariano, P. K. Whitman, S. N. Locke, E. L. Miller, R. Huff, K. Thorp, W. Armstrong, R. Bahr, W. Seka, G. Pien, J. Mathers, S. Morse, S. Loucks, and S. Stagnitto, "Implementation of a high energy 4ω probe beam on the omega laser facility," *Review of Scientific Instruments*, vol. 75, no. 10, p. 3906, 2004.

[46] D. H. Froula, J. S. Ross, L. Divol, and S. H. Glenzer, "Thomson-scattering techniques to diagnose local electron and ion temperatures, density, and plasma wave amplitudes in laser produced plasmas (invited)," *Rev Sci Instrum*, vol. 77, p. 10E522, Jan 2006.

[47] D. Salzmann, *Atomic Processes in Hot Plasmas*. Oxford, U.K.: Oxford University Press, 1998.

[48] S. H. Glenzer, C. A. Back, K. G. Estabrook, R. Wallace, K. Baker, B. J. MacGowan, B. A. Hammel, R. E. Cid, and J. S. De Groot, "Observation of two ion-acoustic wavis in a two-species laser-produced plamsa with thomson scattering," *Physical Review Letters*, vol. 77, no. 8, p. 1496, 1996.

[49] D. H. Froula, L. M. Divol, and S. H. Glenzer, "Measurement of nonlinear growth of ion-acoustic waves in two-ion-species plasmas with thomson scattering," *Physical Review Letters*, vol. 88, no. 10, p. 105003, 2002.

[50] J. D. Huba, *NRL Plasma Formulary*. 2000.

[51] M. J. May, M. B. Scheider, H.-K. Chung, and D. E. Hinkel *Livermore National Laboratory Report*, no. UCRL-JRNL-214752, 2005.

[52] D. H. Froula, L. Divol, and S. H. Glenzer, "Measurements of nonlinear growth of ion-acoustic waves in two-ion-species plasmas with thomson scattering," *Physical Review Letters*, vol. 88, no. 10, pp. 105003–1, 2002.

[53] D. H. Froula, L. Divol, D. G. Braun, B. I. Cohen, G. Gregori, A. Mackinnon, E. A. Williams, S. H. Glenzer, H. A. Baldis, D. S. Montgomery, and R. P. Johnson, "Stimulated brillouin scattering in the saturated regime," *Physics of Plasmas*, vol. 10, p. 1846, 2003.

[54] J. D. Lindl, P. A. Amendt, R. L. Berger, S. G. Glendinning, S. H. Glenzer, S. W. Haan, R. L. Kauffman, O. L. Landen, and L. J. Suter, "The physics basis for ignition using indirect-drive targets on the national ignition facility," *Physics of Plasmas*, vol. 11, no. 2, p. 339, 2004.

[55] H. Baldis, C. Laboune, J. Moody, T. Talinaud, and V. Tikhonchuk, "Localization of stimulated brillouin scattering in random phase plate plasmas," *Physical Review Letters*, vol. 80, p. 1900, 1998.

[56] D. Hinkel, M. Schneider, B. Young, A. Langdon, E. Williams, M. Rosen, and L. Suter, "Creation of hot radiation environments in laser-driven targets," *Physical Review Letters*, vol. 96, pp. 195001/1–4, 19 May 2006.

[57] M. B. Schneider, D. E. Hinkel, B. K. Young, J. P. Holder, A. B. Langdon, H. A. Baldis, R. Bahr, D. E. Bower, H. C. Bruns, K. M. Campbell, J. R. Celeste, S. Compson, C. G. Constantin, E. L. Dewald, S. N. Dixit, M. J. Eckart,

D. C. Eder, M. J. Edwards, A. D. Ellis, J. A. Emig, D. H. Froula, V. Glebov, S. H. Glenzer, D. Hargrove, C. A. Haynam, R. F. Heeter, M. A. Henesian, G. Holtmeier, D. L. James, K. S. Jancaitis, D. H. Kalantar, J. H. Kamperschroer, R. L. Kauffman, J. Kimbrough, R. Kirkwood, A. E. Koniges, O. L. Landen, M. Landon, F. D. Lee, B. J. MacGowan, A. J. Mackinnon, K. R. Manes, C. Marshall, M. J. May, J. W. McDonald, J. Menapace, S. J. Moon, E. I. Moses, D. H. Munro, J. R. Murray, C. Niemann, D. Pellinen, K. Piston, G. D. Power, V. Rekow, S. Roberts, J. A. Ruppe, J. Schein, W. Seka, R. Shepherd, M. S. Singh, C. Sorce, P. T. Springer, C. H. Still, C. Stoeckl, L. J. Suter, G. L. Tietbohl, R. E. Turner, B. M. V. Wonterghem, R. J. Wallace, A. Warrick, P. Watts, F. Weber, P. J. Wegner, E. A. Williams, and P. E. Young, "X-ray flux and x-ray burnthrough experiments on reduced-scale targets at the nif and omega lasers," Jan 2006.

[58] E. D. Wispelaere, V. Malka, S. Huller, F. Amiranoff, S. Baton, R. Bonadio, M. Casanova, F. Dorchies, R. Haroutunian, and A. Modena, "Formation of plasma channels in the interaction of a nanosecond laser pulse at moderate intensities with helium gas jets," *Phys Rev E*, vol. 59, pp. 7110–7120, Jan 1999.

[59] O. Landen and R. Winfield, "Laser scattering from dense cesium plasmas," *Phys Rev Lett*, vol. 54, no. 15, pp. 1660–1663, 1985.

[60] P. Michel, L. Divol, E. A. Williams, S. Weber, C. A. Thomas, D. A. Callahan, S. W. Haan, J. D. Salmonson, S. Dixit, D. E. Hinkel, M. J. Edwards, B. J. MacGowan, J. D. Lindl, S. H. Glenzer, and L. J. Suter, "Tuning the implosion symmetry of icf targets via controlled crossed-beam energy transfer," *Phys Rev Lett*, vol. 102, p. 025004, Jan 2009.